MACQUARIE
University
SYDNEY·AUSTRALIA

Classification of embayed beach morphology and quantifying the influence of headlands on beach and surf zone morphodynamics

By

Thomas Edmund Twysden Fellowes

BSc, MSc

A thesis submitted to Macquarie University

for the degree of Doctor of Philosophy

Department of Earth and Environmental Sciences

15 March 2020

Statement of Originality

This work has not previously been submitted for a degree or diploma in any university. To the best of my knowledge and belief, the thesis contains no material previously published or written by another person except where due reference is made in the thesis itself.

Thomas Edmund Twysden Fellowes

15 March 2020

Acknowledgements

I would like to say that this thesis is the result of the combined efforts from a number of people to whom I am eternally grateful. First, I would like to thank my supervisor, Ana Vila Concejo, for her constant support, encouragement and for believing in me. Thank you for the incredible research opportunities, the fieldtrips and the life experiences. Thank you for providing me with a lifetime supply of "shiny things" that have both inspired and distracted me over the years. To my supervisor, Shari Gallop I thank you for always supporting, reassuring and inspiring me to be my best; I'd like to say thank you to you Shari for being an "eagle eye" and for taking me under your wing and providing me with the opportunity to continue with this PhD. Ana and Shari, thank you both for being strong role models in all aspects of my life and for being "bad ass women in science". I have seen myself grow as a scientist and as a person working with you both and from now on, I promise I will try to keep it "less spicy". It has been a pleasure and a privilege to be your student over the past years and I look forward to long friendships with you both.

I am thankful to my supervisors Paul Hesse and Katherine Dafforn for being so supportive, I am grateful to you both for stepping in and joining the supervisor party in the second half of my candidature. Paul and Katie, you took the final supervisor number to 4 and I wouldn't have it any other way. All four of you have made this one of the most enjoyable experiences of my life. I would also like to thank Karin Bryan for the opportunity of a research collaboration

and exchange in New Zealand; for introducing me to an exciting research project; for the video image techniques I learnt and for the mentoring and guidance I received. In addition, I would like to thank all my co-authors, Jak McCarroll, Andrew Short and Mitchell Harley for their contribution to my thesis, for their expertise and mentoring.

I am particularly thankful to the academics and the students of the Geocoastal Research Group for the positive and friendly environment and the thought-provoking discussions. In particular, thanks to Jody Webster, Belinda Dechnik, Stephanie Duce, Bree Morgan and Tristan Salles for your professional and personal guidance and for the many the laughs we have shared. To Kelsey Sanborn, thank you for being an amazing friend and for making sure we both finished our PhDs; I couldn't have done this without you. To Zsanett Szilagyi thank you for your friendship and support.

On a personal note, thank you to all my friends who have encouraged and amused me throughout my PhD by constantly asking me about how many grains of sand I've counted. To my family; Mum, Dad, Meiko, B, Guy, Amy, Linda and John, thank you for the support and interest in my research and for your constant faith in my ability. And last, but certainly not least, thank you to my wonderful partner Davey, thank you for being there whenever I needed you and for putting up with me. You are amazing and I am lucky to have you in my life. As a reward I will now force you to read this thesis from cover to cover.

Abstract

Embayed beaches are common on mountain and cliff dominated coastlines, represent a large proportion of beaches globally, and have a range of embayment and headland geometries. The headlands around embayed beaches can shadow (protect) areas in their lee through wave refraction processes, creating an alongshore gradient in wave energy and hence beach and sand bar morphology. The varied headland morphology and wave conditions that exist on embayed beaches means that their responses to both storm and fair-weather conditions can be highly variable and hard to predict. Thus, embayed beaches do not typically fit the standard assumptions of beach morphodynamic classifications that assume some alongshore uniformity. Due to this, this thesis aims to classify embayed beaches globally and understand how headlands influence embayed beach morphodynamics across multiple scales. This thesis presents a multi-scale analysis of embayed beaches, including a global analysis that included a total of 168 beaches from Australia, New Zealand, Brazil, United Kingdom, Spain and Portugal. This global analysis classifies the morphological settings of embayed beaches, combined with detailed site-specific studies over days to years that focuses on quantifying how embayment settings and headlands influence the beach morphodynamics. Chapter 2 proposes a new embayed beach classification that categorises embayed beaches by their embayment geometry with an embayment morphometric parameter (γ_e), which is an empirical relationship between embayment area and coastal indentation; and ranges from Class 1 (least embayed) to Class 4 (most embayed). Chapter 3 uses monthly surveys in southeast Australia (2015–2019) at

9 beaches to demonstrate that that the four classes responded differently to storms, whereas recovery (this study and literature; $n = 22$) was consistent at 0.22 $m^3/m/day$ across low-moderate embayed beaches (Class 1–Class 3), but for high embayed beaches (Class 4) was considerably lower at 0.08 $m^3/m/day$, suggesting Class 4 beaches are the most vulnerable to storm impacts. Furthermore, Chapter 3 proposes a new trigonometry-based method quantified the headland shadow edge (X_{se}) length alongshore, which highlighted alongshore responses and showed headland protected (shadowed) zones experienced 7 times less volume losses than exposed zones to 8 powerful storms. Chapter 4 demonstrates a new method developed to quantify sand bar migration rates and vorticity from daily video images (2012–2018) at Bondi Beach (Australia). Results in this chapter show 4 key examples of sand bar response patterns to storms including, opened sand bar-rip channel, meandering sand bar/trough, concentric sand bar, and sand bar curvature switching, and these provide insights into storm-scale shifts in sand bar morphology. Alongshore gradients showed that protected zones experience 25 % less sand bar dynamics than exposed zones. Overall, this thesis quantifies fundamental relations between the degree of embaymentisation, headland shadowing and controls, alongshore morphodynamics and shifts in beach and sand bar morphology under storm and fair-weather conditions, under the framework of a new morphodynamic classification for embayed beaches.

Contents

List of Figures

List of Tables

List of Publications

Chapters 2 to 4 this thesis are based on the following original research articles (published and in preparation):

[Chapter 2] **Fellowes, T.E.,** Vila-Concejo, A., Gallop, S.L., 2019. Morphometric classification of swell-dominated embayed beaches. Marine Geology, 411, 78-87. https://doi.org/10.1016/j.margeo.2019.02.004

[Chapter 3] **Fellowes, T.E.,** Vila-Concejo, A., Gallop, S.L., Harley, M.D., Short, A. D., *In Prep*. The influence of embayed beach exposure and headland shadowing on storm erosion and recovery.

[Chapter 4] **Fellowes, T.E.,** Bryan, K.R., Gallop, S.L., McCarroll, R.J., Vila-Concejo, A., *In Prep*. Quantifying sand bar migration and vorticity from video on an embayed beach.

List of Published Datasets

Chapter 2 refers to the below published dataset:

[Chapter 2] **Fellowes, T.E.,** Vila-Concejo, A., Gallop, S.L., 2018. Embayed Beach Morphometrics Dataset, 1 ed, Mendeley Data. http://dx.doi.org/10.17632/c5bxpgbdr2.1

Chapter 3 refers to the below supplementary information:

[Chapter 3] Supplementary data in Section 6.2

Chapter 4 refers to the below supplementary information:

[Chapter 4] Supplementary data in Section 6.3

Authorship Statements and Co-author Contributions

List of Co-authors

The co-authors involved in the research articles that make up the body of this thesis (Chapters 2–4) are listed in alphabetical order by acronym below:

Name	Acronyms	Affiliation
Andrew L. Short	**ADS**	Geocoastal Research Group, University of Sydney, Australia
Ana Vila-Concejo	**AVC**	Geocoastal Research Group, University of Sydney, Australia
Karin R. Bryan	**KRB**	School of Science and Environmental Research Institute, University of Waikato, New Zealand
Mitchell D. Harley	**MDH**	Water Research Laboratory, University of New South Wales, Australia
R. Jak McCarroll	**RJM**	Coastal Processes Research Group, Plymouth University, United Kingdom
Shari L. Gallop	**SLG**	School of Science and Environmental Research Institute, University of Waikato, New Zealand
Thomas E. Fellowes	**TEF**	Department of Earth and Environmental Sciences, Macquarie University, Australia; Geocoastal Research Group, University of Sydney, Australia

Authorship statements

Authorship statements and co-author contributions (division of labour) are listed below and summarised in the table on the following page:

[Chapter 2] I was responsible for the development of the methodology, the collection and interpretation of the data, creating the figures and writing the paper. AVC, SLG and I equally agreed on the concept, design, research questions and aided in the editing process of the paper.

[Chapter 3] I was responsible for the development of the methodology in conjunction with AVC. I collected and analysied the data and oversaw the creation of figures and wrote the paper. AVC, SLG and I equally agreed on the concept, design, research questions. While ADS, AVC, MDH, SLG aided with the editing process of the paper.

[Chapter 4] I was responsible for developing the methodology for this paper and for data analysis. AVC, SLG, KRB and I equally agreed on the concept, design, research questions. KGB, AVC and I interpreted the data, and I oversaw the creation of figures and wrote the paper. All co-authors aided in the editing process of the paper.

Division of Labour

Author and co-author contributions are listed below alphabetically for Chapter 2 to 4 for the main tasks:

	[Chapter 2]	[Chapter 3]	[Chapter 4]
Conception and design	AVC, TEF	AVC, TEF	KRB, TEF
Planning and implementation	AVC, SLG, TEF	AVC, TEF	KRB, TEF
Data collection	TEF	ADS, MDH, TEF	TEF, RJM
Analysis and interpretation	AVC, SLG, TEF	AVC, SLG, TEF	AVC, KRB, RJM, SLG, TEF
Writing the article	TEF	TEF	TEF
Editing the article	AVC, SLG, TEF	ADS, AVC, MDH, SLG, TEF,	AVC, KRB, RJM. SLG, TEF
Overall Responsibility	TEF	TEF	TEF

Notation and Abbreviations

Notation		Units
u	Alongshore current velocity	m/s
x	Alongshore position	m
M_{along}	Alongshore sand bar migration	m/day
α_{eb}	Beach aspect	$^{\circ}$
X_d	Beach length	m
dX	Beach width from back of beach to mean sea level (MSL)	m
Δ	Change in variable	-
Γ_{cw}	Clockwise sand bar vorticity	s^{-1}
Γ_{ccw}	Counter-clockwise sand bar vorticity	s^{-1}
v	Cross-shore current velocity	m/s
y	Cross-shore position	m
M_{cross}	Cross-shore sand bar migration	m/day
P_{sum}	Cumulative wave power	Kw/m
ρ	Density of water	kg/m^3
A_e	Embayment area	m^2
a	Embayment indentation from headlands to back of beach	m
S_l	Embayment length (headland lengths plus beach length)	m
γ_e	Embayment morphometric parameter	-

δ'	Embayment scaling factor	-
g	Gravitational constant	m/s
X_{hl}	Headland length	m
X_{off}	Headland offset	m
θ_{hl}	Headland orientation relative to beach aspect (α_{eb})	$^\circ$
α_w	Incidence angle (beach aspect wave direction $^\circ$)	$^\circ$
I	Indentation ratio	-
θ_w	Instantaneous wave direction	$^\circ$
H_{max}	Maximum wave height	m
θ_m	Mean wave direction	$^\circ$
T_z	Mean wave period	s
Γ_{norm}	Normalisation of Γ_{sum} divided by number of storm days	$\Gamma/storm$
M_{norm}	Normalisation of M_{sum} divided by number of storm days	$m/storm$
T_p	Peak wave period	s
R	Percentage subaerial beach volume recovery	%
λ	Rip channel spacing	m
X_{sh}	Shadow beach length to typical wave direction	m
X_{se}	Shadow edge	m
H_s	Significant wave height	m
σ	Standard deviation	-
V	Subaerial beach volume	m^3/m
M_{sum}	Summation of Malong and Mcross from a storm	$m/storm\ days$
Γ_{sum}	Summation of Γ_{ccw} and Γ_{cw} from a storm	$\Gamma/storm\ days$
α_p	Topographic profile aspect	$^\circ$
Γ	Vorticity	s^{-1}
E	Wave energy	N/m^2
C_g	Wave group velocity	m/s
P	Wave power (energy flux)	Kw/m
R_o	Width between two headlands	m

Abbreviations

ARI	Average recurrence interval
BAT	Batemans Bay (Australia) offshore Waverider buoy
COR	Cornwall, United Kingdom
CP	Coromandel Peninsula, New Zealand
DPIE	Department of Planning, Industry and Environment, NSW Government, Australia
ENSO	El Niño Southern Oscillation
GAL	Galicia, Spain
GNSS	Global Navigation Satellite Systems
LBT	Longshore bar and trough
LTT	Low tide terrace
MEI	Multivariate El Niño Southern Oscillation Index
MSL	Mean sea level
MSR	Mean spring tidal range
NOAA	National Oceanic and Atmospheric Administration
NSW	New South Wales, Australia
PDO	Pacific Decadal Oscillation
RBB	Rhythmic bar and beach
RGB	Red–green–blue image pixel colours
RTK	Real-time kinematic
SAM	Southern Annular Mode
SC	Santa Catarina, Brazil
SYD	Sydney (Australia) offshore Waverider Buoy
TBR	Transverse bar and rip
Timex	Time-average image
WP	West-facing Portugal

1

Introduction

Human populations are concentrated on the coast, and it is predicted that by 2050 the coastal population will double, increasing by ~1.5 billion people (Neumann et al., 2015). Beaches and the coast are firmly embedded in the human psyche as an aesthetic place that is intrinsically important to life, culture and livelihoods (Barbier et al., 2011; Costas et al., 2015). Beaches are among the most recognisable of coastal environments and provide important ecosystem services that span ecological, cultural, social, economic, political and coastal hazard protection (Barbier et al., 2011; Carter, 2013). However, coastal communities and infrastructure are being threatened by climate change, with sea-level rise, and potential changes in storminess including wave direction and energy considered as key (Barnard et al., 2019; Hemer et al., 2013).

1.1 Beach Morphodynamics

Beaches are defined as a wave-driven accumulation of sediments at the coast, existing between the modal wave base (wave induced sediment transport limit) and the upper swash limit (subaerial wave limit) (Short, 1999) (Figure 1.1). Sandy beaches are common landforms that globally occupy 34 % of wave-exposed coastlines (Hardisty, 1994). Beaches also interact with other coastal landforms including dunes, cliffs and hills, reefs, estuaries, embayments and headlands (Masselink et al., 2014; Williams, 2017). These interactions fit into a generalised morphodynamic feedback between processes (waves and other environmental controls such as tides), sediment transport (movement) and morphology (form), that spans multiple spatial-temporal scales (Wright and Thom, 1977). Beaches are further separated according to Short and Woodroffe (2009) into four main groups representing wave-dominated, tide-modified, tide-dominated and intertidal rock or coral flat beaches.

Beaches are highly dynamic in response to variations in wind, waves, currents, tides, sediment supply and anthropogenic change (Barnard et al., 2015; Costas et al., 2005; Masselink et al., 2014; Wright and Short, 1984), and these responses can be non-linear in nature and hard to predict over temporal scales relevant to management (10s to 100s years) (Cowell and Thom, 1997). A key focus in coastal science has been on characterising beach responses in terms of

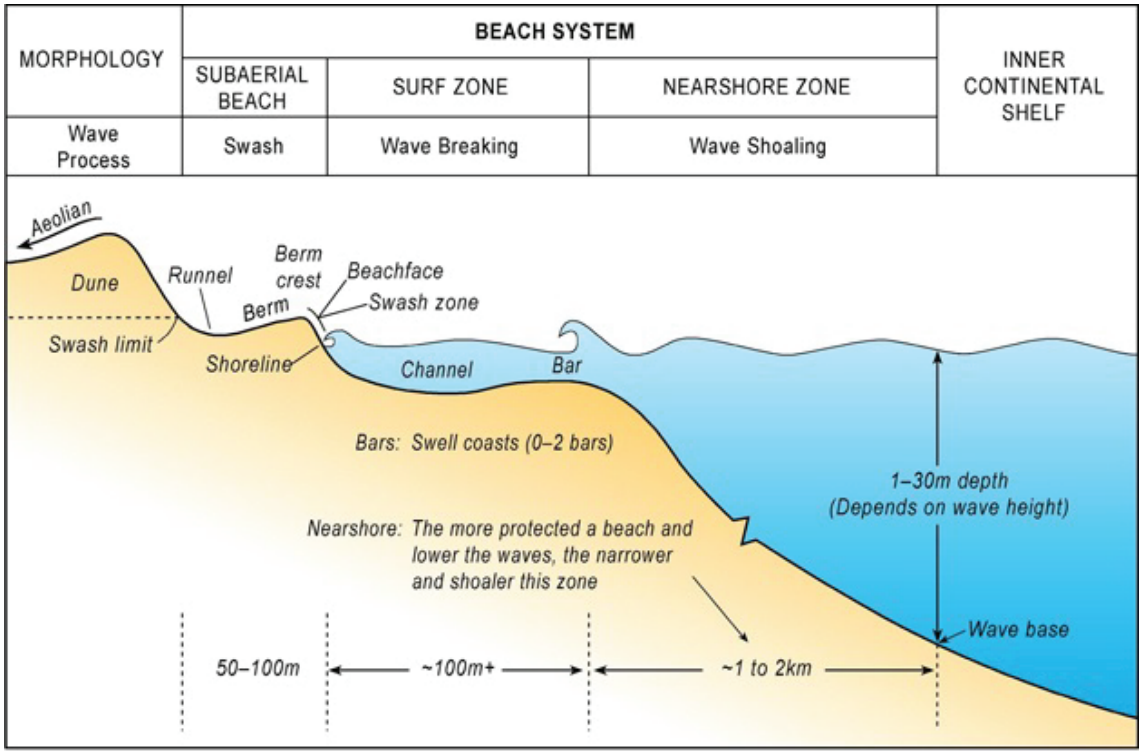

Figure 1.1: Cross-shore sections of a typically wave-dominated beach from Short and Woodroffe (2009).

erosion to energetic waves and storms, and subsequent recovery rates and pathways during fair-weather conditions (Battjes, 1974; Gourlay, 1968; Morton et al., 1994). Beach erosion typically manifests as changes in shoreline position (Boak and Turner, 2005; Vos et al., 2019), loss of subaerial beach volume (above mean sea level) and/or elevation, and changes cross-shore shape (Emery, 1961; Short and Trembanis, 2004). This generally occurs alongside the onshore and offshore migration of sand bars and can change cross-shore sand bar locations and morphology (Lippmann and Holman, 1990; Masselink and Short, 1993), which is intrinsically linked to subaerial beach changes (Wright and Short, 1984). Post-storm subaerial beach recovery may involve shoreline progradation (Yates et al., 2009), increase in beach volume (Harley et al., 2015), and changes in morphology such as accretion or erosion scarps. These are determined by exposure to fair-weather wave conditions (Costas et al., 2005; Loureiro et al., 2012a) alongside the availability of sediment, such as from sediment eroded during a previous storm from the subaerial beach to form a sand bar and sediment source for subaerial beach recovery. Recovery rates dictate beach vulnerability to subsequent storms, if recovery is slower than storm frequency,

then a beach would be more vulnerable that one whose recovery rate is faster the storm frequency (Scott et al., 2016). Meanwhile, geological controls such as headlands can further impact beach morphodynamics from physical processes that modify waves and morphodynamics (Bishop and Cowell, 1997; Hsu and Evans, 1989; Ranasinghe et al., 2004a).

1.1.1 Embayed Beaches

Beaches can be separated into fundamental categories based on the presence or absence of alongshore and cross-shore geological controls into: open beaches with no headlands, embayed beaches that are bound by physical structures (e.g., headlands), and protected or sheltered beaches (in harbours or estuaries) (Figure 1.2) (Short and Woodroffe, 2009). Coastlines that are hill and cliff dominated characterise over half of all coasts globally, with embayed beaches typically found on this type of coastline (Inman and Nordstrom, 1971; Short and Masselink, 1999). Embayed beaches are referred to by a multitude of terms including, headland-bay beaches (Klein et al., 2010), pocket beaches (Horta et al., 2018), zeta bays (Silvester et al., 1980), parabolic beaches (Hsu and Evans, 1989) and structurally controlled beaches (Short and Masselink, 1999). Embayed beaches are frequently found at the mouths of estuarine systems between rocky headlands that are the remnants of drowned river valleys (Bishop and Cowell, 1997), or are small-area coastal indentations where pockets of sediment accumulate as see on the southeast Portuguese coastline (Horta et al., 2018). Embayed beaches that have been studied in the literature and are found across the globe with examples from Perranporth and in southwest United Kingdom (Masselink et al., 2016; Scott et al., 2011), at Rodas in northwest Spain (Costas et al., 2005), at Amoreira in southern Portugal (Loureiro et al., 2012b), at Bombas and Bombinhas in southeast Brazil (Klein et al., 2010), at Palm Beach and Collaroy-Narrabeen in southeast Australia (Ranasinghe et al., 2004a; Short, 2007) and Tairua and Pauanui in northeast New Zealand (Bryan et al., 2013; Gallop et al., 2011).

Embayed beaches have a variety of embayment and headland geometries that contribute to the wide range of embayment shapes and sizes found in nature (Jackson et al., 2005). These physical attributes define the geomorphological setting of embayed beaches (Hsu and Evans, 1989;

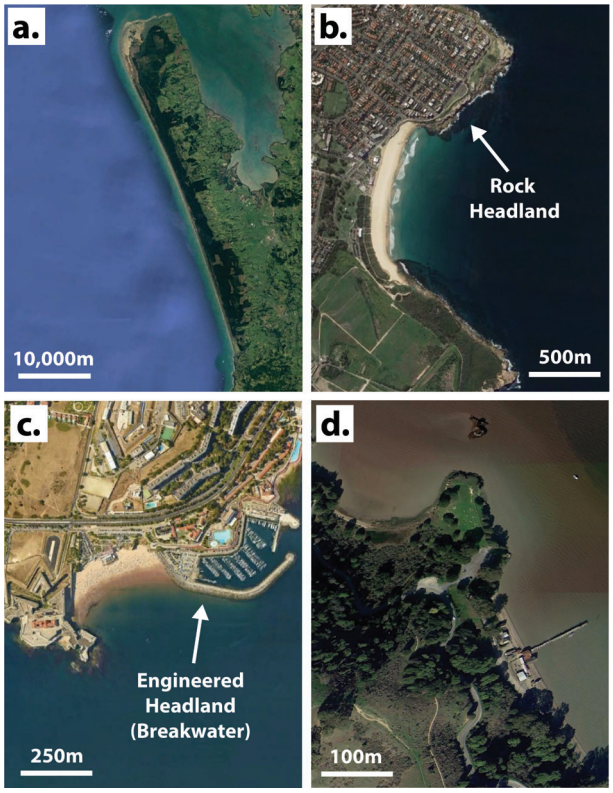

Figure 1.2: Examples of beach categories based on alongshore geological control, (a) open beach (Muriwai, New Zealand), (b) natural embayed beach (Maroubra, Australia), (c) structurally-engineered embayed beach (Torre, Portugal), and (d) protected estuarine beaches (Rat Rock Cove (top) and China Camp (bottom), San Francisco, USA). Image Source: Google Earth Inc.

Jackson and Cooper, 2009). Embayed beaches differ from open beaches (non-headland) due to geological controls on their morphodynamics (Short and Masselink, 1999). The headlands on embayed beaches modify waves through wave convergence onto the headlands and by refraction and diffraction around headlands (Hsu and Evans, 1989). These processes produce a range of embayed beach morphologies and morphodynamic responses that are different to open beaches (Loureiro et al., 2012b; Mortlock and Goodwin, 2016). In addition, headlands that extend further seaward than the surf zone have the potential to retain resuspended and redistributed sediment within the embayment during fair-weather and storm conditions (Pitman et al., 2016). This retention allows many embayed beaches to be considered as closed sedimentary systems with no or limited littoral sediment transport in or out of the system (Silvester, 1985). However, sediment bypassing around headlands can occur if embayments have a shallow coastal indentation or experience a high-wave obliquity from storm waves or when tidal currents dominate the system

(McCarroll et al., 2018; Valiente et al., 2019).

Embayed beaches commonly have non-uniform morphology alongshore and morphodynamics due to the presence of headlands (Castelle and Coco, 2012; Harley et al., 2015) (Figure 1.3). This is because headlands interact with oblique waves (relative to beach aspect) and create an alongshore wave energy and hence morphology gradient that can be highly variable over multiple time scales including storms and seasons (Castelle and Coco, 2012; McCarroll et al., 2016). A wave shadow zone can occur in the lee of headlands depending on the wave direction (typically oblique), creating a protected shadow zone (Daly et al., 2014). This can also occur with quasi shore-normal waves if beach curvature or headland orientations are exaggerated and shadow part of the beach (McCarroll et al., 2016) (Figure 1.3). Defining the morphodynamics between these protected and exposed (non-protected/shadowed) zones requires further investigation. For instance, nearshore currents and circulation in the shadowed protected zone are confined to the area adjacent at the headland rip and recirculates by headland shadow processes; while the reverse is seen at the exposed headland end of the beach that receives un-modified (un-shadowed) waves with wave deflection processes characterised by faster-flowing headland rips and greater recirculation than in the shadow zone (Castelle et al., 2016).

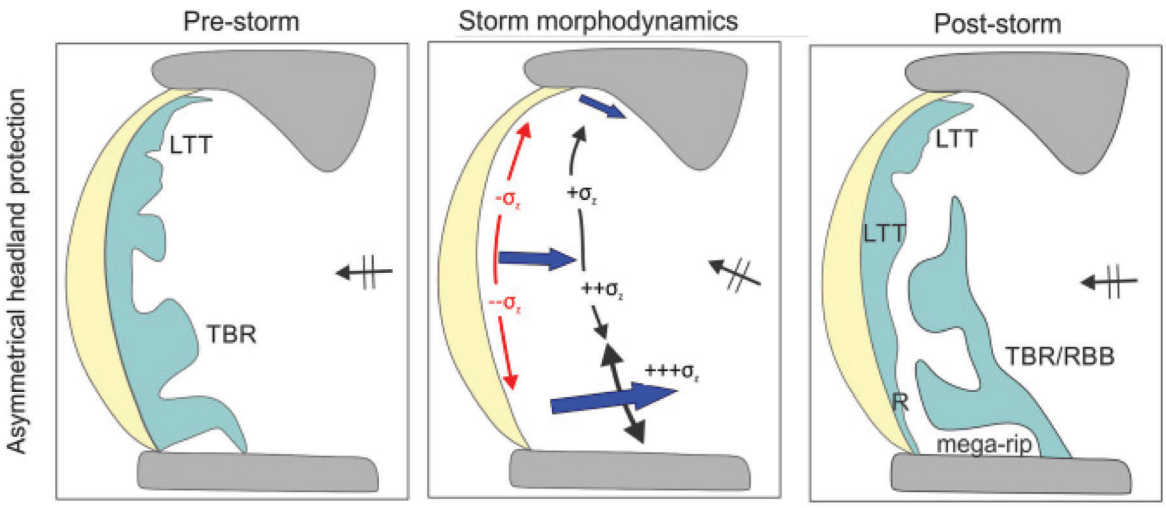

Figure 1.3: Example of alongshore beach morphology gradient at Bondi Beach, Australia which has asymmetrical headlands with the magnitude of sediment transport (blue arrow) and alongshore change (σ_z) shown by the gradient. Modified from McCarroll et al. (2016)

The headlands on embayed beaches also play a key role in dictating storm response through wave shadowing which further confounds erosion and recovery responses to storms (Loureiro et al., 2009). Scott et al. (2011) showed how on a regional scale adjacent beaches can have vastly different morphophonemic response to the same storm because of varying aspect and exposure to waves. In addition to headlands, other geological features such as offshore rocky reefs and islands can also influence the morphodynamic responses of the embayed adjacent beaches as shown at two adjacent beaches by Bryan et al. (2013). There is a clear need to develop an easy to apply classification for embayed beaches to account for impacts from headlands and the geomorphological setting, so that there can be greater understanding of embayed beach morphology and morphodynamics on a global scale.

1.2 Beach Classification

Beach classifications provide a practical way to group important beach processes, allowing comparative studies and quantification of beach dynamics. The first widely used framework that classifies and defines beach and sand bar morphology was proposed by Wright and Short (1984). It characterises wave-dominated sandy beaches into energy-states, based on waves, the dimensionless fall velocity of sediments (Ω), and observations of nearshore morphology. Their model describes up-shifts and down-shifts in beach and surf zone morphology to changing wave conditions. They proposed states ranging from a low energy reflective state, with four intermediate states including low tide terrace (LTT), transverse bar rip (TBR), rhythmic bar and beach (RBB) and longshore bar-trough (LBT), up to a high-energy dissipative state (Figure 1.4). A further extension to this model was proposed by Lippmann and Holman (1990), focusing on longshore variability within the intermediate beach states, although this model and that of Wright and Short (1984) are both open to subjective interpretation (Ranasinghe et al., 2004b), and Wright et al. (1987) identified that only 36 % of observed beaches correctly corresponded to the classification model. Masselink and Short (1993) built on these ideas to compare with relative tidal range and breaker wave height (H_b), to include the effects of tides, swash and wave run-up and surf zone dimensions and wave shoaling. However, there is uncertainty into what

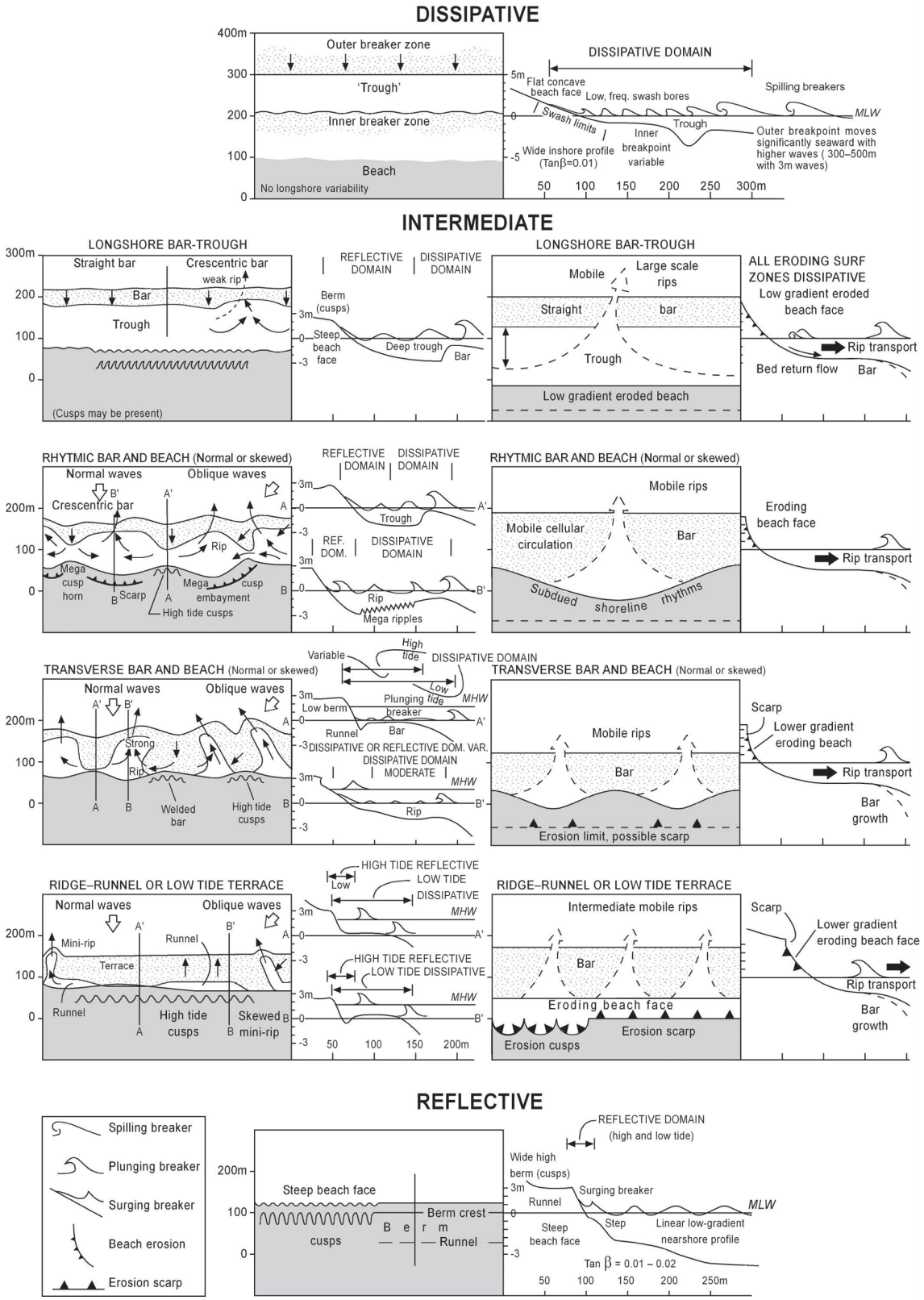

Figure 1.4: Morphological beach state model from Wright and Short (1984) for wave-dominated sandy beaches, ranging from reflective (low wave energy) to dissipative (high wave energy) from Short (2006).

conditions cause resets and this requires further investigation (Holman et al., 2006; Splinter et al., 2011a). The classification model was revisited by Costas et al. (2005) to use the relative tidal range maximum for applications on low-energy sheltered beaches. More recently, Scott et al. (2011) proposed a 9-state model integrating absolute wave power into established frameworks to better understand morphodynamics for integration into risk assessment programs. The existing classifications target beaches that do not have strong geological controls, and many beaches, such as embayed beaches, do not fit this assumption.

1.2.1 Embayed Beach Classification

To incorporate headlands and alongshore gradients in waves with beach response and morphology, Short and Masselink (1999) proposed a circulation model for embayed beaches. They attribute changes in circulation (rip channel morphology) to width between headlands (R_o) and embayment indentation length (S_l = beach and headland length). Their model presents three beach states of normal, transitional and cellular circulation show how there is a shift from open beach morphology (normal state) to headland-controlled morphology (cellular state) and incorporated surf zone width (X_s), rip number and spacing (λ_r) into their model (Figure 1.5). Jackson et al. (2005) and Jackson and Cooper (2009) described the geological impacts from underlying geology and lateral geological controls (headlands) in embayed beaches. They classified 3 beach types based on the influence of underlying geological substrates (Type I to III), that increase sediment mobility offshore and worsen beach responses to storms (Cooper et al., 2004). The Short and Masselink (1999) model was then examined by Castelle and Coco (2012) who showed that sand bars migrate alongshore towards the exposed headland under oblique waves and they suggest that spacing between rip channels is driven by self-organisation. McCarroll et al. (2016) highlighted how the models of Short and Masselink (1999) and Castelle and Coco (2012) did not allow for beaches that may have asymmetrical headland orientations (Figure 1.3), by assuming that both headlands are uniform in headland morphology (e.g., headland length, orientation and asymmetry) (Figure 1.5). These uniform headlands are not representative of the many headland morphologies found in nature (George et al., 2015). Embayed beach classifications have been expended in recent years to include

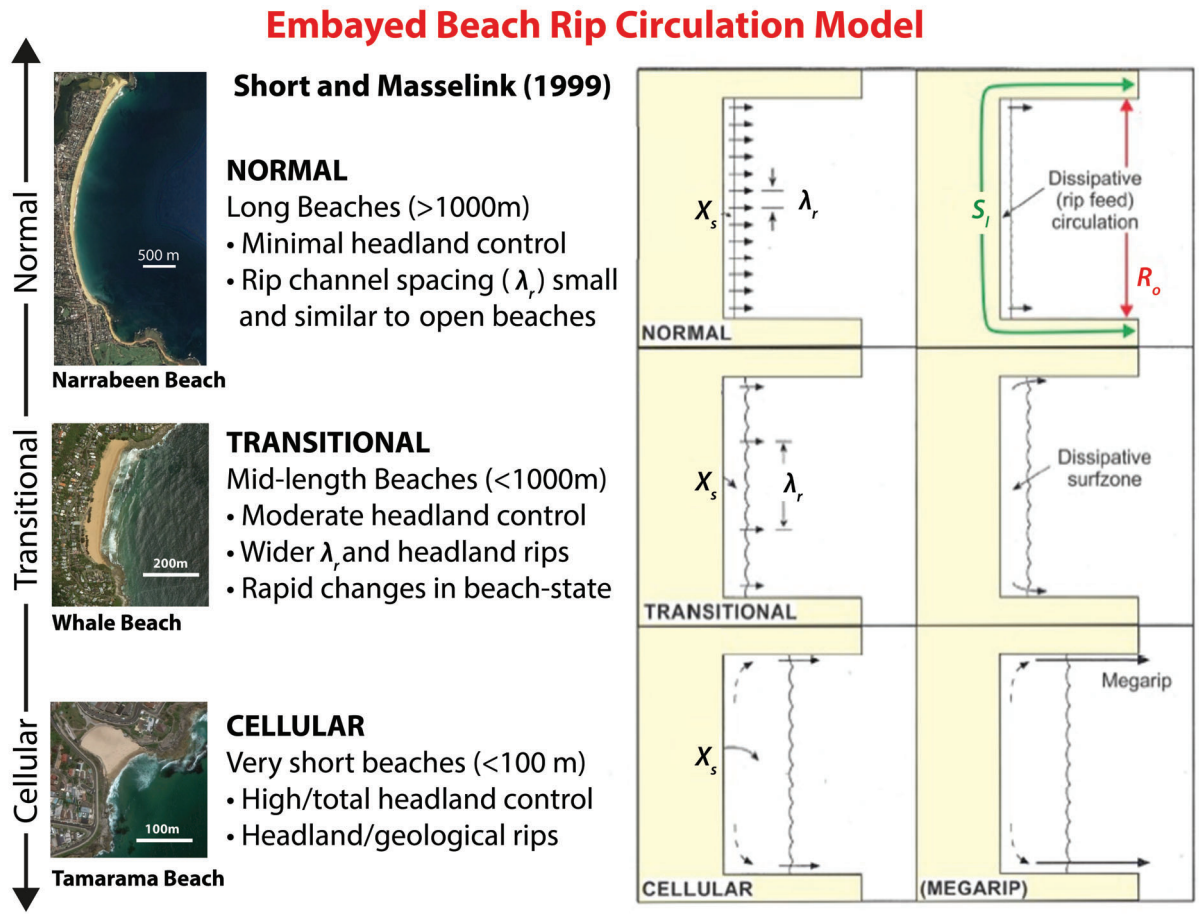

Figure 1.5: Embayed beach circulation model description and typical circulation with examples from Sydney, Australia for each category. Figure shows surf zone (X_s), rip channel spacings (λ_r), width between headlands (R_o) and embayment length (S_l). Modified from Short and Masselink (1999) and McCarroll (2014).

some of the natural variability in embayment and headland geometry, but there is still a room for improvement and a need to develop a classification that covers embayed beaches on a global scale.

1.2.2 Beach monitoring: current and state-of-the-art developments

Methods to monitor beaches have evolved vastly over the last 50 years. Traditional field surveys form the basis for modern approaches and methodologies (Emery, 1961; Harley et al., 2011). In recent years, field surveyors have used RTK-GNSS (Real-Time Kinematic–Global Navigation Satellite Systems) that allow for rapid and high precision surveying (Harley et al., 2011), allowing

for more beaches than ever to be included in studies. Meanwhile, video cameras (Holman and Stanley, 2007), airborne lidar (Phillips et al., 2019) and ground based lidar (Burvingt et al., 2017) are now commonly used to monitor beaches. More recent advancements and reduction in technology costs has seen the use open-access satellite imagery (e.g., Google Earth) (Vos et al., 2019), kites (Bryson et al., 2013) and drones (Joyce et al., 2019; Madrigal, 2019) to monitor beaches. These technological advances have transformed beach monitoring and multi-scaled approaches have become the new standard, integrating both field survey techniques with new remote sensing methods (Splinter et al., 2011b). For instance, images analysis techniques can be used to georeference images with applications to a range of coastal landforms including, beaches, flood tide deltas and sand bars (Lippmann and Holman, 1989; Smith and Bryan, 2007; van de Lageweg et al., 2013). These state-of-the-art advancements are allowing for more comprehensive beach studies as they are become cheaper, more automated and can include parts of the world that have never been visited. This thesis takes advantage of freely available satellite imagery and combines this with video image observations and more traditional RTK-GNSS survey techniques to create a multi-scaled approach to study embayed beaches.

1.3 Aim and objectives

This thesis uses state-of-art methods to answer the following questions using data from embayed beaches from all around the world. This thesis will address a key knowledge gap whereby previous embayed beach research has either been based on few sites or used open beach models without headland impacts to classify embayed beaches. The overreaching thesis aim is:

Classifying and understanding how headlands influence embayed beach morphology and storm response

The following research questions are formulated to address this aim, and each question is answered following a series of objectives:

Research question 1: *Is it possible to describe different types of embayed beaches by their geomorphological setting using morphometrics collected from open-access imagery?*

Objective 1.1 Develop a simple empirical relationship to classify the degree of embaymentisation (level of influence) from headlands have on embayed beach morphodynamics;

Objective 1.2 Develop a simple classification of embayed beach headland orientations that is universally applicable to embayed beaches;

Objective 1.3 Compare these two new classifications with previous classifications, apply them to globally representative regions and at a regional level to explore relationships in embayed beach morphometrics.

Research question 2: *Does the degree of embaymentisation and headland orientations impact embayed beach storm response and post-storm recovery rate?*

Objective 2.1 Compare how headlands and degree of embayment influence morphological response to storm conditions;

Objective 2.2 Determine how the degree of embaymentisation impacts post-storm recovery of the subaerial beach;

Objective 2.3 Assess how headlands impacts alongshore morphodynamics in protected (headland shadowed) and exposed zones of embayed beaches.

Research question 3: *Can we provide a new approach to quantify sand bar and rip channel responses along embayed beaches to storms from video?*

Objective 3.1 Develop a semi-automated method to measure patterns of sand bar migration and sand bar vorticity from video imagery;

Objective 3.2 Provide insights into sand bar morphodynamics on an embayed beach with asymmetrical headlands and an alongshore gradient in waves.

1.3.1 Approach and thesis structure

A multi-scaled approach was used to investigate embayed beaches across multiple spatial (metres to kilometres) and temporal (days to millennia) scales. This thesis is composed of chapters that are self-contained research articles in a format suitable for publication in a peer-review journal and are either published or in preparation for publication. These chapters (Chapters 2–4) have their own introductory sections, site descriptions and conclusions included, and as such, there is a small amount of repetition. The chapters that form the research component of this thesis address the above questions and objectives and answer the overarching thesis aim. A brief description of each chapter is given below.

[Chapter 1] (this chapter) introduces the importance of coastal geomorphology, embayed

beaches and briefly presents the current literature understanding and summarises key knowledge gaps and outlined the aim and research questions.

[Chapter 2] presents a new morphometric classification of embayed beaches based on the degree of embaymentisation from headlands. A quantitative assessment of embayment morphometrics from 168 beaches from six regions globally was undertaken using open-access satellite imagery. Chapter 2 proposes a new classification that statistically defines the degree of embaymentisation and describes 4 classes of embayed beach and we presents 6 headland orientation types. This chapter is published in *Marine Geology*.

[Chapter 3] explores a new method to quantify the alongshore morphodynamics in protected zones (shadowed in the lee of headlands) and exposed zones of embayed beaches in relation to headland shadowing processes. Chapter 3 focuses on 9 embayed beaches in southeast Australia across the range of 4 classes identified in Chapter 2. The analyses use monthly subaerial beach surveys between 2015 and 2019 and compare the storm response and recovery rates with embayed beaches from the literature.

[Chapter 4] presents a new pattern recognition methodology to quantify sand bar dynamics from video. This chapter expands on Chapter 3, furthering the research into alongshore morphodynamics in headland protected and exposed zones with focus on storm-scale sand bar morphodynamics. Chapter 4 presents a new method that quantifies sand bar migration and vorticity and demonstrates four examples of sand bar response patterns to storms, providing insights into shifts between morphologies on storm-scales at an embayed beach with asymmetrical headlands.

[Chapter 5] draws together the key findings of all the chapters, showing how this thesis has

advanced the state of knowledge of embayed beaches and geological control of beach morphodynamics. Chapter 5 also discusses key future research directions based on the findings of this thesis.

1.4 References

Barbier, E.B., Hacker, S.D., Kennedy, C., Koch, E.W., Stier, A.C., Silliman, B.R., 2011. The value of estuarine and coastal ecosystem services. Ecological Monographs 81, 169-193.

Barnard, P.L., Erikson, L.H., Foxgrover, A.C., Hart, J.A.F., Limber, P., O'Neill, A.C., van Ormondt, M., Vitousek, S., Wood, N., Hayden, M.K., Jones, J.M., 2019. Dynamic flood modeling essential to assess the coastal impacts of climate change. Scientific Reports 9, 4309.

Barnard, P.L., Short, A.D., Harley, M.D., Splinter, K.D., Vitousek, S., Turner, I.L., Allan, J., Banno, M., Bryan, K.R., Doria, A., Hansen, J.E., Kato, S., Kuriyama, Y., Randall-Goodwin, E., Ruggiero, P., Walker, I.J., Heathfield, D.K., 2015. Coastal vulnerability across the Pacific dominated by El Nino/Southern Oscillation. Nature Geosci 8, 801-807.

Battjes, J., 1974. Surf similarity. Coastal Engineering Proceedings 1.

Bishop, P., Cowell, P.J., 1997. Lithological and Drainage Network Determinants of the Character of Drowned, Embayed Coastlines. The Journal of Geology 105, 685-700.

Boak, E.H., Turner, I.L., 2005. Shoreline Definition and Detection: A Review. Journal of Coastal Research, 688-703.

Bryan, K.R., Foster, R., MacDonald, I., 2013. Beach Rotation at Two Adjacent Headland-Enclosed Beaches. Journal of Coastal Research, 2095-2100.

Bryson, M., Johnson-Roberson, M., Murphy, R.J., Bongiorno, D., 2013. Kite aerial photography for low-cost, ultra-high spatial resolution multi-spectral mapping of intertidal landscapes. PloS one 8, e73550.

Burvingt, O., Masselink, G., Russell, P., Scott, T., 2017. Classification of beach response to extreme storms. Geomorphology 295, 722-737.

Carter, R.W.G., 2013. Coastal Environments: An Introduction to the Physical, Ecological, and Cultural Systems of Coastlines. Elsevier Science.

Castelle, B., Coco, G., 2012. The morphodynamics of rip channels on embayed beaches. Continental Shelf Research 43, 10-23.

Castelle, B., Scott, T., Brander, R.W., McCarroll, R.J., 2016. Rip current types, circulation and hazard. Earth-Science Reviews 163, 1-21.

Costas, S., Alejo, I., Vila-Concejo, A., Nombela, M.A., 2005. Persistence of storm-induced morphology on a modal low-energy beach: A case study from NW-Iberian Peninsula. Marine Geology 224, 43-56.

Costas, S., Ferreira, O., Martinez, G., 2015. Why do we decide to live with risk at the coast? Ocean Coastal Management 118, 1-11.

Cowell, P.J., Thom, B.G., 1997. Morphodynamics of coastal evolution, in: Carter, R.W.G., Woodroffe, C.D. (Eds.), Coastal Evolution: Late Quaternary Shoreline Morphodynamics. Cambridge University Press, United Kingdom and New York, pp. 33-86.

Daly, C.J., Bryan, K.R., Winter, C., 2014. Wave energy distribution and morphological

development in and around the shadow zone of an embayed beach. Coastal Engineering 93, 40-54.

Emery, K., 1961. A simple method of measuring beach profiles. Limnology and Oceanography 6, 90-93.

Gallop, S.L., Bryan, K.R., Coco, G., Stephens, S.A., 2011. Storm-driven changes in rip channel patterns on an embayed beach. Geomorphology 127, 179-188.

George, D.A., Largier, J.L., Storlazzi, C.D., Barnard, P.L., 2015. Classification of rocky headlands in California with relevance to littoral cell boundary delineation. Marine Geology 369, 137-152.

Gourlay, M.R., 1968. Beach and dune erosion tests. Delft Hydraulics Laboratory, Rep. M935/M936.

Hardisty, J., 1994. Beach and nearshore sediment transport, in: Pye, K. (Ed.), Sediment transport and depositional processes. , Blackwell, London, UK, pp. 216-255.

Harley, M.D., Turner, I.L., Short, A.D., 2015. New insights into embayed beach rotation: The importance of wave exposure and cross-shore processes. Journal of Geophysical Research: Earth Surface 120, 1470-1484.

Harley, M.D., Turner, I.L., Short, A.D., Ranasinghe, R., 2011. Assessment and integration of conventional, RTK-GPS and image-derived beach survey methods for daily to decadal coastal monitoring. Coastal Engineering 58, 194-205.

Hemer, M.A., Fan, Y., Mori, N., Semedo, A., Wang, X.L., 2013. Projected changes in wave climate from a multi-model ensemble. Nature Climate Change 3, 471. Holman, R.A., Stanley, J., 2007. The history and technical capabilities of Argus. Coastal Engineering 54, 477-491.

Holman, R.A., Symonds, G., Thornton, E.B., Ranasinghe, R., 2006. Rip spacing and persistence on an embayed beach. Journal of Geophysical Research: Oceans 111, C01006.

Horta, J., Oliveira, S., Moura, D., Ferreira, Ó., 2018. Nearshore hydrodynamics at pocket beaches with contrasting wave exposure in southern Portugal. Estuarine, Coastal and Shelf Science 204, 40-55.

Hsu, J., Evans, C., 1989. Parabolic Bay Shapes and Applications. Proceedings of the Institution of Civil Engineers 87, 557-570.

Inman, D.L., Nordstrom, C.E., 1971. On the Tectonic and Morphologic Classification of Coasts. The Journal of Geology 79, 1-21.

Jackson, D.W.T., Cooper, J.A.G., 2009. Geological Control on Beach Form: Accommodation Space and Contemporary Dynamics. Journal of Coastal Research, 69-72.

Jackson, D.W.T., Cooper, J.A.G., del Rio, L., 2005. Geological control of beach morphodynamic state. Marine Geology 216, 297-314.

Joyce, K.E., Duce, S., Leahy, S.M., Leon, J., Maier, S.W., 2019. Principles and practice of acquiring drone-based image data in marine environments. Marine and freshwater research 70, 952-963.

Klein, A.H.d.F., Ferreira, Ó., Dias, J.M.A., Tessler, M.G., Silveira, L.F., Benedet, L., de Menezes, J.T., de Abreu, J.G.N., 2010. Morphodynamics of structurally controlled headland-bay beaches in southeastern Brazil: A review. Coastal Engineering 57, 98-111.

Lippmann, T., Holman, R., 1990. The spatial and temporal variability of sand bar morphology. Journal of Geophysical Research 95, 11,575 - 511,590.

Lippmann, T.C., Holman, R.A., 1989. Quantification of sand bar morphology: A video technique based on wave dissipation. Journal of Geophysical Research: Oceans 94,

995-1011.
Loureiro, C., Ferreira, O., Cooper, J.A.G., 2009. Contrasting Morphologic Behaviour at Embayed Beaches in Southern Portugal. Journal of Coastal Research, 83-87.
Loureiro, C., Ferreira, Ó., Cooper, J.A.G., 2012a. Extreme erosion on high-energy embayed beaches: Influence of megarips and storm grouping. Geomorphology 139–140, 155-171.
Loureiro, C., Ferreira, Ó., Cooper, J.A.G., 2012b. Geologically constrained morphological variability and boundary effects on embayed beaches. Marine Geology 329–331, 1-15.
Madrigal, L.T., 2019. Uas-based monitoring of sandy coasts in the Bay of Cadiz (SW Spain). Universidad de Cádiz.
Masselink, G., Hughes, M., Knight, J., 2014. Introduction to Coastal Processes and Geomorphology. Taylor Francis.
Masselink, G., Scott, T., Poate, T., Russell, P., Davidson, M., Conley, D., 2016. The extreme 2013/2014 winter storms: hydrodynamic forcing and coastal response along the southwest coast of England. Earth surface processes and Landforms 41, 378-391.
Masselink, G., Short, A.D., 1993. The Effect of Tide Range on Beach Morphodynamics and Morphology: A Conceptual Beach Model. Jounal of Coastal Research 9, 785-800.
McCarroll, R.J., 2014. Field observations of embayed beaches: lagrangiancirculation, morphodynamics and the rip current hazard. The University of New South Wales.
McCarroll, R.J., Brander, R.W., Turner, I.L., Van Leeuwen, B., 2016. Shoreface storm morphodynamics and mega-rip evolution at an embayed beach: Bondi Beach, NSW, Australia. Continental Shelf Research 116, 74-88.
McCarroll, R.J., Masselink, G., Valiente, N., Scott, T., King, E., Conley, D., 2018. Wave and Tidal Controls on Embayment Circulation and Headland Bypassing for an Exposed, Macrotidal Site. Journal of Marine Science and Engineering 6, 94.
Mortlock, T.R., Goodwin, I.D., 2016. Impacts of enhanced central Pacific ENSO on wave climate and headland-bay beach morphology. Continental Shelf Research 120, 14-25.
Morton, R.A., Jeffrey, G.P., James, C.G., 1994. Stages and Durations of Post-Storm Beach Recovery, Southeastern Texas Coast, U.S.A. Journal of Coastal Research 10, 884-908.
Neumann, B., Vafeidis, A.T., Zimmermann, J., Nicholls, R.J., 2015. Future Coastal Population Growth and Exposure to Sea-Level Rise and Coastal Flooding - A Global Assessment. PloS one 10, e0118571.
Phillips, M.S., Blenkinsopp, C.E., Splinter, K.D., Harley, M.D., Turner, I.L., 2019. Modes of Berm and Beachface Recovery Following Storm Reset: Observations Using a Continuously Scanning Lidar. Journal of Geophysical Research: Earth Surface 124, 720-736.
Pitman, S., Gallop, S.L., Haigh, I.D., Masselink, G., Ranasinghe, R., 2016. Wave breaking patterns control rip current flow regimes and surfzone retention. Marine Geology 382, 176-190.
Ranasinghe, R., McLoughlin, R., Short, A., Symonds, G., 2004a. The Southern Oscillation Index, wave climate, and beach rotation. Marine Geology 204, 273-287.
Ranasinghe, R., Symonds, G., Black, K., Holman, R., 2004b. Morphodynamics of intermediate beaches: a video imaging and numerical modelling study. Coastal Engineering 51, 629-655.
Scott, T., Masselink, G., O'Hare, T., Saulter, A., Poate, T., Russell, P., Davidson, M., Conley, D., 2016. The extreme 2013/2014 winter storms: Beach recovery along the southwest

coast of England. Marine Geology.
Scott, T., Masselink, G., Russell, P., 2011. Morphodynamic characteristics and classification of beaches in England and Wales. Marine Geology 286, 1-20.
Short, A.D., 1999. Handbook of Beach and Shoreface Morphodynamics. Wiley.
Short, A.D., 2006. Australian beach systems-nature and distribution. Journal of Coastal Research, 11-27.
Short, A.D., 2007. Beaches of the New South Wales coast: a guide to their nature, characteristics, surf and safety. Sydney University Press.
Short, A.D., Masselink, G., 1999. Embayed and structurally controlled embayed beaches, Handbook of beach and shoreface morphodynamics. Wiley, Chichester, pp. 230-250.
Short, A.D., Trembanis, A.C., 2004. Decadal Scale Patterns in Beach Oscillation and Rotation Narrabeen Beach, Australia—Time Series, PCA and Wavelet Analysis. Journal of Coastal Research, 523-532.
Short, A.D., Woodroffe, C.D., 2009. The Coast of Australia. Cambridge University Press, Melbourne, Australia.
Silvester, R., 1985. Natural headland control of beaches. Continental Shelf Research 4, 581-596.
Silvester, R., Tsuchtya, Y., Shibano, Y., 1980. Zeta bays, pocket beaches and headland control, Coastal Engineering 1980. American Society of Civil Engineers, Sydney, Australia, pp. 1306-1319.
Smith, R.K., Bryan, K.R., 2007. Monitoring Beach Face Volume with a Combination of Intermittent Profiling and Video Imagery. Journal of Coastal Research, 892-898.
Splinter, K.D., Holman, R.A., Plant, N.G., 2011a. A behavior-oriented dynamic model for sandbar migration and 2DH evolution. Journal of Geophysical Research: Oceans 116, (C1).
Splinter, K.D., Strauss, D.R., Tomlinson, R.B., 2011b. Assessment of Post-Storm Recovery of Beaches Using Video Imaging Techniques: A Case Study at Gold Coast, Australia. IEEE Transactions on Geoscience and Remote Sensing 49, 4704-4716.
Valiente, N.G., Masselink, G., Scott, T., Conley, D., McCarroll, R.J., 2019. Role of waves and tides on depth of closure and potential for headland bypassing. Marine Geology 407, 60-75.
van de Lageweg, W.I., Bryan, K.R., Coco, G., Ruessink, B.G., 2013. Observations of shoreline–sandbar coupling on an embayed beach. Marine Geology 344, 101-114.
Vos, K., Harley, M.D., Splinter, K.D., Simmons, J.A., Turner, I.L., 2019. Sub-annual to multi-decadal shoreline variability from publicly available satellite imagery. Coastal Engineering.
Williams, P.W., 2017. Chapter 8 - Coasts: the Mobile Interface Between Land and Sea, in: Williams, P.W. (Ed.), New Zealand Landscape. Elsevier, pp. 337-403.
Wright, L., Thom, B., 1977. Coastal depositional landforms: a morphodynamic approach. Progress in Physical Geography 1.
Wright, L.D., Short, A.D., 1984. Morphodynamic variability of surf zones and beaches: A synthesis. Marine Geology 56, 93-118.
Wright, L.D., Short, A.D., Boon, J.D., Hayden, B., Kimball, S., List, J.H., 1987. The morphodynamic effects of incident wave groupiness and tide range on an energetic beach. Marine Geology 74, 1-20.
Yates, M.L., Guza, R.T., O'Reilly, W.C., 2009. Equilibrium shoreline response: Observations and modeling. Journal of Geophysical Research: Oceans 114.

2

Morphometric classification of swell-dominated embayed beaches

This chapter is based on the following publication:

Fellowes, T.E., Vila-Concejo, A., Gallop, S.L., 2019. Morphometric classification of swell-dominated embayed beaches. Marine Geology, 411, 78-87.

https://doi.org/10.1016/j.margeo.2019.02.004

2.1 Abstract

Globally, embayed beaches are common to hilly and mountainous coastlines. They are typically characterised by two headlands that are a primary control on incident wave exposure and beach morphodynamics. Embayed beaches exist under a range of headland morphologies and degree of embaymentisation. Here, we present a generalised embayment morphometric parameter (γ_e) which classifies the geomorphological setting of embayed beaches based on the embayment indentation and area. We apply this to 168 swell-dominated embayed beaches from 6 regions using open-access imagery. The embayment morphometric parameter (γ_e) was subjected to k-means cluster analysis to identify 4 classes of embayed beaches with increasing γ_e indicating greater headland influence and impact on incident wave exposure. The Classes range from 1 to 4 with increasing degree of embayment. The most common is Class 2 (43 %, n = 73) which represents embayed beaches that have moderate embayment indentation and headland influence. There are clear trends in embayment geometry regardless of location, wave climate or tidal regimes. Within the embayments, there were 6 possible headland orientations (types H1–H6). The most common (58 %, n = 97) is when both headlands are orientated outwards from the beach (H6) and may result in greater morphological beach response from less headland shadowing, compared with headlands orientated inwards onto the beach (H1). In summary, we have developed a simple classification scheme for embayed beaches based on degree of indentation and headland orientation that can be applied to any embayed beach globally.

2.2 Introduction

Embayed beaches are bound laterally by physical barriers such as natural rocky headlands, submerged rocky platforms, and artificial harbour walls and breakwaters (Hsu and Evans, 1989). Embayed beaches are common to hilly and mountainous coasts, which constitute a large proportion of the world's coastlines (Short and Masselink, 1999). The term 'embayed beach' is an umbrella description for pocket (Bowman et al., 2009), headland-bay (Klein and Menezes, 2001), estuarine- and barrier-lagoon systems (Bishop and Cowell, 1997; Thom and Roy, 1985)

and tertiary compartments (Thom et al., 2018). There is a need to better assess the embayment geometry of embayed beaches for morphodynamic assessments and management purposes (Bowman et al., 2009). This assessment must include headland morphologies (orientation) and embayment morphometrics as they determine the physical extent of an embayment. The degree of embaymentisation is the primary geological regulator controlling the hydrodynamic and morphological processes on embayed beaches (Castelle and Coco, 2012; Jackson and Cooper, 2009; Loureiro et al., 2012b; Masselink et al., 2016). Currently, there is no simple assessment of headland orientations in relation to beach aspect for embayed beaches. Headlands on either end of an embayed beach are diverse and can be symmetrical or asymmetrical in terms of length, width, and orientation (McCarroll et al., 2016; Mortlock et al., 2017; Reniers et al., 2004). An embayment with a deep indentation has headland lengths that are substantially greater than width between the headlands (Bowman et al., 2009; Daly et al., 2014). This embayment geometrygenerally contains sediment with limited or no littoral sediment transport (Bryan et al., 2013). In contrast, an embayment with shallow indentation has headlands that are shorter than width between headlands (Bowman et al., 2009), and may experience littoral transport and headland bypassing under oblique and/or storm conditions (George et al., 2015; Horta et al., 2018; Silvester, 1985; Valiente et al., 2019). Headlands are responsible for inducing complex hydrodynamic interactions on embayed beaches through wave refraction (Loureiro et al., 2012a), dissipation and headland shadowing (Bryan et al., 2013; Castelle and Coco, 2012). For instance, an embayment with deep indentation has large headland impacts on incident waves, and therefore as per Short and Masselink (1999) the breaker wave height (H_b) at the beach is reduced by:

$$H_b = \sqrt{H_o^2(R_o/S_l)} \tag{2.1}$$

where, H_o is the offshore significant wave height, R_o is the width between headlands, and S_l is the total embayment length including beach and headlands. Shifts in wave direction relative to headland orientations can modify surf zone morphology (McCarroll et al., 2016), such as determining the number, position, spacing, and orientation of channel rip currents (Castelle and Coco, 2012; Holman et al,. 2006; Short, 1985); as well as, of headland and cellular rip currents

(Castelle et al., 2016; Loureiro et al., 2012b). Moreover, oblique waves can cause beach rotation by moving sand to the downdrift headland, rotating the shoreline position alongshore (Harley et al., 2014). Loureiro et al. (2013) states that due to these processes embayed beaches do not align with the commonly used morphodynamic beach state models. Much of embayed beach literature is heavily focused on relatively short-term (days to years) morphological responses to waves (Loureiro et al., 2012b); rather than the longer-term effects of the geomorphic embayment setting on beach morphology. Authors have approached the parameterisation of embayment morphometrics differently. Early work into describing static equilibrium planforms of embayed beaches by Hsu et al. (1989) was completed using imagery and maps to measure morphometrics that form embayed beach planforms. They then presented the planform ratio (I):

$$I = a/R_o \tag{2.2}$$

where, a is indentation of the embayment from headland point to the back-beach limit and R_o is width between headlands. This method considers all embayment to be parabolic in shape and does not include other embayment shapes (Klein and Menezes, 2001). Continuing from this, a widely used embayed beach classification is the non-dimensional embayment scaling factor (δ') of Short and Masselink (1999):

$$\delta' = S_l^2/100R_oH_b \tag{2.3}$$

where, S_l is the embayment length that combines length of both headland and beach length (X_d). This classification provides a simple methodology to describe three surf zone circulation patterns on embayed beaches; cellular ($\delta' < 8$), transitional ($\delta' = 8$–19) and normal beach circulation ($\delta' > 19$) (Castelle and Coco, 2012). However, when headland lengths are greater than surf zone width, a common occurrence in many embayed systems, this parameter overestimates the embayment processes (Castelle and Coco, 2013). Castelle and Coco (2012) extended Short and Masselink (1999)'s work through the non-dimensional scaling parameter (δ) which incorporates aspects of equation 2.3 and includes beach slope (tan_β), surf zone width (X_s) and significant wave height (H_s). However, both these approaches require morphometrics or in situ wave measurements found only at a limited number of embayed beaches. For instance, $tan\beta$ is a

highly variable parameter that should be measured in situ and H_b could be obtained through open-access wave propagation models (e.g., Wave Watch III) but is generally not accurate for individual embayments. Ultimately, a parameterisation that can include the natural variability evident in the many embayment shapes, areas and complex headland orientations is paramount for classifying embayed beaches.

In this paper, we present a generalised embayment morphometric parameter to classify the overall geomorphological setting of embayed beaches combining headland orientation and then compare with established embayment morphometrics and beach morphology. We first assessed embayment morphometrics of 168 swell-dominated embayed beaches using open-access imagery in 6 regions of the world. This was achieved by measuring 7 morphometric parameters to characterise embayments, including headland orientations relative to the beach aspect and shadowing to dominant (modal) regional wave direction. Second, we used these results to define a new generalised embayment morphometric parameter that reflects the degree of embaymentisation. This novel approach provides a simple empirical relationship to examine the influences that the inherent embayment geometry has on embayed beach morphodynamics. It is low-cost as it only needs parameters that can be obtained from open-access imagery combined with regional wave conditions.

2.3 Methods

2.3.1 Study Sites

We focused on 168 embayed beaches with two natural rocky headlands, mostly composed of sandy sediments, exposed to swell conditions, and not part of alongshore drift aligned sediment embayments (Figure 2.1). These regions were selected because they have established literature on their embayed beaches and wave climates (Table 2.1) and because they represent a range of embayments across a diverse range of tide, swell and storm conditions. The regions included Cornwall, United Kingdom (COR), Galicia, Spain (GAL), Leiria to Algarve, western Portugal (WP), New South Wales, Australia (NSW), Coromandel Peninsula, New Zealand (CP) and Santa

Catarina, Brazil (SC) (Figure 2.1).

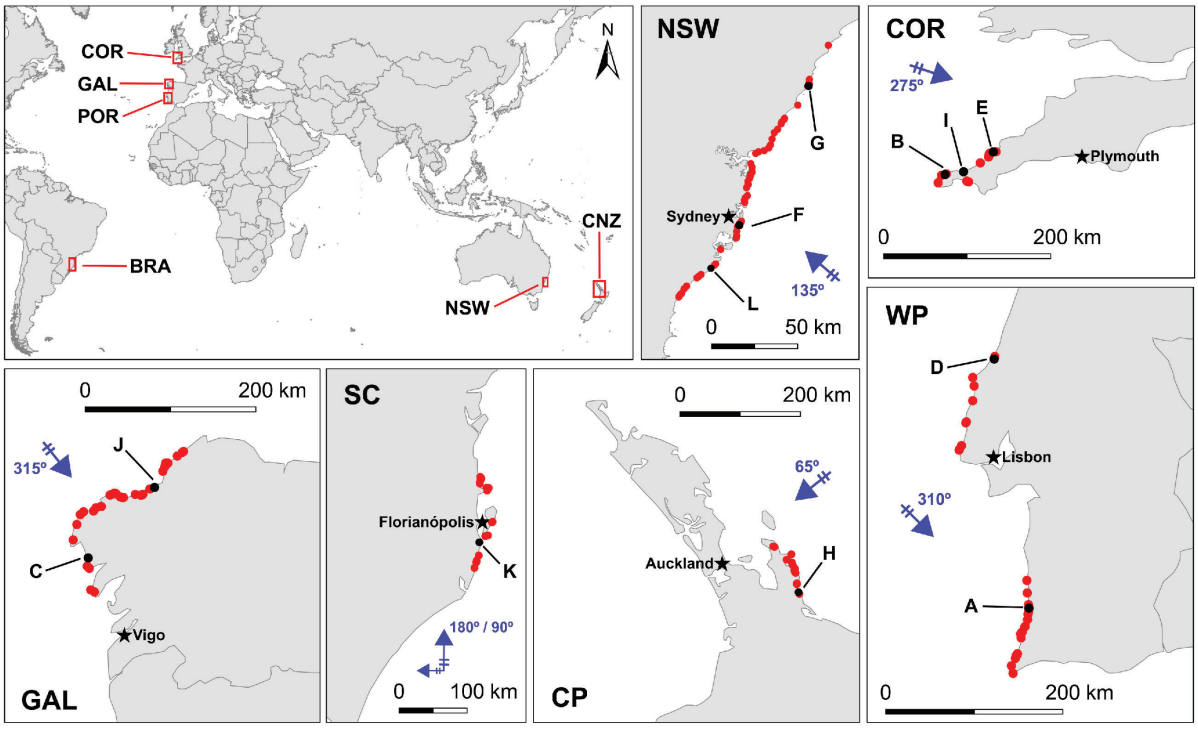

Figure 2.1: Embayed beach sites (n = 168) from the 6 regions showing all sites (red circles), select sites discussed in detail in the manuscript (black circles) and, dominant swell direction (°) (blue arrows). Regions are Cornwall, United Kingdom (COR), Galicia, Spain (GAL), Leiria to Algarve, western Portugal (WP), New South Wales, Australia (NSW), Coromandel Peninsula, New Zealand (CP) and Santa Catarina, Brazil (SC).

2.3.2 Morphometric Parameters

We measured 7 embayment morphometric geometries using the *measure*, *polygon* and *compass* tools from open-access imagery in Google Earth Pro (Google, Inc) (Figure 2.2). Naming conventions followed previous literature and are presented in Figure 2.2 (Hsu and Evans, 1989; Short and Masselink, 1999). These include, width between headlands (R_o) as the distance between the headland oceanward points. Headland orientations (θ_h) is between the point adjacent to headlands at the back-beach and the oceanward point. Embayment indentation (a) is the midpoint of the headland width line to the back-beach boundary (e.g., seawall). Embayment area (A_e) was calculated using the same headland width line and included the total area of the embayment drawing lines along the headlands and along the back-beach including the beach area. Alongshore beach length (X_d) was between the headland

Table 2.1: Regional characteristics of mean annual wave climate including significant wave height (H_s), peak period (T_p), swell wave direction (θ_m) from Wave Watch III timeseries (NOAA), mean spring tidal range (MSR), regional geology and relevant literature.

Region	**n**	H_s **(m)**	T_p **(m)**	θ_m **(º)**	**MSR (m)**	**Regional Geology**	**Relevant Beach and Hydrodynamic Literature**
COR	14	1–1.5	10	275	4.5	Granites and Metasediments	Masselink et al. (2014); Masselink et al. (2016); Scott et al. (2016); Valiente et al. (2019)
GAL	35	2–2.5	11	310	3.5	Granites and Metasediments	Costas et al. (2005); Iglesias and Carballo (2009); Iglesias et al. (2009a); Méndez and Vilas,(2005)
WP	32	1.5–2.5	11	310	3.5	Limestone and Dolomit	Horta et al. (2018); Loureiro et al. (2009); Loureiro et al. (2012a); Marques,(2009); Palha et al. (2010)
NSW	55	1–2	8–10	135	2	Quartz Sandstone	Harley et al. (2015); Mortlock et al. (2017); Short,and Trenaman (1992); Thom and Roy (1985)
CP	14	1.5	8	65	1.5	Dacitic-rhyolitic	Adams et al. (1994); Gallop et al. (2009); Gallop,et al. (2011); Gorman et al. (2003); Wright,(1992)
SC	24	1.5	8	125	0.5–1	Granites and Metasediments	Araújo,et al. (2003); Horn Filho,and Diehl, (2004); Klein,et al. (2010); Pianca et al. (2010)

boundaries. Embayment length (S_l) is a sum of X_d and each headland length. Shadowed beach length (X_{sh}) is the alongshore distance in the lee of each headland from typical swell direction and was also converted to percentage of X_d. An extensive analysis of the measured morphometrics found 2 to be the most influential on embayed beach geometries and beach morphodynamics. These are, the embayment area (A_e) which is responsible for regulating sediment budgets and the exposure to swell waves and the embayment indentation (a) which has a key influence on wave shadowing, dissipation and beach response. Therefore, to determine the impact of embaymentisation across a spectrum of embayment geometries, a combination of these two morphometrics where used to create the simple and informative embayment morphometric parameter (γ_e),

$$\gamma_e = a/\sqrt{A_e} \tag{2.4}$$

2.3.3 Embayed Beach Classification

Cluster analysis has previously been used to classify beach morphology (Scott et al., 2011), headland orientation and morphology (George et al., 2015) and coral reef spur and groove morphology (Duce et al., 2016). K-means cluster analysis was also chosen here for its computational efficiency and ability to output visual clusters of datasets with multiple iterations (here, n = 100). Clusters were computed using the embayment morphometric parameter (γ_e) with an initial user defined number of clusters that was trialled to determine the optimal number, using methods from Jain (2010). Whereby, they state clusters are best characterised by a low inter-cluster variability distance from centre of cluster (here, < 0.5 γ_e) and to also ensure to maximise the difference between each cluster. The four resulting clusters represent the classes of embayed beach that were then compared to δ' from Short and Masselink (1999) and previous assessments published in the literature (Bowman et al., 2009; Castelle and Coco, 2012; Elshinnawy et al., 2018a; Horta et al., 2018; Jackson and Cooper, 2009).

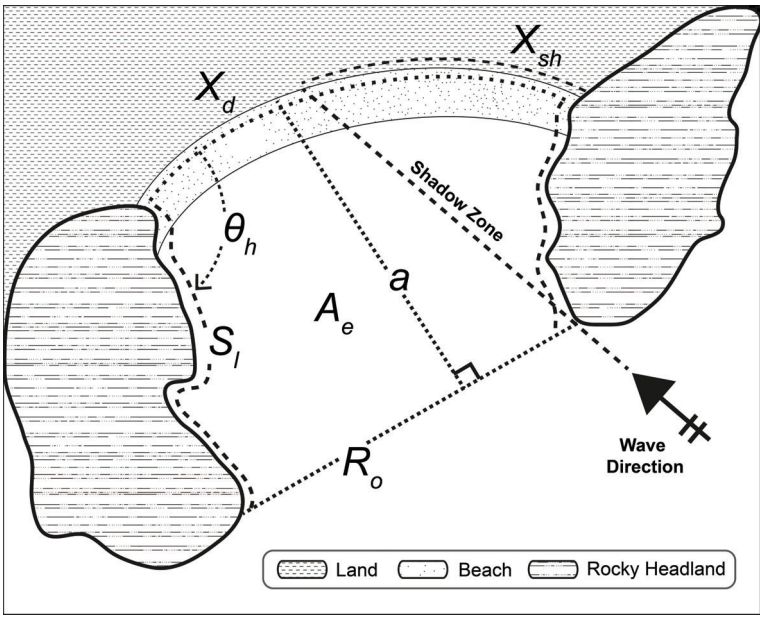

Figure 2.2: Morphometric parameters: embayment area (A_e), embayment indentation (a), headland orientation to beach aspect (θ_h), alongshore beach length (X_d), width between headlands (R_o), shadow zone and shadowed beach length (X_{sh}) and total embayment length including beach and headlands (S_l).

2.4 Results

2.4.1 Embayment Characteristics

2.4.1.1 Morphometric Analysis

There was great variability in morphometric parameters between and within the regions. Mean A_e for the 168 beaches was 960 $x10^3$ m^2,ranging from 9 $x10^3$ m^2 (Bogon beach, NSW, Figure 2.3g) to 13,580 $x10^3$ m^2 (Hayle beach, COR, Figure 2.3i). The regional mean A_e was largest in COR and lowest in WP (Figure 2.4a). Mean a was 580 m, ranging from 88 m (Pedra da Bica beach, WP, Figure 2.3a) to 2,740 m (Carnota beach, GAL, Figure 2.3c). The largest regional mean for a was COR, followed closely by GAL; NSW and WP had the lowest a (Figure 2.4b). Moreover, all beaches with $X_d \geq 100$ m also had $a > X_d$ and represented 34% of all sites (e.g., Crantock beach, COR, Figure 2.3e). The largest differences were at Riazor beach (GAL, Figure 2.3j) where X_d = 1,380 m while a was 1,580 m. Mean R_o was 1,300 m and ranged between 75 m (Bogon beach NSW, Figure 2.3g) and 6,430 m (Hayle beach, COR, Figure 2.3i). Regional R_o means were similar across GAL, NSW, CP and SC (Figure 2.4c). COR had the widest mean distance between headlands (R_o), while the most narrowly-spaced headlands were in WP. Twelve percent of beaches exhibited $R_o < a$ planform ratios (I, Eq. 2.2); of those, all of them were relatively short beaches with X_d < 1,000 m with the exception of Riazor beach (X_d = 1,380 m) in GAL (Figure 2.3j) and São Martinho do Porto beach (X_d = 2,120 m) in WP (Figure 2.3d). The lowest planform ratio, I (Eq. 2.2) was 0.16 at Mataora beach in CP (Figure 2.3h) represented the coastal relief of any beach in this study. Mean X_d was 1,100 m and ranged between 40 m (Bosigran Castle Cove beach, COR, Figure 2.3b) and 7,800 m (Hayle beach, COR, Figure 2.3i). Regional means were similar in COR, CP, and SC; the greatest regional X_d was in COR, while the lowest was in WP (Figure 2.4d).

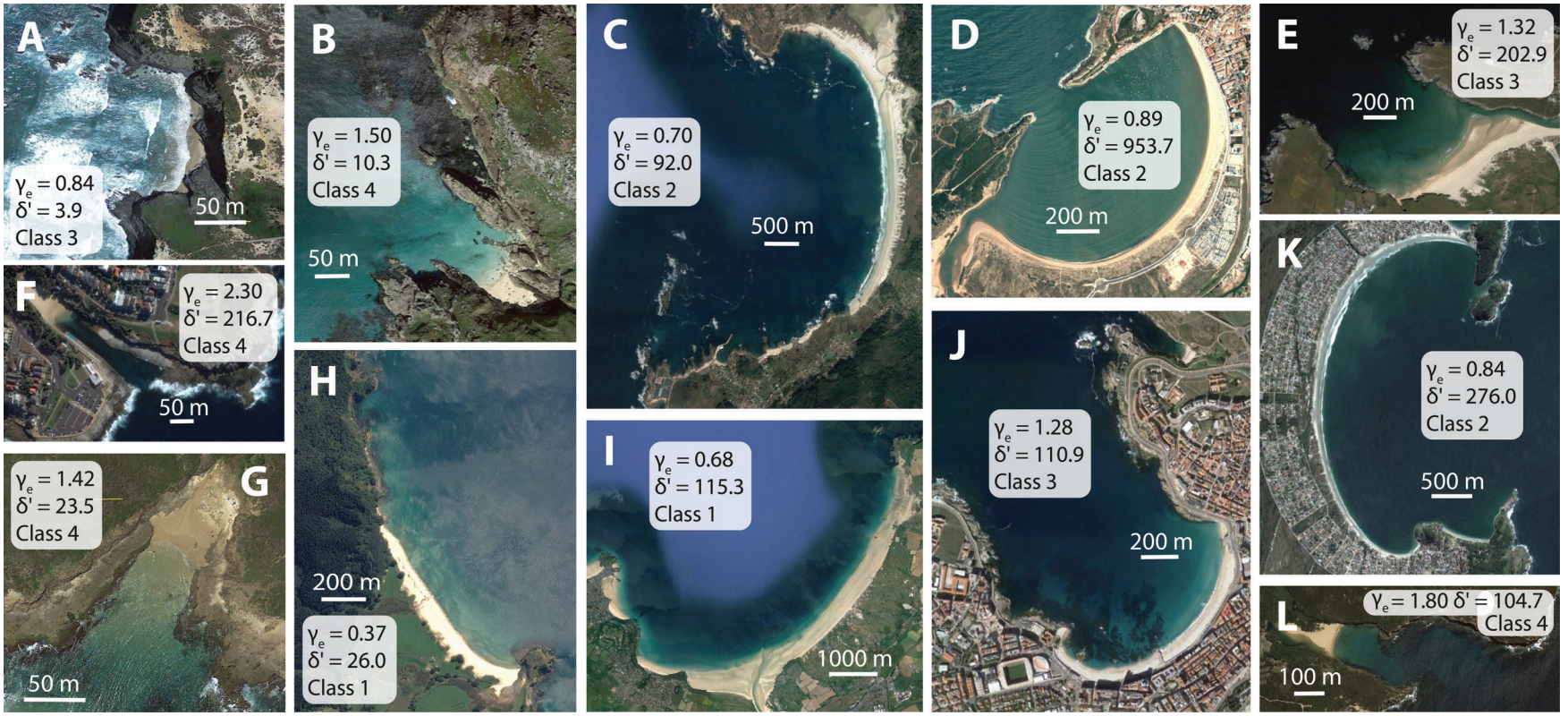

Figure 2.3: Embayed beaches discussed in text with γ_e (Eq. 4), δ' (Eq. 3) and the classes of embayed beach defined in this study. (a) Pedra da Bica, WP, (b) Bosigran Castle Cove, COR, (c) Carnota, GAL, (d) São Martinho do Porto, WP, (e) Crantock, COR, (f) Clovelly, NSW, (g) Bogon, NSW, (h) Mataora, CP, (i) Hayle, COR, (j) Riazor, GAL, (k) Meio, SC, and (l) Wattamolla, NSW. Images modified from Google Earth and available in Fellowes et al., (2018).

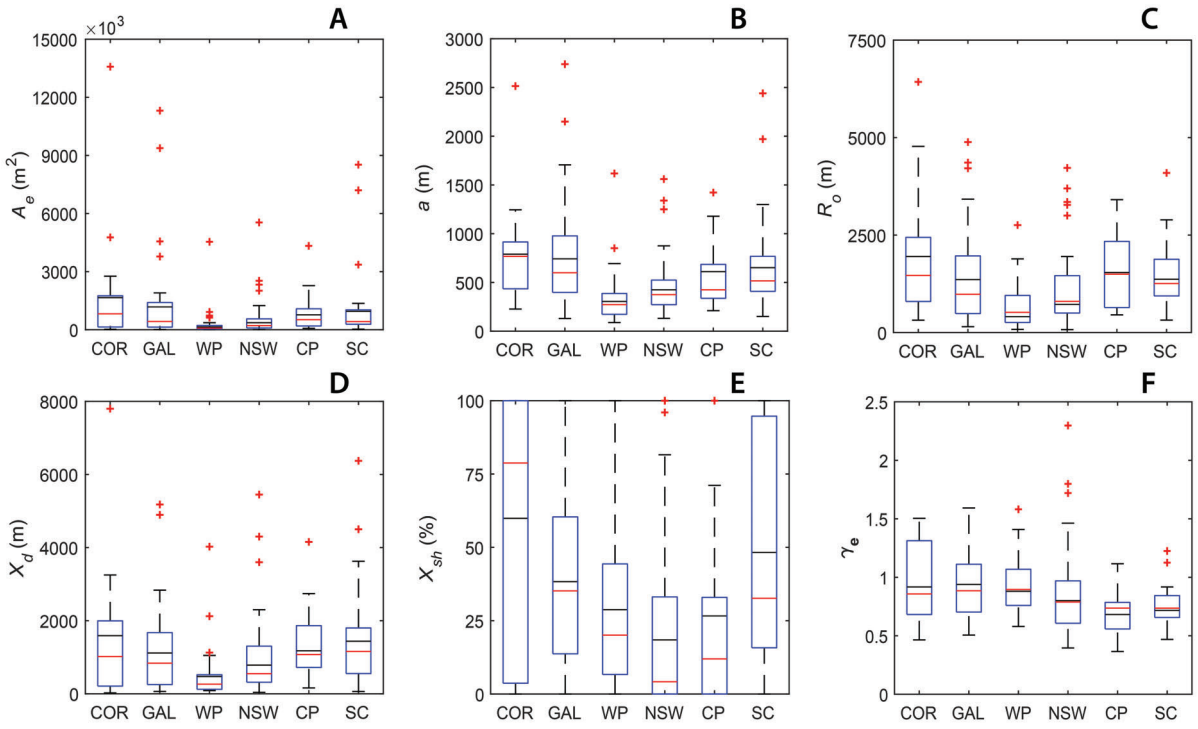

Figure 2.4: Morphometric analysis showing mean (black line), median (red line), 25th and 75th percentiles (blue box), range (black whiskers) and extreme data (red +).

2.4.1.2 Headland Analysis

We measured the orientation of each headland (θ_h) and identified 3 possible orientations relative to beach aspect (inwards, perpendicular and outward). The various symmetrical and asymmetrical combinations of these resulted in 6 possible headland orientation types (H1–H6, Figure 2.5a). The dominant headland orientations were H6 (58 % total, < 75 % regionally), H2 (29 % total, < 40 % regionally), H1 (10 % total, < 20 % regionally); fewer occurrences observed of H3 (2 % total, < 7.5 % regionally), H5 (1 % total, < 10 % regionally) and no occurrences of H4 (Figure 2.5b).

There were minor differences in the proportions of each headland orientation across the 6 regions (Figure 2.5d). Shadowed beach length (X_{sh}) ranged from 0 to 100 % with a mean of 34 % of total alongshore beach length impacted by shadowing (Figure 2.4e). The greatest regional mean X_{sh} was in COR and SC, while NSW and CP exhibited the smallest mean X_{sh}. Meanwhile,

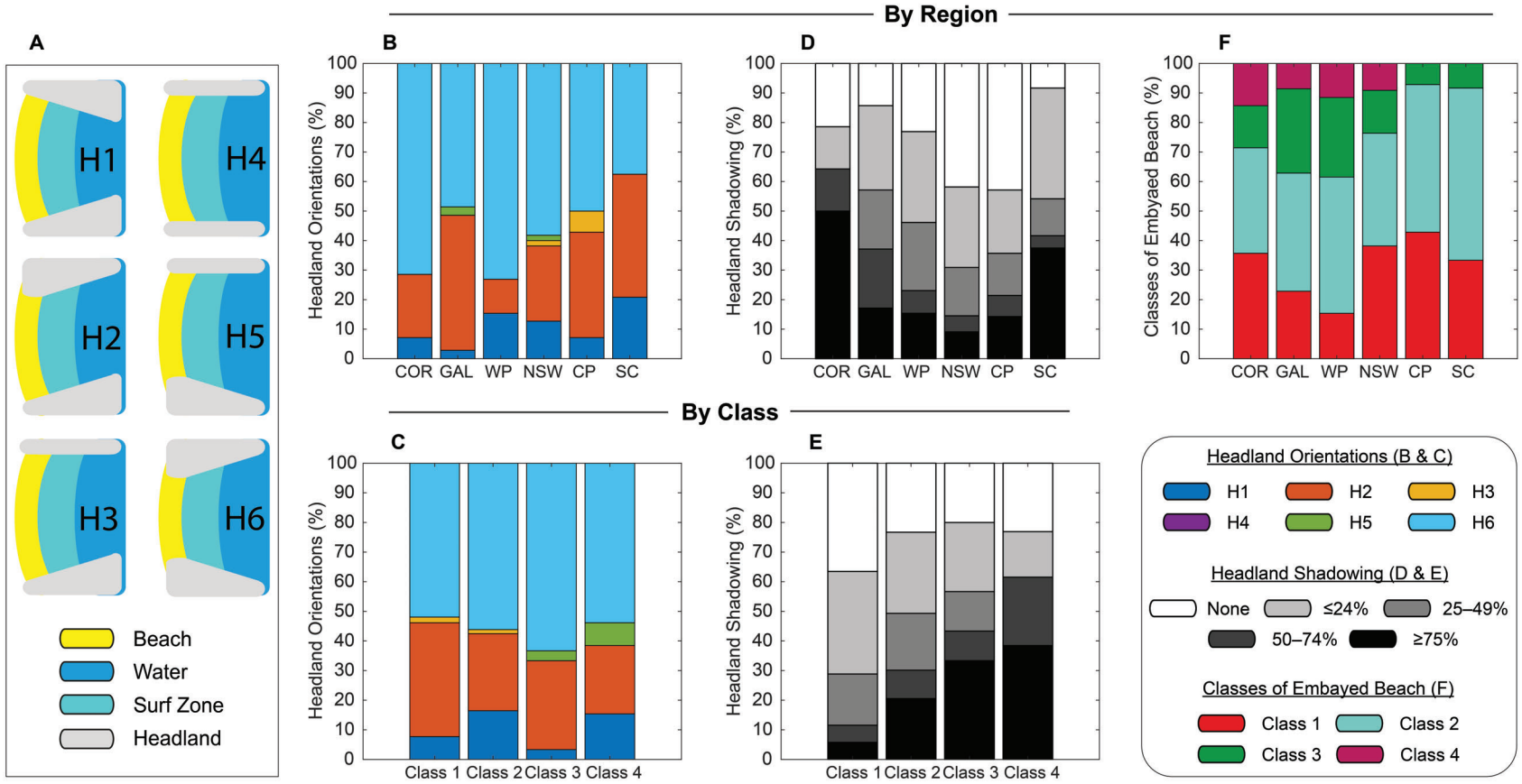

Figure 2.5: Headland orientations types (H1–H6) (a), headland origination type (%) by region (b) and by class (c), headland shadow beach length (X_{sh}) categories (%) by region (d) and by class (e), and, different classes of embayed beach proportions (%) by region (f).

common shadowing categories were > 75 % X_{sh} represented 20 % (n = 33), 24.9–0.1 % X_{sh} represented 27.5% (n = 47) and 0 % X_{sh} illustrated 27 % (n = 45) of embayed beaches (Figure 2.5d).

2.4.2 Embayed Morphometric Parameter (γ_e)

There is a wide range of γ_e values found across the 168 embayed beaches with the lowest γ_e is 0.36 at Mataora beach, CP (Figure 2.3h), the highest is 2.30 at Clovelly beach, NSW (Figure 2.3f) and mean γ_e is 0.87. On average GAL, COR and WP had the similar and high means γ_e, NSW is transitional, and CP and SC have the lowest mean γ_e values (Figure 2.4f, 2.5f). For the highest and lowest recorded γ_e, a was equal to 5 R_o and 0.16 R_o respectively; while, those beaches γ_e > 0.99 typically had a > 4 R_o.

2.4.2.1 Classes of Embayed Beach

We identified four statistically distinct embayment classes using k-means cluster analysis for γ_e values (Figure 2.5f, Figure 2.6b; Table 2.1). Regional beach classification yielded 15–43 % of beaches in Class 1 (e.g., Crantock beach, COR, Figure 2.3e), 36–58 % in Class 2 (e.g., Meio beach, SC, Figure 2.3k), 7–29 % in Class 3 (e.g., Mataora beach, CP, Figure 2.3h), and 0–14 % in Class 4 (e.g., Wattamolla beach, NSW, Figure 2.3l). Class 1 embayments had the largest area, wide R_o, low embayment indention (a), and headland shadowing effects are minimal (Figure 2.7a). Class 2 embayments have lower R_o, higher a, and greater headland influence than Class 1 (Figure 2.7b). Class 3 embayments have similar R_o and a with moderate-high headland effects (Figure 2.7c). Finally, Class 4 embayments are the most embayed beaches, with the highest a and the narrowest R_o; these are the most deeply-indented embayed beaches where headland effects dominate beach morphodynamics (Figure 2.7d). Breaking wave height (H_b) (Eq. 2.1) is greatest for Class 1 beaches, and lowest for Class 4 embayments (Table 2.1). The planform ratio, I (Eq. 2) and the proportion of embayments considered deep ($a < R_o$) increases with from Class 1 to 4.

Headland orientations (H1–H6) generally had similar proportions for each class of embayed

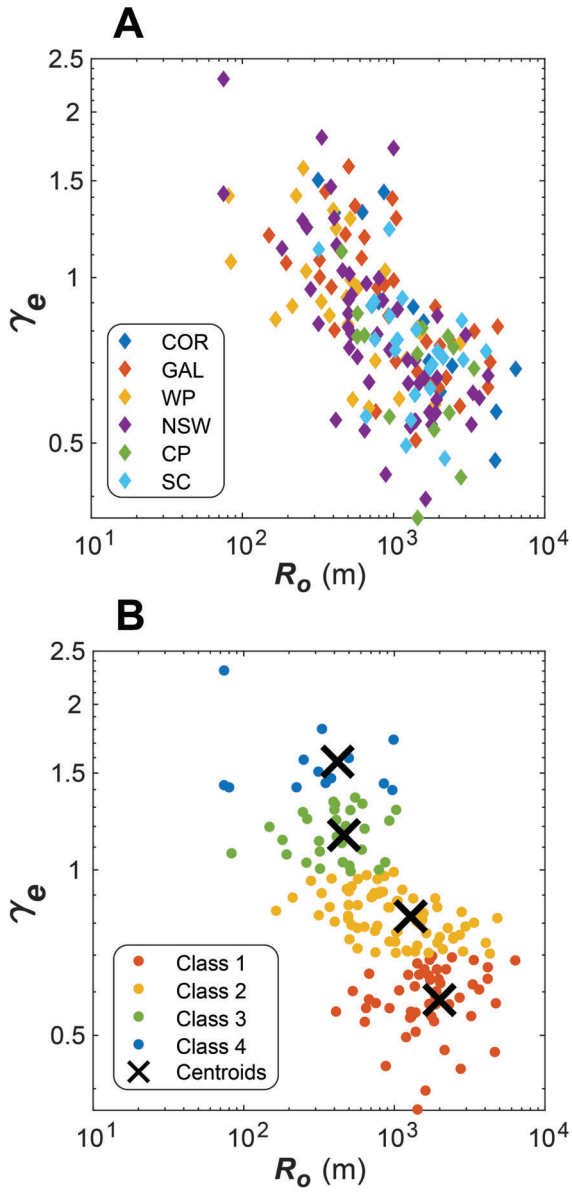

Figure 2.6: (a) Embayment morphometric parameter ($_e$) against width between headlands (R_o) ($R^2 = -0.49$; $p - value$ 0.001) grouped by region. (b) Classes of embayed beach with centroid (mean) denoted by 'x'.

beach (Figure 2.5a and c). The most common types for all classes were H2 (50–60 %), H6 (25–40 %) and H1 (5–15 %) (Figure 2.5c). Class 1 and 2 had minimal percentages of H3, while Class 3 and 4 had minimal percentages of H5 (Figure 2.5c). Moreover, the proportions of embayed beaches that exhibited headland shadowing greater than half of total alongshore beach length increased from 10 % of sites in Class 1 to 60 % of Class 4 (Figure 2.5d). Most notably, embayed beaches with over 75 % of beach length shadowing, increased from 6 % in Class 1 to

Table 2.2: Comparison of mean characteristics from the 4 classes of embayment beach.

Defining Parameters	**Class 1**	**Class 2**	**Class 3**	**Class 4**
Number of beaches (n [% of N])	52 [31]	73 [43]	30 [18]	13 [8]
γ_e mean (Eq. 2.4)	0.58	0.82	1.16	1.57
γ_e range	0.36–0.69	0.70–0.98	0.99–1.34	1.39–2.30
Breaker wave height, H_b (m) (Eq. 2.1)	1.49	1.36	1.30	1.00
Embayment indentation, a (m)	575	656	426	550
Width between headlands, R_o (m)	1994	1283	463	419
Alongshore beach length, X_d (m)	1713	749	222	50
Embayment area, A_e (x10^6 m^2)	1.33	1.15	0.19	0.17
Total embayment length, S_l (m)	2661	2270	1084	1265
Shadowed beach length, X_{sh} (% [m])	20 [437]	36 [564]	45 [125]	55 [56]
Parameter (δ') (Eq. 2.3)	26	44	26	54
Parameter (δ') range	5–115	4–953	4–202	10–216
Planform ratio (I) (Eq. 2.2)	0.29	0.56	0.91	1.71
Beach/ total embayment length (X_d/S_l)	0.62	0.45	0.24	0.11
Total embayment length/width (S_l/R_o)	1.36	1.92	2.31	3.88
Shallow indentation, $a > R_o$ (%)	0	3	27	85
Deep indentation, $a < R_o$ (%)	100	97	73	15

38 % in Class 4; while shadowing over 50 % increased from 6 % in Class 1 to 23 % in Class 4. Approximately 20 % of beaches in each class had negligible headland shadowing; except Class 1, representing the least embayed beaches, where 37 % of beaches had no headland shadowing.

2.5 Discussion

2.5.1 Degree of Embaymentisation

The new classification based on our proposed embayment morphometric parameter (γ_e) is a significant step in categorising embayed beaches on local, regional and global scales (Table 2.1, Figure 2.3). For instance, it extends the work by Hsu et al (1989) in highlighting how some H1, H2 and H6 headland orientations do not encompass parabolic shapes and do not follow I from irregular headland morphologies and orientations (Figure 2.3d, j, l; Figure 2.9i). The four classes defined across all regions are characterised by morphometric measurements that centre around defined ranges of γ_e and that, therefore, have similar embayment characteristics, and

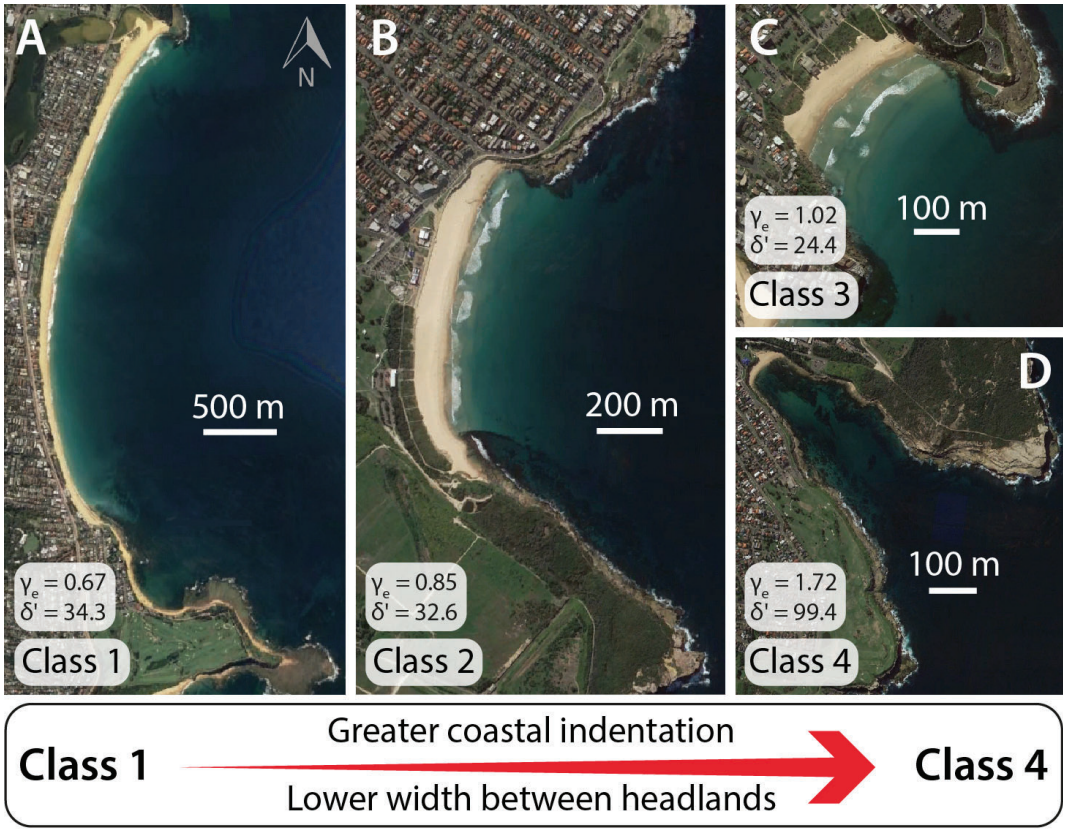

Figure 2.7: (a) Example of each class of embayed beach from NSW, Australia. Value of $_e$ and δ' are noted with general trends of shallow to deep embayment indentation and wide headlands width to narrow width highlighted. (a) Collaroy-Narrabeen, (b) Maroubra, (c) Freshwater and, (d) Malabar representing Class 1 through 4. Images modified from Google Earth and available in Fellowes et al., (2018).

an expected typical morphodynamic behaviour (Table 2.1, Figure 2.6b, Figure 2.7). As Class 4 represents the most embayed beaches, we can predict that the geological control on beach morphodynamics through headland shadowing increases with γ_e and is maximum for Class 4 (Figure 2.5e). This is related to the effects of wave refraction around headlands (Bryan et al., 2013; Castelle and Coco, 2012; Klein and Menezes, 2001), in conjunction with the control that the depth of indentation of the embayment has on wave dissipation (Blossier et al., 2016; Elshinnawy et al., 2018b; Harley et al., 2015), combined with headland symmetry/asymmetry effects on alongshore wave-energy gradients (Daly et al., 2014; McCarroll et al., 2016), beach rotation (Harley et al., 2015) and underlying geology (Jackson and Cooper, 2009; Loureiro et al., 2013).

In addition to impacts on wave shadowing, we expect the embayment morphometric parameter to also allow the surf zone morphology and circulation to be inferred. Based on this we suggest that Class 1 and 2 beach morphology, representing the least embayed beaches, will be the most dynamic (Harley et al., 2015). For example, as shown by the dynamic nature of (Class 1) Narrabeen beach revealed by over 40 years of monitoring, that this beach is exposed to swell waves and typically has open beach surf zone morphology away from the headlands (Harley et al., 2015; Figure 2.7a). Additionally, Scott et al (2016) found that beach response and surf zone circulation at beaches in north Cornwall varied with different embayment geometries (represented here by the classes of embayed beach) and embayment exposure (aspect) to swell waves. Class 1 and 2 beaches would have the largest sand budgets and typically have multiple rip currents away from the headland limits as well as headland rip currents (Castelle et al., 2016; Gallop et al., 2009; Loureiro et al., 2012b; Short and Masselink, 1999). During storms, Class 2-4 may switch to headland-dominated cellular circulation (Castelle and Coco, 2013; Short and Masselink, 1999) or experience greater erosion adjacent to headlands (Bryan et al., 2013; Harley et al., 2014). Although this cellular circulation response is dependent of the embayment aspect and exposure to swell waves (Castelle and Coco, 2012; Scott et al, 2016). Greater embayment indentations, here defined as Class 3 or 4, may be naturally protected by their degree of embaymentisation (i.e., narrow width between headlands, shallower bathymetries adjacent to headlands and higher γ_e) from smaller sediment budgets if retained within the embayment (Horta et al., 2018). For instance, Class 3 beaches may be susceptible to mega-rip formation as modelled in Castelle and Coco (2012) on sites like Tamarama beach, NSW (Figure 2.9h). While, Class 4 beaches may be protected by headland lengths that remove most wave energy at the shoreline shown by the lower H_b (Eq. 2.1) calculated here for each class (Table 2.1) (Loureiro et al., 2012a; Castelle and Coco, 2013). Class 4 beaches have greater headland and indentation influences on wave energy that reaches the shoreline, evident by no surf zone rip currents (e.g., Wattamolla beach, NSW; Figure 2.3l) and are potentially at less risk to storm erosion when compared to the more exposed beaches with lower indentation or headland influences in Class 1 and 2 (Horta et al., 2018).

2.5.1.1 Comparison with Previous Classification (δ')

Here we compare the widely used parameter δ' (Short and Masselink, 1999), which classifies the general pattern of surf zone circulation, with our embayment morphometric parameter γ_e (Figure 2.8). Short and Masselink (1999) stated that embayed beaches fit into 3 circulation states (Eq. 3). While, Castelle and Coco (2012) showed through a model that under symmetrical headland orientation conditions, some embayed beaches do abide to this classification (δ'). Adding, that there is potential for δ' to overestimate the number of surf zone rip currents and overall circulation state for deeply embayed beaches with small-area, or asymmetrical headlands, here described as Class 3 or 4 (Figure 2.8). There is a lack of definition of the boundaries between the three circulation states of δ' (Castelle and Coco, 2012), compared with γ_e where each class is characterised in Table 2.1. When we applied δ' to our 168 beaches we found a greater range of values (δ' = 1–953) than the original range (δ' = 1–48) presented in Short and Masselink (1999). Comparisons of δ' show that deep indentation embayed beaches (high γ_e) can be incorrectly classified as normal or transitional (Figure 2.8). In fact, Figure 2.8 shows very clearly how our classes obtained using γ_e spread over the three circulation states defined by Short and Masselink (1999) strengthening the use of γ_e over δ'.

There are several cases where δ' incorrectly assigns normal circulation for beaches in Class 3 and 4 (Figure 2.8); this happens for small-area and narrow headland embayments and is a concern for this method (Figure 2.9c, e, g, i, j, o and l). On the other hand, existing literature (Bowman et al., 2009; Castelle and Coco, 2012; Horta et al., 2018; Loureiro et al., 2012b) indicates that normal circulation is only possible for the wide and large-area embayments that γ_e classifies as Class 1 and 2 (e.g., Figure 2.9a, b, d, f, k, m and p). Figure 2.9 also shows examples where δ' yielded cellular or transitional circulation to beaches that are not deeply embayed and that our classification correctly classified as Class 1 or 2 (e.g., Figure 2.9e, g, and n). Our methodology and new classes of embayed beaches transcend any circulation assignment issues and unlike previous classification attempts, we base our classifications and γ_e on inherited embayment geometries and literature to deduce beach morphodynamics and this is supported by H_b (Eq. 1) calculated for each class (Table 2.1).

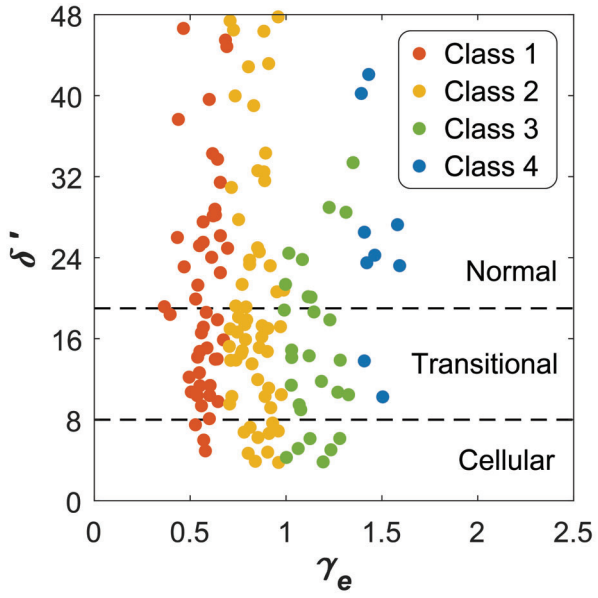

Figure 2.8: Comparison between δ' and γ_e with 4 classes of embayed beaches and circulation states labelled from Short and Masselink (1999). Note, that this subset is limited to $\delta' = 48$ allowing comparison with Short and Masselink

2.5.2 Regional variability in embayed beach morphology

Applying the embayment morphometric parameter (γ_e) to 6 regions globally shows there are some typical embayment settings and morphometrics that exist across different regions, independent of the wave climate or tidal regimes. For instance, we found that γ_e, headland shadowing and headland orientations can be similar for embayed beaches that are entirely of different proportions, see for example the small Silveira beach ($\gamma_e = 0.72$, Figure 2.9d) and the large Dunas de Corrubedo beach ($\gamma_e = 0.70$ Figure 2.9b). Comparisons between regions show that Class 1 and 2 encompass most of the beaches in all the regions studied, while Class 3 and 4 show greater variability (Figure 2.5f). Class 3 (e.g., Tamarama beach, Figure 2.9h) exists in all regions, with GAL and WP showing the largest proportions of Class 3 beaches. Finally, Class 4 beaches do not exist on CP or SC and represent small percentages of the remaining study regions; only in COR the percentage of Class 4 beaches is similar to the percentage of Class 3 beaches (Figure 2.5f). Although all the regions studied are on tectonically trailing edge margins, the underlying geology combined with the atmospheric and wave climate, provide a range of conditions that reflect the regional distribution of classes (Figure 2.5f). This may be

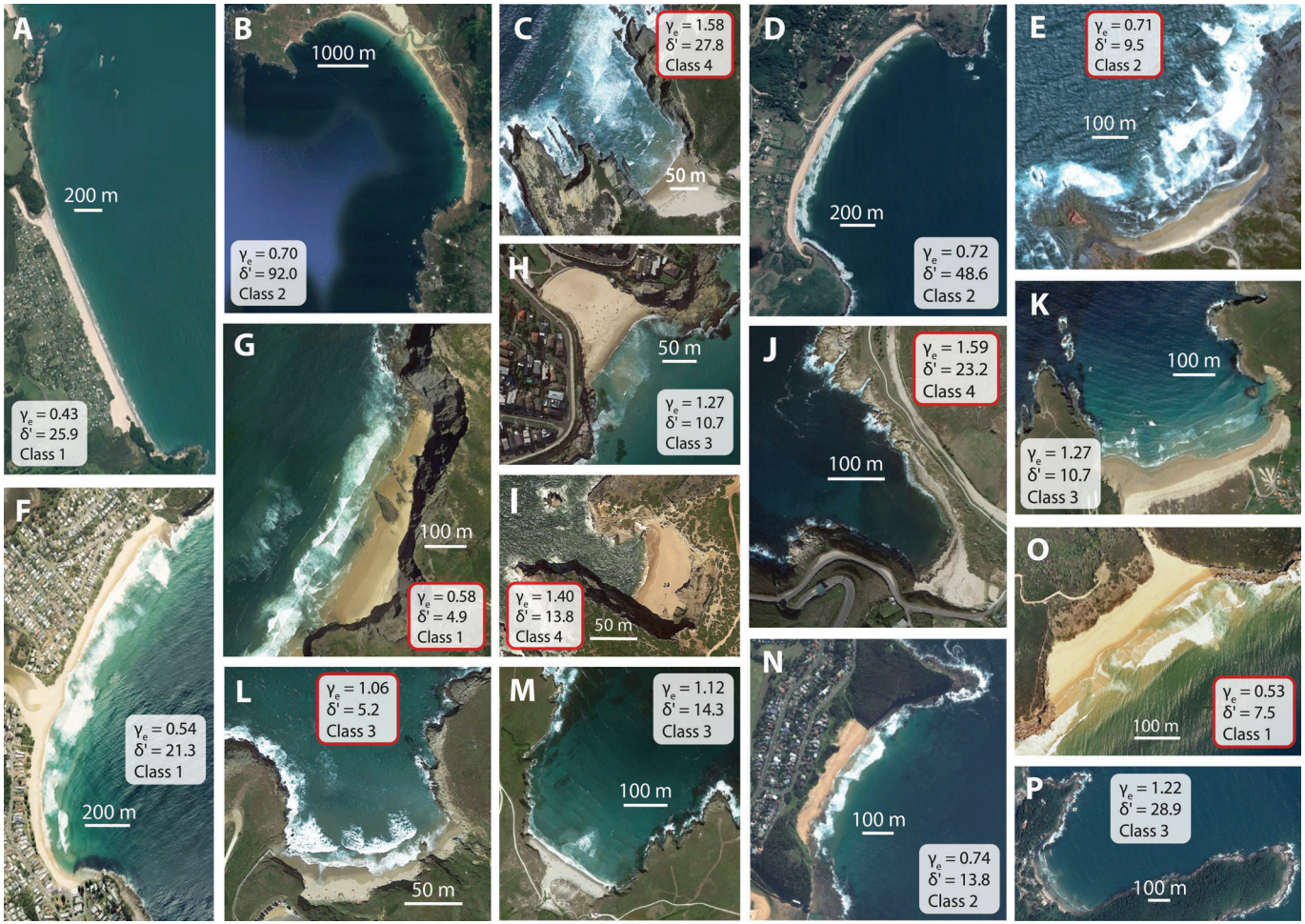

Figure 2.9: Embayed beaches subjected to δ' (Eq. 2.3) and γ_e (Eq. 2.4). Red boxes indicate beaches where δ' do not match the classes or predicted circulation states. (a) Whiritoa, CP, (b) Dunas de Corrubedo, GAL, (c) Carvalhal, WP, (d) Silveira, SC, (e) Ponta Ruiva, WP, (f) Avoca, NSW, (g) Mouranitos North, WP, (h) Tamarama, NSW, (i) Carneiro, WP, (j) Bens, GAL, (k) Pantin, GAL, (l) San Miro, GAL, (m) Seaia, GAL, (n) Turimetta, NSW, (o) Tallows, NSW, (p) Retiro dos Padres, SC. Images modified from Google Earth and available in Fellowes et al., (2018).

further attributed to regional configurations of river catchments, valleys, and headlands, among others.

The GAL coastline has the deepest indentations for its embayed beaches (high γ_e) and a high proportion (38 %) of Class 3 and 4 sites (Figure 2.5f), which is likely due to the presence of long estuaries (rias) or catchments that flow out to deeply-indented embayments, on the granitic coast with high-energy wave climate (Iglesias et al., 2009b; Méndez and Vilas, 2005). Similar conditions occur on the granitic coast of Cornwall with many long river valleys that incise the coast (Masselink et al., 2016; Prodger et al., 2016b; Scott et al., 2016) creating large proportions of Class 3 and 4 beaches, but also large river catchments that result in a larger proportion of Class 1 beaches. On the contrary, the high proportion of Class 3 and 4 embayments in WP (Figure 2.5f) is probably related to the relatively soft coastline (limestone-dolomite; Marques, 2009) with large valley formations exposed to high energy wave climate (Horta et al., 2018; Loureiro et al., 2012b). Similarly, the presence of Class 3 and 4 beaches in NSW can also be related to the soft headland geology dominated by quartz sandstone (Wright and Thom, 1977) and the relatively high wave energy. On the other hand, there are two regions, SC and CP, that have no Class 4 beaches and can therefore be considered as less embayed. In SC it may be attributed to the large river valleys and wide estuarine systems, that produce wide embayments on the igneous coastal geology (Horn and Diehl, 2004); and in CP it is likely due to the hard-igneous geology (Adams et al., 1994). The underlying geology and atmospheric and wave climates are obviously of first-order importance controlling the shape of coastlines around the world. However, our classification works independently of the geology/climate forcing the shape of the embayments. Future research should address the links between the classes and the geology and climates.

2.5.3 Headland Orientations

Headland orientations across the regions are separated into 6 headland orientations from H1 to H6 (Figure 2.5a). Over 58 % of all the embayed beaches in our study have the H6 headland orientation. The inherent location of many embayed beaches at the mouth of drowned river valleys and as estuarine-barrier systems, where $R_o > X_d$ as a general rule, have been suggested

to be the reason for the dominance of H6 headland orientations (Bishop and Cowell, 1997); this is also supported by the dominance of Class 1 and 2 beaches across all regions (Figure 2.5f). Embayed beaches with asymmetrical headland orientations or one headland that encourages greater headland shadowing than the other (e.g., Carnota beach, Figure 2.3c) may be subjected to an alongshore energy-gradient in waves and beach response. This was identified by McCarroll et al. (2016) who showed that each headland within an embayment can contribute a different amount of headland impact on the resulting inter-embayment wave dynamics during modal and storm conditions. Moreover, headland orientations that encourage less headland refraction and shadowing (H6) may provide less protection from swell waves when compared to H1 morphologies and in extreme events may result in greater beach response (George et al., 2015; Hsu and Evans, 1989; Klein et al., 2010). The broad-range of headland orientations presented here may relate to the geology of the regions, whereby the headland composition may dictate headlands protrusion and orientations and the embayment indentation (George et al., 2015). Greater understanding of embaymentisation, headland morphologies and orientations are fundamental in determining short and medium-term beach morphodynamics and for coastal embayment management (Thom et al., 2018).

2.6 Conclusions

We have developed a new embayment morphometric parameter (γ_e) to quantify the degree of embaymentisation on swell-dominated beaches, which is a function of the embayment indentation (a) and the embayment area (A_e) measured from open-access imagery. K-means cluster analysis identified four classes using γ_e (0.36–2.30), from the least embayed beaches (Class 1) to the most embayed beaches (Class 4). Our classification was able to classify the wide range of embayed beaches studied, improving on previous classifications (δ') (Short and Masselink, 1999) and embayment morphometric analyses (I) (Hsu et al., 1989) which are bound to idealistic embayment geometries and do not allow for the inclusion of irregular embayment shapes and areas, high indentation or asymmetrical headlands orientations. Furthermore, our classification can also be used to infer typical surf zone circulation based of

embayment geometries where on occasions previous classifications encountered problems. The global assessment of 168 swell-dominated beaches from 6 regions highlighted that the large variability in embayment and headland orientations is independent of the wave climate or tidal regimes. Class 2 (43 %, n = 73) was the most common globally, representing embayed beaches with low-moderate headland influence from their embayment morphology and Class 4 were the least common (8 %, n = 13). The most embayed regions with the largest proportion of Class 3 and 4 beaches (high γ_e, great headland influence and indentation) are in Galicia (Spain) and Cornwall (UK). The least embayed regions (low γ_e) are Coromandel Peninsula (NZ) and Santa Catarina (Brazil), with no or low occurrences of embayed beaches in Class 3 and 4. These variations may be attributed to the swell conditions and the coastal geology. To complement the classification model and morphometric assessment, we compare 6 identified headland orientations from beach aspect (H1–H6). The most common (58 %, n = 97) headland orientations are outwards from the beach (H6), associated with embayed beaches at the mouths of drowned rivers or catchments. These are more exposed to more wave energy and have potential for greater morphological response compared to headland orientation inwards onto the beach (H1) that encourages more headland shadowing and reduce wave energy. Determining morphological processes from our methods will lead to effective and targeted vulnerability assessment for many embayed beaches under a broad-range of embayment geometries, swell and tidal regimes.

2.7 Acknowledgements

TEF's funding is from the Macquarie University Research Training Programme and AV-C's Re-Entry Fellowship from Women in Science at the University of Sydney.

2.8 Data Availability

Datasets related to this article can be found at http://dx.doi.org/10.17632/c5bxpgbdr2.1, an open-source online data repository hosted at Mendeley Data (Fellowes et al., 2018).

2.9 References

Adams, C.J., Graham, I.J., Seward, D., Skinner, D.N.B., Moore, P.R., 1994. Geochronological and geochemical evolution of late Cenozoic volcanism in the Coromandel Peninsula, New Zealand. New Zealand Journal of Geology and Geophysics 37, 359-379.

Araújo, C.E., Franco, D., Melo, E., Pimenta, F., 2003. Wave regime characteristics of the southern Brazilian coast, Proceedings of the sixth international conference on coastal and port engineering in developing countries, COPEDEC VI, Colombo, Sri Lanka, Paper, p. 15.

Bishop, P., Cowell, P.J., 1997. Lithological and Drainage Network Determinants of the Character of Drowned, Embayed Coastlines. The Journal of Geology 105, 685-700.

Blossier, B., Bryan, K.R., Daly, C.J., Winter, C., 2016. Nearshore sandbar rotation at single-barred embayed beaches. Journal of Geophysical Research: Oceans 121, 2286-2313.

Bowman, D., Guillén, J., López, L., Pellegrino, V., 2009. Planview Geometry and morphological characteristics of pocket beaches on the Catalan coast (Spain). Geomorphology 108, 191-199. Bryan, K.R., Foster, R., MacDonald, I., 2013. Beach Rotation at Two Adjacent Headland-Enclosed Beaches. Journal of Coastal Research S65(2), 2095-2100.

Castelle, B., Coco, G., 2012. The morphodynamics of rip channels on embayed beaches. Continental Shelf Research 43, 10-23.

Castelle, B., Coco, G., 2013. Surf zone flushing on embayed beaches. Geophysical Research Letters 40, 2206-2210.

Castelle, B., Scott, T., Brander, R.W., McCarroll, R.J., 2016. Rip current types, circulation and hazard. Earth-Science Reviews 163, 1-21.

Costas, S., Alejo, I., Vila-Concejo, A., Nombela, M.A., 2005. Persistence of storm-induced morphology on a modal low-energy beach: A case study from NW-Iberian Peninsula. Marine Geology 224, 43-56.

Daly, C.J., Bryan, K.R., Winter, C., 2014. Wave energy distribution and morphological development in and around the shadow zone of an embayed beach. Coastal Engineering 93, 40-54.

Duce, S., Vila-Concejo, A., Hamylton, S.M., Webster, J.M., Bruce, E., Beaman, R.J., 2016. A morphometric assessment and classification of coral reef spur and groove morphology. Geomorphology 265, 68-83.

Elshinnawy, A.I., Medina, R., González, M., 2018a. Dynamic equilibrium planform of embayed beaches: Part 1. A new model and its verification. Coastal Engineering 135, 112-122.

Elshinnawy, A.I., Medina, R., González, M., 2018b. On the influence of wave directional spreading on the equilibrium planform of embayed beaches. Coastal Engineering 133, 59-75.

[*dataset*] Fellowes, T.E., Vila-Concejo, A., Gallop, S.L., 2018. Embayed Beach Morphometrics Dataset, 1 ed, Mendeley Data, http://dx.doi.org/10.17632/c5bxpgbdr2.1

Gallop, S.L., Bryan, K.R., Coco, G., 2009. Video Observations of Rip Currents on an Embayed Beach. Journal of Coastal Research S56(1), 49-53.

Gallop, S.L., Bryan, K.R., Coco, G., Stephens, S.A., 2011. Storm-driven changes in rip channel patterns on an embayed beach. Geomorphology 127, 179-188.

George, D.A., Largier, J.L., Storlazzi, C.D., Barnard, P.L., 2015. Classification of rocky headlands in California with relevance to littoral cell boundary delineation. Marine

Geology 369, 137-152. Gorman, R.M., Bryan, K.R., Laing. A.K., 2003. Wave hindcast for the New Zealand region: deep-water wave climate. New Zealand Journal of Marine and Freshwater Research 37, 589-612.

Harley, M.D., Andriolo, U., Armaroli, C., Ciavola, P., 2014. Shoreline rotation and response to nourishment of a gravel embayed beach using a low-cost video monitoring technique: San Michele-Sassi Neri, Central Italy. Journal of Coastal Conservation 18, 551-565.

Harley, M.D., Turner, I.L., Short, A.D., 2015. New insights into embayed beach rotation: The importance of wave exposure and cross-shore processes. Journal of Geophysical Research: Earth Surface 120, 1470-1484.

Holman, R.A., Symonds, G., Thornton, E.B., Ranasinghe, R., 2006. Rip spacing and persistence on an embayed beach. Journal of Geophysical Research: Oceans 111, C01006.

Horn Filho, N., Diehl, F., 2004. Santa Catarina coastal province, Brazil: geology, geomorphology and paleogeography. Journal of Coastal Research, S39(1), 311-315.

Horta, J., Oliveira, S., Moura, D., Ferreira, Ó., 2018. Nearshore hydrodynamics at pocket beaches with contrasting wave exposure in southern Portugal. Estuarine, Coastal and Shelf Science 204, 40-55.

Hsu, J., Evans, C., 1989. Parabolic Bay Shapes and Applications. Proceedings of the Institution of Civil Engineers 87, 557-570.

Hsu, J.R.C., Silvester, R., Xia, Y.M., 1989. Static Equilibrium Bays: New Relationships. Journal of Waterway, Port, Coastal, and Ocean Engineering 115, 285-298.

Iglesias, G., Carballo, R., 2009. Wave energy potential along the Death Coast (Spain). Energy 34, 1963-1975.

Iglesias, G., López, M., Carballo, R., Castro, A., Fraguela, J.A., Frigaard, P., 2009a. Wave energy potential in Galicia (NW Spain). Renewable Energy 34, 2323-2333.

Iglesias, G., López, I., Castro, A., Carballo, R., 2009b. Neural network modelling of planform geometry of headland-bay beaches. Geomorphology 103, 577-587.

Jackson, D.W.T., Cooper, J.A.G., 2009. Geological Control on Beach Form: Accommodation Space and Contemporary Dynamics. Journal of Coastal Research S56(1), 69-72.

Jackson, D.W.T., Cooper, J.A.G., del Rio, L., 2005. Geological control of beach morphodynamic state. Marine Geology 216, 297-314.

Jain, A.K., 2010. Data clustering: 50 years beyond K-means. Pattern Recognition Letters, 31, 651-666.

Klein, A.H.d.F., Ferreira, Ó., Dias, J.M.A., Tessler, M.G., Silveira, L.F., Benedet, L., de Menezes, J.T., de Abreu, J.G.N., 2010. Morphodynamics of structurally controlled headland-bay beaches in southeastern Brazil: A review. Coastal Engineering 57, 98-111.

Klein, A.H.d.F., Menezes, J.T.d., 2001. Beach Morphodynamics and Profile Sequence for a Headland Bay Coast. Journal of Coastal Research 17, 812-835.

Loureiro, C., Ferreira, O., Cooper, J.A.G., 2009. Contrasting Morphologic Behaviour at Embayed Beaches in Southern Portugal. Journal of Coastal Research S56(1), 83-87.

Loureiro, C., Ferreira, Ó., Cooper, J.A.G., 2012a. Extreme erosion on high-energy embayed beaches: Influence of megarips and storm grouping. Geomorphology 139, 155-171.

Loureiro, C., Ferreira, Ó., Cooper, J.A.G., 2012b. Geologically constrained morphological variability and boundary effects on embayed beaches. Marine Geology 329, 1-15.

Loureiro, C., Ferreira, Ó., Cooper, J.A.G., 2013. Applicability of parametric beach morphodynamic state classification on embayed beaches. Marine Geology 346, 153-164.

Marques, F., 2009. Sea cliff instability hazard prevention and planning: examples of practice in

Portugal. Journal Of Coastal Research, S56(1), 856-860.
Masselink, G., Austin, M., Scott, T., Poate, T., Russell, P., 2014. Role of wave forcing, storms and NAO in outer bar dynamics on a high-energy, macro-tidal beach. Geomorphology 226, 76-93.
Masselink, G., Castelle, B., Scott, T., Dodet, G., Suanez, S., Jackson, D., Floc'h, F., 2016. Extreme wave activity during 2013/2014 winter and morphological impacts along the Atlantic coast of Europe. Geophysical Research Letters 43, 2135-2143.
McCarroll, R.J., Brander, R.W., Turner, I.L., Van Leeuwen, B., 2016. Shoreface storm morphodynamics and mega-rip evolution at an embayed beach: Bondi Beach, NSW, Australia. Continental Shelf Research 116, 74-88.
Méndez, G., Vilas, F., 2005. Geological antecedents of the Rias Baixas (Galicia, northwest Iberian Peninsula). Journal of Marine Systems 54, 195-207.
Mortlock, T., Goodwin, I.D., McAneney, J., Roche, K., 2017. The June 2016 Australian East Coast Low: Importance of Wave Direction for Coastal Erosion Assessment. Water 9(2), 121.
Mortlock, T.R., Goodwin, I.D., 2016. Impacts of enhanced central Pacific ENSO on wave climate and headland-bay beach morphology. Continental Shelf Research 120, 14-25.
Palha, A., Mendes, L., Fortes, C.J., Brito-Melo, A., Sarmento, A., 2010. The impact of wave energy farms in the shoreline wave climate: Portuguese pilot zone case study using Pelamis energy wave devices. Renewable Energy 35, 62-77.
Pianca, C., Mazzini, P.L.F., Siegle, E., 2010. Brazilian offshore wave climate based on NWW3 reanalysis. Brazilian Journal of Oceanography 58, 53-70.
Prodger, S., Russell, P., Davidson, M., 2016a. Grain-size distributions on high energy sandy beaches and their relation to wave dissipation. Sedimentology 64(5), 1289-1302.
Prodger, S., Russell, P., Davidson, M., Miles, J., Scott, T., 2016b. Understanding and predicting the temporal variability of sediment grain size characteristics on high-energy beaches. Marine Geology 376, 109-117.
Reniers, A.J.H.M., Roelvink, J.A., Thornton, E.B., 2004. Morphodynamic modeling of an embayed beach under wave group forcing. Journal of Geophysical Research: Oceans 109(C1), C01030.
Scott, T., Masselink, G., O'Hare, T., Saulter, A., Poate, T., Russell, P., Davidson, M., Conley, D., 2016. The extreme 2013/2014 winter storms: Beach recovery along the southwest coast of England. Marine Geology 382, 224-241.
Scott, T., Masselink, G., Russell, P., 2011. Morphodynamic characteristics and classification of beaches in England and Wales. Marine Geology 286, 1-20.
Short, A.D., 1985. Rip-current type, spacing and persistence, Narrabeen Beach, Australia. Marine Geology 65, 47-71.
Short, A.D., Trenaman, N., 1992. Wave climate of the Sydney region, an energetic and highly variable ocean wave regime. Marine and Freshwater Research 43, 765-791.
Short, A.D., Masselink, G., 1999. Embayed and structurally controlled embayed beaches, in: Short, A.D., (Eds.), 1999. Handbook of beach and shoreface morphodynamics. Wiley, Chichester, pp. 230-250.
Silvester, R., 1985. Natural headland control of beaches. Continental Shelf Research 4, 581-596.
Thom, B., Roy, P.S., 1985. Relative sea levels and coastal sedimentation in southeast Australia in the Holocene. Journal of Sedimentary Research 55(2), 257-267.
Thom, B.G., Eliot, I., Eliot, M., Harvey, N., Rissik, D., Sharples, C., Short, A.D., Woodroffe,

C.D., 2018. National sediment compartment framework for Australian coastal management. Ocean Coastal Management 154, 103-120.

Valiente, N.G., Masselink, G., Scott, T., Conley, D., McCarroll, R.J., 2019. Role of waves and tides on depth of closure and potential for headland bypassing. Marine Geology 407, 60-75.

Wright, I.C., 1992. Shallow structure and active tectonism of an offshore continental back-arc spreading system: the Taupo Volcanic Zone, New Zealand. Marine Geology 103, 287-309.

Wright, L., Thom, B., 1977. Coastal depositional landforms: a morphodynamic approach. Progress in Physical Geography 1(3), 412-459.

3

The influence of embayed beach exposure and headland shadowing on storm erosion and recovery

This chapter is based on the following publication (in preparation):

Fellowes, T.E., Vila-Concejo, A., Gallop, S.L., Harley, M.D., Short, A. D., *In Prep*. The influence of embayed beach exposure and headland shadowing on storm erosion and recovery.

3.1 Abstract

Embayed beaches come in a range of shapes, sizes and orientations all of which influence beach morphodynamics. Headlands on embayed beaches can result in alongshore gradients in wave energy, with a protected (shadow) zone in the lee of the headland grading to a more exposed zone away from the headland. These wave energy gradients correspond to alongshore variation in the morphodynamic beach states commonly seen on embayed beaches. Moreover, the location and proportion of the energy gradients shift with changes wave direction, particularly during storms. A definition is needed to define boundaries between exposed and protected zones to determine and predict embayed beach storm responses and recovery rates. Here we present a simple trigonometry-based approach to quantify the boundary between exposed and protected embayed beach zones, as the shadow edge (X_{se}). This method uses headland geometry collected from open-access imagery, combined with storm wave direction, and can be applied to any embayed beach. We also investigate the impact of headland geometry and storm wave direction on embayed beach storm response and recovery, using results from monthly topographic beach surveys (2015–2019) at 9 embayed beaches in southeast Australia, combined with data from the literature from elsewhere in Australia, the United Kingdom and Portugal. Mean subaerial beach volume losses to eight high-energy storms in southeast Australia were 7 times higher in exposed zones (43 m^3/m) than protected zones (6 m^3/m). Storm frequency, embayment geometries and degree of embaymentisation dictates the storm response and recovery rates. Mean storm recovery rates were consistent across all higher energy low-moderate embayment-controlled beaches at 0.22 $m^3/m/day$ and for lower energy high embayment-controlled beaches was 0.08 $m^3/m/day$. We propose that there is an embaymentisation threshold indicating that highly embayment-controlled beaches are the most vulnerable to storms due to a long lag in recovery rates.

3.2 Introduction

Embayed beaches occur globally on hill and cliff dominated coastlines (Short and Masselink, 1999). They are bound by physical structures such as headlands that define the extent of the embayment (Hsu and Evans, 1989). Headlands have an important influence on alongshore connectivity, where embayed beaches with headlands extending seaward of the surf zone commonly retain sediment within the embayment with little or no littoral sediment exchange (Bryan et al., 2013; Harley et al., 2015; Pitman et al., 2016). Headlands are also the primary regulator of incident waves and embayed beach morphodynamics (Short, 1978; Hsu and Evans, 1989; Loureiro et al., 2012b; Daly et al., 2014). Headlands and their associated rocky attachments such as reefs, platforms and islands (Short, 2010; Bryan et al., 2013) modify waves through shadowing, refraction and diffraction (Loureiro et al., 2012b; Burvingt et al., 2017); these effects are the most prevalent with oblique waves relative to headland aspect and impact alongshore morphodynamics (Silvester, 1985). This means that embayed beaches commonly have an alongshore gradient of wave energy, from exposed zones with relatively high wave energy to protected zones with relatively low wave energy in the lee of a shadowing headland (Castelle and Coco, 2012; Daly et al., 2014). This energy gradient largely drives alongshore beach morphodynamics and the nearshore morphology of embayed beaches (Daly et al., 2015; McCarroll et al., 2016; Burvingt et al., 2017). Shore-normal headlands typically shadow part of the beach from oblique waves, but high beach curvature and/or headlands that are oblique to the shoreline can also result in headland shadowing with shore-normal waves (Hsu and Evans, 1989). Additionally, changes in wave direction from storms or weather systems (e.g., El Niño Southern Oscillation, Southern Annular Mode) and headland shadowing can cause shoreline rotation by redistributing sediment within the embayment (Short and Masselink, 1999; Barnard et al., 2015).

Recent studies on the United Kingdom (Burvingt et al., 2017), Portugal (Loureiro et al., 2014), Brazil (Klein et al., 2010), Australia (Harley et al., 2011a) and New Zealand (Bryan et al., 2013) have built on the early works of Hsu and Evans (1989) and Short and Masselink (1999), working

towards determining the relationship between embayed beach settings, beach morphodynamics, erosion and recovery rates and circulation. These two early works formed a base that led to a better understanding of embayed beaches in relation to exposure to storms (Burvingt et al., 2017), circulation patterns and embayment settings (Castelle and Coco, 2012), definition of the depth of embayment closure (Valiente et al., 2019), characterisation of different headland types and by-passing processes (George et al., 2015) and the quantification of the degree of embaymentisation and headland orientation (Fellowes et al., 2019). This paper builds on the work of Fellowes et al. (2019) that established four classes of embayed beaches based on the degree of embaymentisation, from Class 1 (least embayment controlled) to Class 4 (most embayment controlled), which is expressed as the embayment morphometric parameter (γ_e),

$$\gamma_e = a/\sqrt{A_e} \tag{3.1}$$

where, a is embayment coastal indentation from the seaward headland extent to the active back-beach boundary and A_e is embayment area. Fellowes et al. (2019) also defined 6 key types of headlands based on their orientation and symmetry, ranging from two headlands with acute angles to beach aspect (H1) to two headlands with obtuse angles (H6), with the most common type (H6 = 58 %) from an assessment of 168 beaches globally; they further showed the proportion of the beach shadowed by headlands to dominant wave directions increases with embayment class.

Here we focus on comparing the storm response, and post-storm recovery rates of embayed beaches relative to their degree of embaymentisation (Class 1–Class 4) and headland orientation (H1–H6). The objectives are to: (1) compare how headland and embayment characteristics influence the morphological beach response to fair-weather and storm conditions; (2) determine how headlands and the degree of embaymentisation influences post-storm recovery of the subaerial beach; and (3) assess how headland shadowing impacts the morphodynamics in protected (shadowed in the lee of headlands) and exposed zones of embayed beaches. This will be achieved by integrating data from 9 beaches in New South Wales, Australia and 13 other beaches from existing literature.

3.2.1 Study area

This study focuses on 9 wave-dominated embayed beaches in southeast Australia, along the New South Wales (NSW) coast (Figure 3.1). The NSW coastline is characterised by hundreds of drowned river valleys with cliffs now separating the valleys and beaches partly filling the valleys forming sandy embayed beaches (Short, 1993; Bishop and Cowell, 1997; Thom et al., 2018). Seven of our sites are in the Sydney region, including Narrabeen-Collaroy (herein referred to as Narrabeen), Bondi, Tamarama, Bronte, Coogee, Maroubra and Malabar (Figure 3.1d–j; Table 3.1), with two sites (Moruya and Pedro) located on the South Coast (230 km south of Sydney) (Figure 3.1k–l). These 9 beaches represent a variety of embayed beach morphologies (Table 3.1) with beach lengths from 80 m to 3600 m. These sites represent the four classes of embayed beaches (Class 1–Class 4) and the 4 most common headland types (H2, H3, H4 and H6) defined by Fellowes et al. (2019). Note that the two absent headland types H1 and H4 are relatively rare, representing 10 % and 0 % of embayed beaches from a global assessment by Fellowes et al. (2019). Narrabeen, Bronte, Maroubra, Moruya and Pedro have an easterly beach aspect (α_{eb}), Tamarama, Coogee and Malabar face southeast, while Bondi faces south-southeast (Table 3.1). These beaches are typically in an intermediate beach state such as transverse bar and rip (TBR) or rhythmic bar and beach (RBB), with the exception of Coogee and Malabar that are reflective or low tide terrace (LTT) (Wright and Short, 1984; Short, 1993). All of these beaches are bound by two rocky headlands, many of which extend into submerged reefs (Figure 3.1). The NSW coast is micro-tidal (< 2 m). The Sydney region has mean offshore significant wave height (H_s) of 1.6 m, mean wave period (T_z) of 8 s, and a typical wave direction (θ_w) of 135° (Short and Trenaman, 1992; Harley et al., 2010). The South Coast has mean offshore H_s of 1.4 m, T_z of 6.1 s and θ_w of 130°. Both regions regularly experience storms, that have been previously defined from long-term the wave climate data as events with H_s > 3 m for a minimum 6 hour duration and storm independence of 24 hours (Shand et al., 2010). Storms can be generated year-round by mid-latitude cyclones, east coast cyclones and during summer by tropical cyclones and can arrive to the coast from north-east to south (Short and Trenaman, 1992; Mortlock and Goodwin, 2015). Storm frequency in the region is impacted by regional and

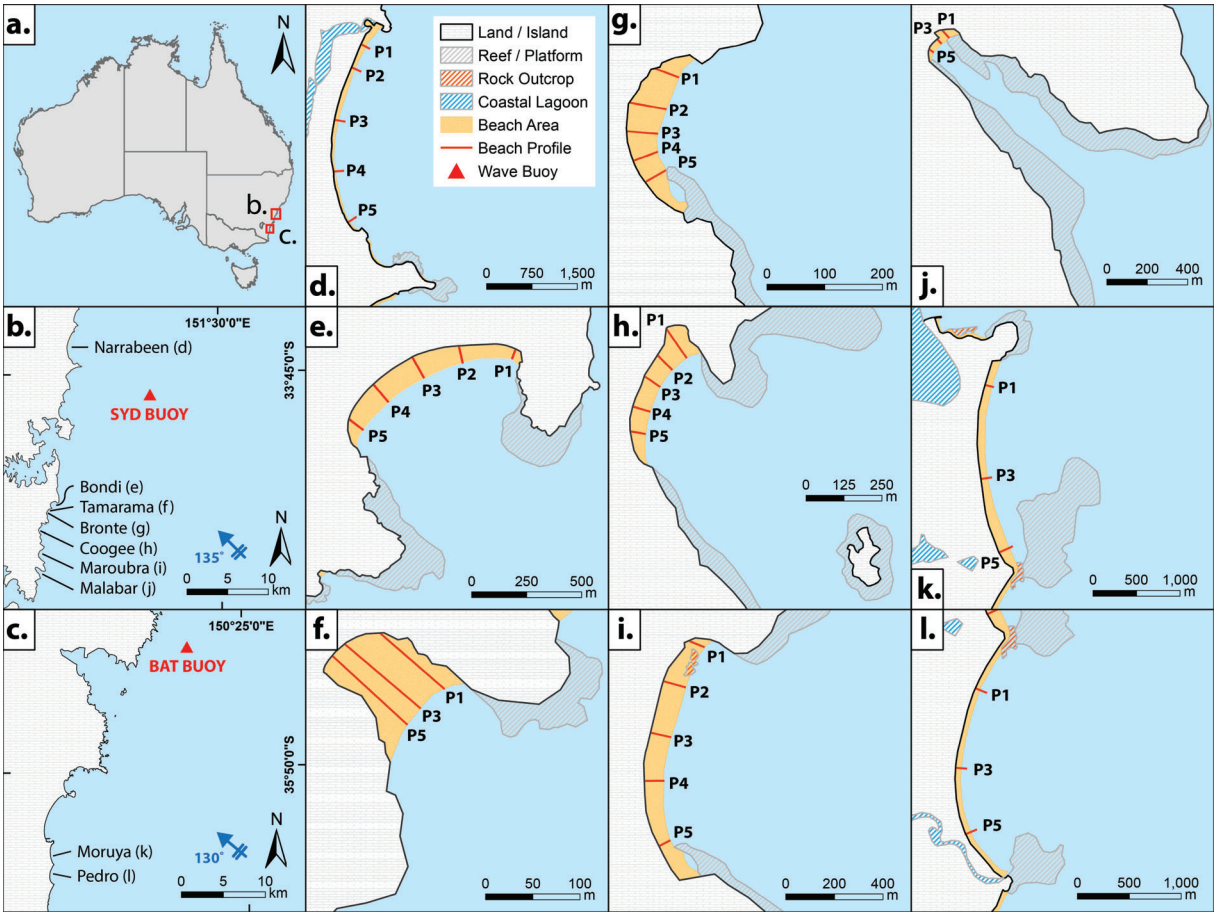

Figure 3.1: Location of beach sites with embayed beach class and headland type from Chapter 2. (a) Australian context, (b) Sydney region, (c) South Coast region, (d) Narrabeen (C1/H2), (e) Bondi (C2/H2), (f) Tamarama (C3/H6), (g) Bronte (C2/H6), (h) Coogee (C3/H2), (i) Maroubra (C2/H6), (j) Malabar (C4/H6), (k) Moruya (C1/H5), and (l) Pedro (C1/H3). Typical swell directions (blue arrow) and Waverider buoy locations are shown in (b) and (c).

Pacific-scale weather systems (Mortlock and Goodwin, 2016) and is significantly modified by the El Niño Southern Oscillation (ENSO), the Southern Annular Mode (SAM) and the Pacific Decadal Oscillation (PDO) (Barnard et al., 2015). Barnard et al. (2015) found that in NSW, the multivariate ENSO index (MEI) characterises El Niño (+MEI) as warm periods when storms were less frequent and beaches typically accreted, while La Niña (-MEI) was associated with cool periods when storm frequency is higher, and beaches typically eroded; we will also apply MEI to our study to differentiate stormy-periods from extended fair-weather periods.

Table 3.1: Beach sites and statistics including beach length X_d, beach aspect eb (bearing [degrees]), beach classes (C1–C4) and headland types (H1–H6), headland length X_{hl}, headland offset distance X_{off}, headland aspects α_{hl}, number of surveys, dates and survey method.

Region	Site	X_d (m)	α_{eb} [°]	Class	HL Type	X_{hl} north (m)	X_{hl} south (m)	X_{off} north (m)	X_{off} south (m)	α_{hl} north (ź)	α_{hl} south (ź)	n Surveys	First Survey	Last Survey	Survey Method
Sydney	Narrabeen	3600	E [98]	C1	H2	729	-77	2280	555	119	125	99	5/11/15	10/6/19	RTK
	Bondi	875	SSE [154]	C2	H2	565	-123	824	22	175	155	35	25/11/15	30/7/19	RTK
	Tamarama	80	SE [130]	C3	H6	210	39	231	110	120	170	33	26/2/16	30/7/19	RTK
	Bronte	250	E-ESE [103]	C2	H6	199	53	325	200	75	130	33	26/2/16	30/7/19	RTK
	Coogee	460	E-ESE [112]	C3	H2	259	-102	670	339	147	146	26	13/6/16	30/7/19	RTK
	Maroubra	980	E [100]	C2	H6	665	560	987	350	65	131	34	11/2/16	30/7/19	RTK
	Malabar	180	SE [138]	C4	H6	1227	506	1487	252	121	143	10	23/5/18	30/7/19	RTK
South Coast	Moruya	2430	E [90]	C1	H5	529	283	470	0	45	90	32	24/11/15	14/6/18	Emery
	Pedro	2470	E [100]	C1	H3	375	23	900	-152	90	50	32	24/11/15	14/6/18	Emery

3.3 Methods

3.3.1 Hydrodynamics

We used offshore wave data for Sydney (SYD) and South Coast at Batemans Bay (BAT) from 01/11/2015–21/06/2019, corresponding to the beach survey period (Figure 3.1b–c). The SYD buoy is 10 km offshore in 90 m water depth, 10 km southeast from Narrabeen and 17 to 25 km northeast of the study beach zone from Bondi to Malabar (Figure 3.1b). The BAT buoy is 4 km offshore in 73 m water depth and 25 km northeast of the southern sites Moruya and Pedro (Figure 3.1c). Wave data included hourly offshore H_s, T_z, peak period (T_p) and θ_w measurements. Wave power (energy flux) P was calculated following Komar (1998),

$$P = EC_g \tag{3.2}$$

where, wave energy (E) is expressed as,

$$E = \frac{1}{16}\rho g H_s^2 \tag{3.3}$$

where, ρ is seawater density (1025 kg/m^3), g is the gravitational acceleration (9.81 m/s), and wave group velocity C_g (m/s) is expressed as,

$$C_g = \frac{gT_z}{2\pi}n \tag{3.4}$$

where, parameter n for deep water is 0.5 and T_z is wave period. A Peaks-Over-Threshold method described in Harley (2017) was used to identify storms (listed in Supplementary Table S1) with a wave height threshold of 3 m H_s and a minimum duration of 6 hours based on the NSW wave climate (Shand et al., 2010). There were 67 storms in total, and we focused on those where waves exceeded the 90^{th} percentile of cumulative storm power (P_{sum}) (sum of hourly P measures per storm), herein referred to as the "high-energy storms", cross-referenced and combined in one list of events from both regional buoys (SYD and BAT). We paid particular attention to the notable 4–7^{th} June 2016 storm, that was the most erosive storm in NSW for at least 40 years (Harley et al., 2017). This storm consisted of a relatively slow-moving weather system that impacted 2000 km of the east Australian coast, it coincided with superelevated springtide water-level of 0.44 m above the mean tide level, it had a storm surge of 0.34 m, an Average Recurrence Interval (ARI) of ~2.5 years and an atypically E-NE storm direction (Mortlock et al., 2017).

3.3.2 Headland impacts

We developed a simple trigonometric method using to quantify the proportions of an embayed beach that receive headland-modified waves (protected zone) such as due to refraction, and headland-unmodified waves (exposed zone) during various storm wave directions. This was based on two key properties of headland geometry (length and orientation) in conjunction with storm wave directions (Figure 3.2a–b). We used open-access satellite imagery from Google Earth Inc., and as such, submerged rocky reefs and platforms that are often hard to identify in these images, and the associated wave refraction processes, were not included in our analyses but are important because they underlie important wave processes such as refraction and diffraction (Hsu and Evans, 1989). Naming convention we use follows Short and Masselink (1999) and Fellowes et al. (2019) (Chapter 2). The distance alongshore of beach length (X_d) that is protected

and shadowed by headlands and the boundary between this protected zone and the exposed zone was defined as the shadow edge (X_{se}). This X_{se} was calculated for each storm and is based on storm wave direction and the headland geometries, due to this there may be different proportions of each zone from different wave directions (Figure 3.2c). A shadow headland is the headland that is actively shadowing the beach from storm wave direction (θ_w), defined by incident angle to the shore-normal beach aspect (beach's average aspect) and waves ($\alpha_w = \alpha_{eb} - \theta_w$). For example, an east-facing beach ($\alpha_{eb} = 90°$) has a southern shadow headland when $\theta_w > 90°$ and a north headland shadow when $\theta_w < 90°$ (e.g., Figure 3.2c and d). To quantify the location of the boundary X_{se} we used a trigonometry approach,

$$X_{se} = tan(\theta_w).X_{hl} \tag{3.5}$$

where, α_w is the incident angle (in this case mean storm wave direction) and X_{hl} is the cross-shore headland length (Table 3.1).

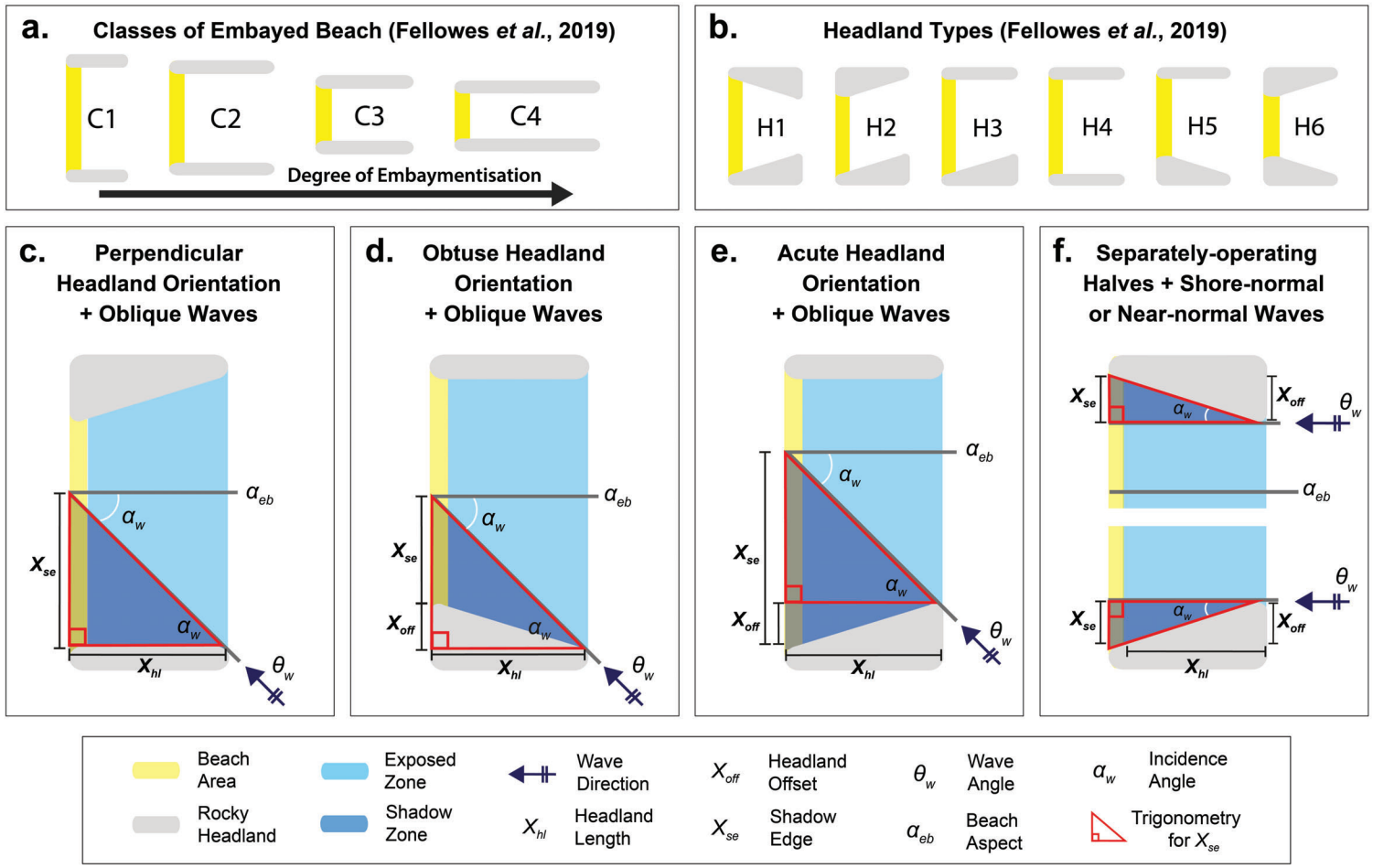

Figure 3.2: Methodology to quantify the shadow edge (X_{se}) (Eq. 4) for the (a) different classes of embayed beach (Class 1–Class 4) and the (b) headland types (H1–H6) stated in Fellowes et al, (2019) (Chapter 2). Methods for a (c) perpendicular headland orientation with oblique waves (H3–H6), (d) obtuse headland orientation with oblique waves (H5–H6), (e) acute headland orientation with oblique waves (H1–H3), and, (f) separately-operating beach halves with (quasi) shore-normal waves (H1–H3).

The offshore headland extent was used as the origin for the triangle, with a line perpendicular to α_{eb} extending to the back-beach boundary such as a sea wall, promenade or dune toe if no static boundary was present (Figure 3.2c–f). If the shadow headland orientation was obtuse relative to α_{eb} (typical of H4–H6), then a headland offset distance X_{off} was subtracted from X_{se} as the triangle drawn starts before the start of the beach and must be corrected to so that the distance only covers the shadow on the beach (Figure 3.2d). Conversely, if the headland orientation was acute relative to α_{eb} (typical of H1–H3), then a headland offset distance X_{off} was added to X_{se} to make up for the beach length that is not covered by X_{se} as the triangle starts away from the beach end (Figure 3.2e). The profile locations were then measured alongshore from the shadow headland relative to X_{se} with the exposed zone above ($X_{se} > 0$) and shadowed zone below ($X_{se} < 0$) this boundary. On occasions, both headlands can shadow both ends of the beach simultaneously, such as on H1 to H3 beaches when both headland orientations were acute relative to α_{eb} (H1) or when storm wave directions θ_w were close to α_{eb} (Figure 3.2f), in which case the beach was treated as two separately-operating halves, with an X_{se} calculated from each headland (Figure 3.2f). Furthermore, if $\theta_w \approx \alpha_{eb}$ then the headland orientation angle (e.g., if headland has acute orientation and shadows) is used as the wave angle to calculate X_{se} (Figure 3.2f). Then profile distances from X_{se} were normalised as a percentage of beach length X_d and used to categorise distances of shadowed and exposed profiles within the corresponding halves.

3.3.3 Beach profile surveys

We used beach survey data from November 2015 to July 2019 (Table 3.1). Cross-shore topographic profiles of the subaerial beach (Figure 3.1) were collected using a combination of RTK-GNSS (Real Time Kinematic Global Navigation Satellite System) and Emery surveys (Table 3.1). The profiles had origins at the back of the beach (sea wall or benchmark in dune) and extended perpendicular to the shoreline; they were measured at low tide and extended to wading depth (~ -0.5 m mean sea level, MSL). Cross-shore beach distances to MSL (dX) and subaerial (above MSL) profile volume V (m^3/m) were quantified, with deviations of ΔdX and ΔV at each profile normalised by the study averages (2015–2019), using similar methods to Harley et al. (2011b) and Burvingt et al. (2018). Percentage profile recovery after storms R,

was calculated following the method of Harley et al. (2017),

$$R = 100\ (\Delta V_{recovery}\ /\ \Delta V_{storm}) \tag{3.6}$$

where, $\Delta V_{recovery}$ is volume recovery and ΔV_{storm} is storm erosion. We reviewed existing embayed beach literature from other swell-dominated regions to compare with this study. The regions where chosen for available erosion and volume recovery data and their representation of the different classes of embayed beach (Class 1–Class 4), headland types (H1–H6) to individual storms or storm-clusters. These regions include data from the United Kingdom (UK), including 8 beaches in Cornwall (Perranporth, Sennen, Constantine, Fistral, Trenance, Porthtowen, Porth and Porthcothan) during the Boreal winter storm season in 2013/14, and at Perranporth for 4 winter storm seasons between 2009/10 and 2013/14 (Masselink et al., 2016a; Masselink et al., 2016b; Pitman et al., 2016; Scott et al., 2016b; Burvingt et al., 2017; Burvingt et al., 2018); Data were also used from 3 beaches in central Portugal (Monte Clérigo, Amoreira and Arrifana) during the Boreal winter storms of 2007/08 and 2008/09 (Loureiro et al., 2011; Loureiro et al., 2012a; Loureiro et al., 2014); and, 3 beaches (North Haven, Boomerang and Elizabeth) in NSW Australia (Harley et al., 2017) to the June 2016 storm that we pay particular attention to in this study.

3.4 Results

3.4.1 Hydrodynamics

During our survey period in southeast Australia, the wave conditions were representative of the long-term wave climate, with mean offshore H_s were 1.6 m at Sydney (SYD) and 1.4 m at South Coast (BAT) (Figure 3.3a–b), T_z were 6.2 and 6.1 s (Figure 3.3c–d), and mean θ_w was 135° and 130° at SYD and BAT respectively. Seasonal variation showed the usual trends defined by Harley et al. (2011b) of easterly waves in Austral summer and southerly waves during the winter (Figure 3.3e–f). Mean wave power P was 0.01 $x10^3$ and 0.008 $x10^3 Kw/m$ in SYD and BAT (Figure 3.3g–h).

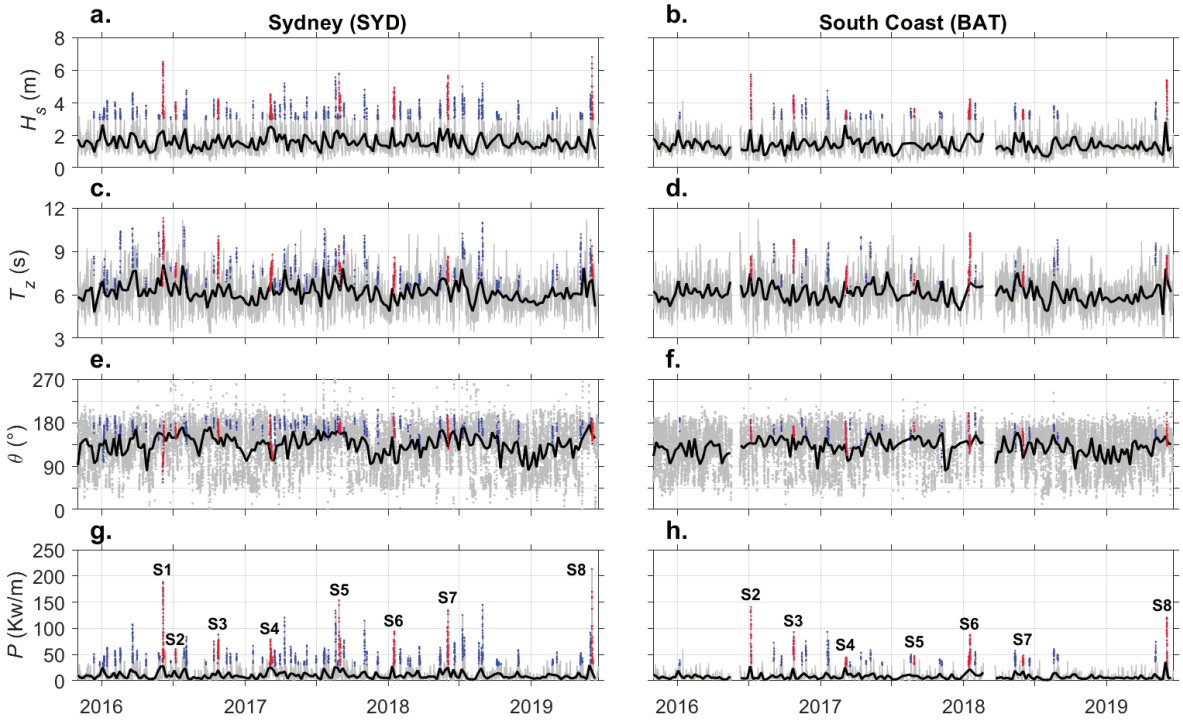

Figure 3.3: Regional offshore waves and P with hourly measurements (grey), 7-day average (black) and storms (H_s > 3 m for minimum 6-hour period in blue) with the high-energy storms for cumulative storm power P_{sum} from both regions (SYD and BAT) labelled in red (S1–S8). (left) Sydney (SYD) and (right) South Coast (BAT). (a–b) significant wave height H_s, (c–d) wave period T_z, (e–f) wave direction θ_w, and (g–h) wave power flux P.

There were more than double the number of storms (H_s >3 m) in SYD (n = 67) than in BAT (n = 27) (Figure 3.3a–b). Average storm statistics at SYD and BAT were similar, with mean storm H_s of 3.5 m and 3.4 m, T_z of 7.7s and 7.6 s, T_p of 10.9 s and 10.8 s and θ_w of 167° and 160° respectively. The same eight high-energy storms (S1–S8) were identified from both buoys (excl. S1 at BAT from instrument malfunction) (Figure 3.3d; Table 3.2). These storm waves had statistics that were largely similar, although some regional inconsistencies in P_{sum}, duration and wave directions occurred during S2 and S6 (Figure 3.3g–h; Table 3.2). Please note that S2 and S5 were included as high-energy storms in both regions even though they primarily impacted the South Coast only (Table 3.2). The beach responses to all 8 high-energy storms were therefore included for both regions for comparison.

Table 3.2: The high-energy storms for cumulative storm power P_{sum} when H_s > 3 m (S1–S8) from Sydney (SYD) and South Coast Batemans Bay (BAT) buoys.

Storm	**S1**		**S2**		**S3**		**S4**		**S5**		**S6**		**S7**		**S8**	
Dates SYD	4–7 Jun 2016		7-8 Jul 2016		22–25 Oct 2016		4–11 Mar 2017		28-Aug-01 Sep-17		14–17 Jan 2018		31 May – 3 Jun-18		4–7 Jun 2019	
Dates BAT	5–7 Jun 2016		6-8 Jul 2016		23–25 Oct 2016		5–8 Mar 2017		27-28 Aug 2017		13–18 Jan 2018		31 May – 3 Jun-18		4–5 Jun 2019	
Buoy	SYD	BAT	SYD	BAT	SYD	BAT	SYD	BAT	SYD	BAT	SYD	BAT	SYD	BAT	SYD	BAT
Duration (h)	75	-	47	37	66	43	168	66	100	9	82	124	69	59	70	36
Mean Hs (m)	4.2	-	3.5	4.3	3.7	3.8	3.5	3.2	4.2	3.4	3.7	3.4	4.2	3.3	4	4.6
Max Hmax (m)	12	-	7.2	11	8	9.4	8.6	7.2	10.4	7.9	9.6	7	10	7	12.5	10.2
Mean Tz (s)	9.1	-	7.6	7.8	8.7	8.7	7.4	7	8	7	7.3	8.2	7.6	7.2	7.8	8
Mean Tp (s)	14	-	11	10.9	12.3	12.5	11.2	10.1	11	10	10.6	11.2	11.5	11.5	11.1	11.3
Mean Wdir (°)	119	-	160	158	166	160	146	150	171	169	174	147	171	148	162	153
Mean Bearing	ESE	-	SSE	SSE	SSE	SSE	SE	SSE	S	S	S	SE	S	SSE	SSE	SSE
P_{sum} $x10^3$ **(Kw/m)**	6.35	-	1.49	2.74	3.04	2.72	3.89	2.14	2.63	0.39	2.74	3.28	4.24	1.38	2.77	3.06

3.4.1.1 Fair-weather and stormy periods

The study period was characterised by times of extended fair-weather conditions when MEI was positive (El Niño) and stormy-periods when MEI was negative (La Niña) (Figure 3.3g–h; Figure 3.4). During the fair-weather periods in the Austral summer of 2015–16 and from mid-2018 to mid-2019 (+MEI) no high-energy storms were recorded. The stormy-period from June 2016 to June 2018 (-MEI), saw the first 7 high-energy storms (S1–S7) occur with an average spacing of 131 days (~4 month) (Table 3.2). The final high-energy storm (S8) was in June 2019 and ended a year-long period of fair-weather conditions.

3.4.2 Exposure and headland impacts

3.4.2.1 Beach exposure to storm waves

The total subaerial beach volume loss (ΔV) to storms was dictated by beach aspect (α_{eb}), while within beaches was determined by the aspect (α_p) of the individual beach profiles in relation to storm wave direction (θ_w). The α_p commonly varied alongshore, with beach curvature making

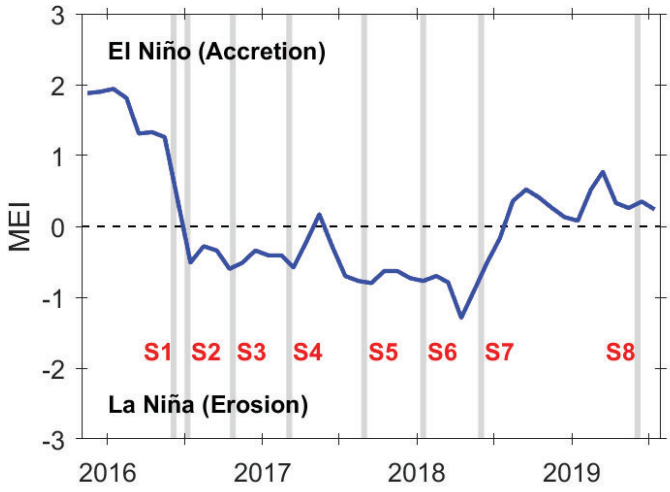

Figure 3.4: Multivariate El Niño Southern Oscillation Index (MEI) showing high-energy storms (S1–S8) (grey). Fair-weather periods (Austral summer 2015/16, June 2018–June 2019) during El Niño (warm, accretion, +MEI) and stormy period (June 2016–June 2018) during La Niña (cool, erosion, -MEI).

profiles near the headlands different to the central beach α_{eb} (e.g., Bondi P1 and P3; Figure 3.1e). Profiles that aligned with θ_w typically had higher ΔV than those orientated away from θ_w (Figure 3.5). In general terms, if θ_w was E-ENE, the central and southern profiles (P3–P5) with $60° > \alpha_p < 120°$ were more exposed on east-facing beaches like Maroubra and Narrabeen (Figure 3.1d and i; Figure 3.5a); while if θ_w was S-SE then the central and northern profiles (P1–P3) with $80° > \alpha_p < 140°$ were more exposed (Figure 3.5c). This was clearly seen during S1, which had a mean θ_w of 118° (E-ENE) and at profiles with α_p of 80–100° (E) ΔV reached 155 m^3/m (mean ~100 m^3/m) (Figure 3.5a), which was up to 3 times that of profiles that had α_p of >120° with ΔV reaching 80 m^3/m with a mean of ~50 m^3/m (Figure 3.5a). This same wave exposure and profile α_p relationship was also evident for SE storm waves, for instance during S4 with a θ_w of 148° (SE) profiles with α_p of 80–120° (E–SE) had double the ΔV, reaching 50m^3/m (mean ~30 m^3/m), compared to profiles at had α_p of <60° and >120° which reached 25 m^3/m (mean ~20 m^3/m) (Figure 3.5d). Storms that caused overall accretion occurred when the storm only impacted one region, for instance impacting the BAT buoy and the South Coast beaches of Moruya and Pedro to S2 and S5 while the Sydney beaches were not impacted and showed volume increases (Figure 3.5b and e).

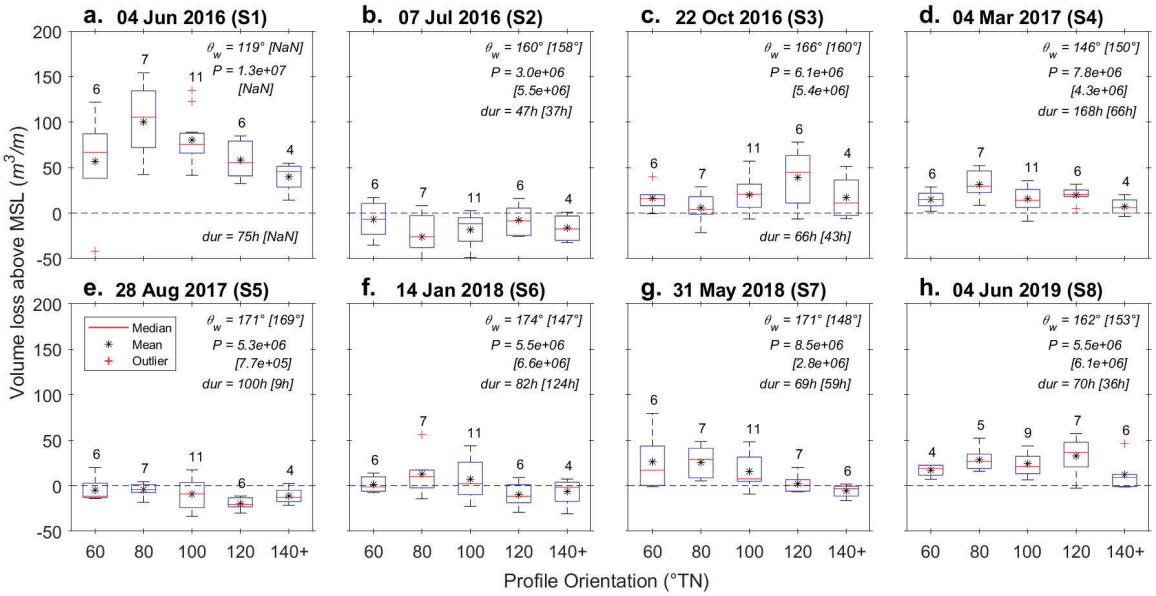

Figure 3.5: Profile orientation and beach volume loss above MSL (m^3/m). High energy storms (a–h) with mean direction (θ_w), cumulative power (P_{sum}) and duration for SYD [BAT]. Orientations are separated by 20-degree bins and have n profiles stated above each boxplot.

3.4.2.2 Headland shadowing (X_{se})

In addition to the beach and profile aspects (α_{eb} and α_p) and exposure to storm waves (Figure 3.5), headlands also played an important role in alongshore variability in beach response to storms. Alongshore wave energy gradients due to headland shadowing, defined using our method of quantifying the shadow edge (X_{se}), highlighted the difference in morphodynamic response in the exposed and protected zones (Figure 3.6a). There was a significant positive relationship between the distance from X_{se} and subaerial beach volume loss (ΔV) (Figure 3.6a), whereby if a profile was in the shadow zone (X_{se} < 0) it either had a reduced ΔV than those in the exposed zone (X_{se} > 0) or even accretes as a result of the storm as seen in S8 (Figure 3.6a). Meanwhile, individual storms gave the highest ΔV when they were shore-normal to the beaches when X_{se} = 0–100 (Figure 3.6b; Figure 3.7). The ΔV was 7 times less for profiles in the shadow zone compared to the exposed zone. The mean ΔV for profiles in the shadow zone was -6 m^3/m and (σ±7 m^3/m) and for profiles located in the exposed zone had a mean ΔV = -43 m^3/m (σ ± 25 m^3/m) (Figure 3.6a). Comparing the shadow edge (X_{se}) and the classes of embayed beaches showed increasing relationship from the protected zone to the exposed zone with volumes losses

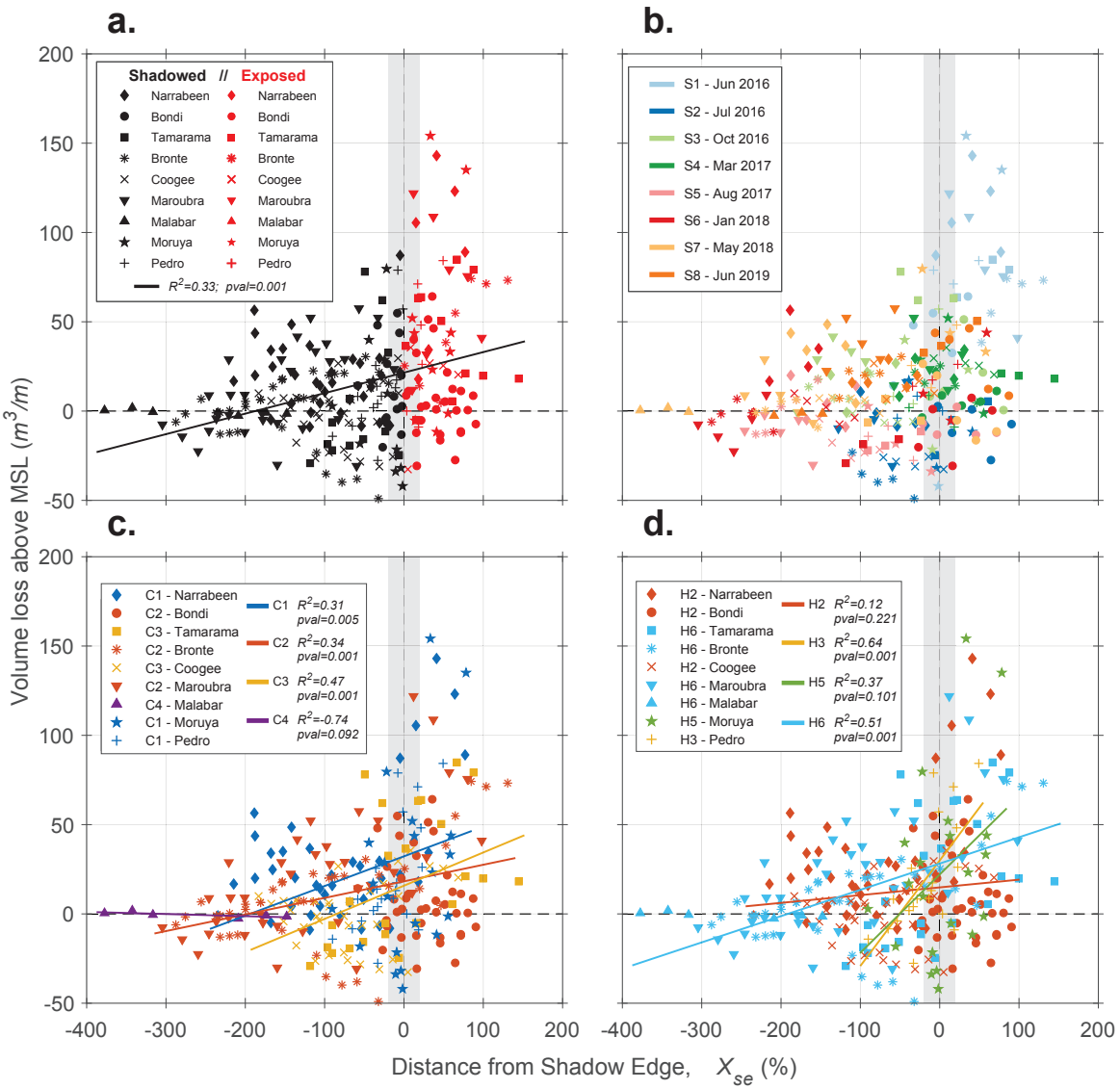

Figure 3.6: Subaerial volume loss ΔV (m^3/m) and distance from the shadow edge X_{se} (vertical grey band $\sim X_{se} = 0$) as a % of beach length (X_d) to the eight high-energy storms. (a) ΔV in shadow zone when $X_{se} < 0$ (black) and exposed zone (red) when $X_{se} > 0$ with trendline, (b) storms (S1–S8) and X_{se}, (c) classes (Class 1–Class 4) and X_{se} with trendlines, and (d) headland types and X_{se} with trendlines.

to storms ΔV for Class 1 to Class 3, but for Class 4 this was a negative relationship (Figure 3.6c). The presence of submerged rocky reefs and the offshore islands that were not accounted for by X_{se} and meant that Bondi (Class 2), Coogee (Class 3) and Moruya (Class 1) did not have a clear X_{se} and ΔV relationship, and ΔV was commonly the same in the exposed and protected zones (Figure 3.6a–b). While X_{se} and headland types showed mixed results in the relationship with ΔV so that the positive relationship was significant for H2 and H6 and not for H3 and H5

(Figure 3.6d).

3.4.2.3 Storm response

The greatest mean absolute volume change $|\Delta V|$ (i.e., any change in V, either accretion or erosion) to the high-energy storms was greatest in lower class beaches, with mean changes of 18.9 % for Class 1 and Class 2 beaches and 8.4 % for Class 3 and Class 4 beaches (Figure 3.6b). Focusing just on beaches that eroded overall during storms, the highest erosion generally occurred in the least embayed classes (Class 1 and Class 2; e.g., Narrabeen, Moruya and Pedro to S1, S6–S8) (Figure 3.7). The beach aspect to storm wave direction also had a strong influence on the degree of erosion. The eight high-energy storm waves came from three main directions (E-ENE, SE and S) (Table 3.1):

E-NE storm waves (S1): the E-ENE waves of the June 2016 (S1) impacted the east-facing beaches more than the S-SE facing beaches. For example, Maroubra is east-facing, and thus exposed to E-NE waves and had a mean ΔV of -90 m^3/m compared to Bondi which faces S-SE facing so less exposed to these waves which had ΔV of -45 m^3/m (Figure 3.1e and i; Figure 3.7). Furthermore, this storm had the greatest ΔV, because many of the normally headland protected beach profiles were exposed to waves from the direction, such as (P5) at the south ends of Narrabeen, Bronte, Coogee, Maroubra, Pedro (Figure 3.6b; Figure 3.7a, d–f, i).

SE-SSE storm waves (S2, S3 S4, and S8): for SE waves, most beaches were exposed and eroded during the storms (e.g., S4 mean -20 m^3/m across all sites), with the exception of the protected south ends of the east-facing beaches which have prominent southern headlands in the shadow zone (e.g., Narrabeen and Maroubra; Figure 3.6b; Figure 3.8a and g).

S storm waves (S5, S6 and S7): For southerly waves, most beaches did not experience high ΔV as all profiles were typically in the shadow zone (when $X_{se} < 0$). The exception to this were the Class 1 beaches that were still exposed at the mid-beach to S waves (i.e., were too wide to have headland protection along the whole beach) and had ΔV = -15-25 m^3/m (e.g., S6; Figure 3.6c; Figure 3.7; Figure 3.8a, h–i).

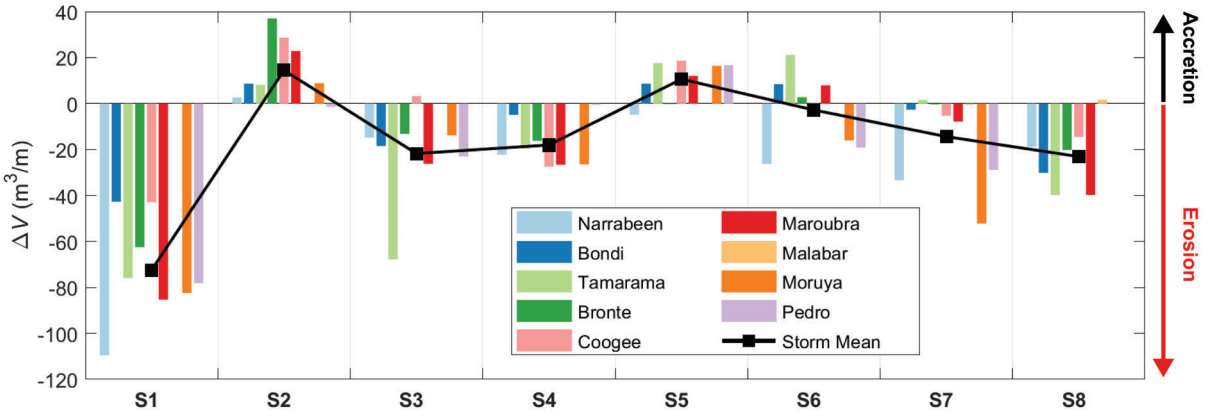

Figure 3.7: Subaerial beach volume change (ΔV) from the high-energy storms (S1–S8). Note that S2 and S5 were included for comparison but only impacted the South Coast beaches.

Timeseries of ΔV and ΔdX showed that beaches typically experienced erosion from the high-energy storms (Figure 3.4; Figure 3.8). The stormy-period (-MEI, Figure 3.4) from mid-2016 to mid-2018 was the most active, with the largest change in ΔV and ΔdX (Figure 3.3; Figure 3.8). Moreover, the least embayed beaches (Class 1–Class 2) had largest variations in ΔV (Narrabeen (Class 1) 160 m^3/m, Maroubra (Class 2) 120 m^3/m and Moruya (Class 1) 150 m^3/m; Figure 3.8a, h–i; Figure 3.9a). On the contrary, the most embayed beaches (Class 3–Class 4) and those controlled by rocky reefs and platforms in addition to the headlands (e.g., Coogee; Figure 3.8e) showed small ΔV and ΔdX (Coogee (Class 3) 60 m^3/m and Malabar (Class 4) 5 m^3/m; Figure 3.8e and g; Figure 3.9a). Mean ΔV decreased from Class 1 to Class 4, at -25 m^3/m for Class 1, -12 m^3/m for Class 2, -7 m^3/m for Class 3 and -0.5m^3/m for Class 4 (Figure 3.9a). Looking at the mean absolute change in $|\Delta V|$ to the 11 high-energy storms, there was a decreasing percentage change from Class 1 with 14.8 ±17.3 %, to Class 2 with 17.5 ±20.5 %, to Class 3 with 15.2 ±17.0 % and Class 4 with 1.5 ±1.6 %. Mean ΔV was not linearly related to headland type, with -12.5 m^3/m for H2, -19 m^3/m for H3, -24 m^3/m for H5 and -12 m^3/m for H6 (Figure 3.9b).

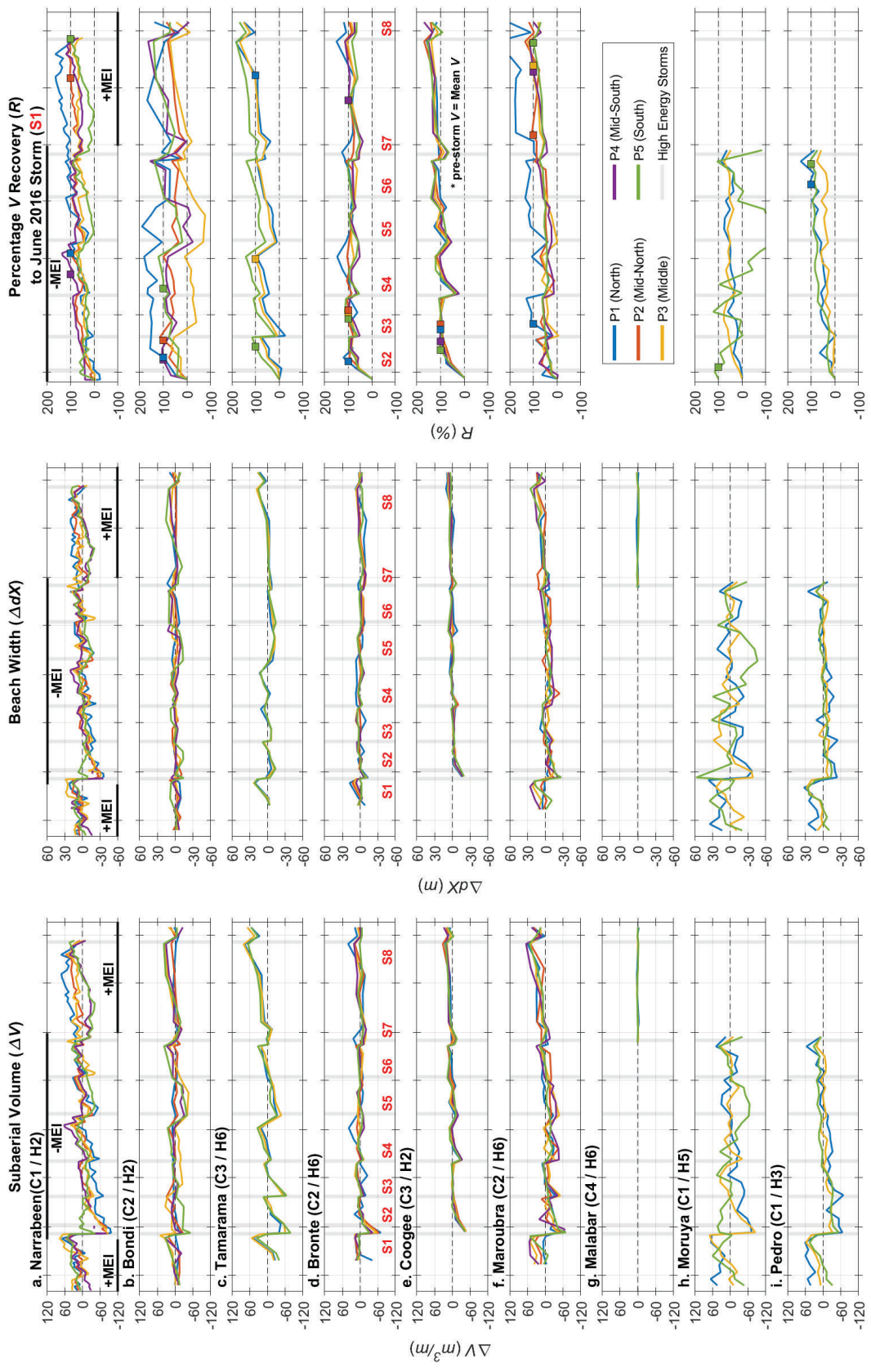

Figure 3.8: Timeseries of ΔV (m^3/m) (left), ΔdX (m) (middle) and beach volume recovery R (%) to June 2016 (S1) storm (right), where pre-storm volume is 100 % and storm volume lost is 0 % (dash line). (a) Narrabeen, (b) Bondi, (c) Tamarama, (d) Bronte, (e) Coogee, (f) Maroubra, (g) Malabar (no S1 recovery data), (h) Moruya, and (i) Pedro. High energy storms (grey lines) labelled S1–S8 (red) and fair-weather (+MEI) and stormy-periods (-MEI) (black lines).

3.4.2.4 Fair-weather response

The beaches recovered subaerial volume and beach width in the periods between the high-energy storms (e.g., post-S1 to pre-S3) and during the longer fair-weather periods (mid-2018–mid-2019) when MEI was positive (Figure 3.4; Figure 3.8). During these calmer conditions all beaches across the 4 classes were in an accreted state with both ΔV and ΔdX above the study (2015–2019) averages (Figure 3.8). During the Austral summer 2015–16, at Narrabeen (Class 1) and Maroubra (Class 2), the mean change in V was +60 m^3/m (38 and 46 %) and ΔdX was +25 m above the study-average (41 and 40 %) (Figure 3.8a and f). At Bondi (Class 2) and Tamarama (Class 3), ΔV was +50 m^3/m (28 and 16 %) and ΔdX was +15 m (19 and 15 %) (Figure 3.8b and c), Bronte (Class 2) ΔV was +20 m^3/m (20ΔdX) and ΔdX +15 m (32ΔdX) (Figure 3.8d) and at Moruya (Class 1) and Pedro (Class 1) ΔV was +65 m^3/m (29 and 40 ΔdX) ΔdX and +40 m (38 and 53 %) (Figure 3.8h–i). In May 2016 (pre-S1), all the beaches increased ΔV and ΔdX further up to maxima of ΔV up to 70 m^3/m and ΔdX up to 40 m (Figure 3.8). The longest fair-weather period was from mid-2018 to mid-2019 when ΔV and ΔdX increased across all classes, with all sites recovered back to pre-June 2016 (S1) storm levels. The exceptions were Moruya and Pedro where this could not be verified because data collection finished in June 2018, but results indicate that their recovery was following the same trend and that by now 2019 they would have recovered (Figure 3.8h–i). In the fair-weather period (+MEI) between mid-2018 to mid-2019, ΔV and dX steadily increased (Figure 3.8). The mean change in V changed during this time was +90 m^3/m for Class 1 (Narrabeen, Moruya and Pedro), +60 m^3/m for Class 2 (Bondi, Bronte and Maroubra), +50 m^3/m for Class 3 (Tamarama and Coogee) and +0.5 m^3/m for Class 4 (Malabar). At the same time the mean ΔdX per class was +30 m for Class 1, +16 m Class 2, +12.5 m for Class 3 and +0.5 m for Class 4 (Figure 3.8).

The subaerial beach recovery rate during the fair-weather periods and after these high-energy storms varied across the 9 embayed beaches (Figure 3.9c). There was a nonlinear trend in recovery rates with increasing embayed beach classes, where we see this inconsistency with a rate of 0.31 $m^3/m/day$ for Class 1, 0.16 $m^3/m/day$ for Class 2, 0.28 $m^3/m/day$ for Class 3 and 0.011 $m^3/m/day$ for Class 4 (Figure 3.9c). Furthermore, an assessment of the different headland

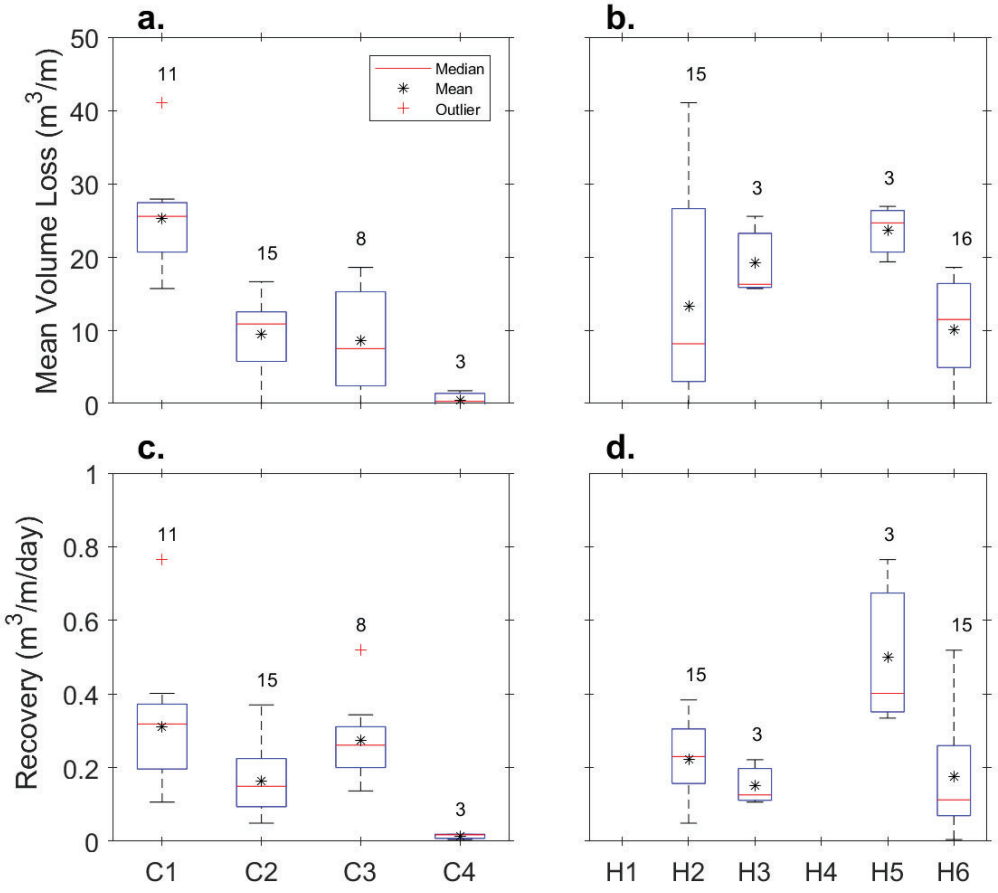

Figure 3.9: Mean storm volume loss (m^3/m) to high-energy storms for (a) class of embayment and (b) headland type, and rate of recovery ($m^3/m/day$) for (c) class of embayment and (d) headland types with n profiles in each category.

types showed that the recovery rates were different for the 4 types of headlands represented in this study (Figure 3.9d). Recovery rates were highest for the H5 (Figure 3.2b) which recovered ~2-3 times faster than the other headland types was 0.5 $m^3/m/day$, compared with mean recovery rates of H2 at 0.22 $m^3/m/day$, for H3 was 0.15 $m^3/m/day$ and H6 was 0.18 $m^3/m/day$ (Figure 3.9d).

3.4.3 Case Study: June 2016 storm (S1) erosion and recovery

The June 2016 (S1) storm impacted all beaches in this study (Figure 3.7). The overall mean ΔV was -73 m^3/m, ranging from 43 m^3/m (19 % of subaerial volume) at Bondi to 155 m^3/m (51 %) at Narrabeen (Figure 3.7). Contrary to the general erosional trend observed during S1,

Moruya (P5) had the only profile that accreted post-storm with an increase to ΔV of +50 m^3/m (+20 % of subaerial volume) (Figure 3.7). This compares to the other Moruya profiles (P1 and P3) that experienced losses to ΔV of -135 and -154 m^3/m (33 and 35 % of subaerial volume) respectively (Figure 3.8h). Overall losses in terms of percentage change were highest for the less embayed beaches with volume losses at Tamarama (Class 3, Figure 3.1f) of ΔV = 76 m^3/m or 22 % of beach volume and at Narrabeen (Class 1, Figure 3.1d) with losses of ΔV = 110 m^3/m or 50 % of beach volume (Figure 3.8a).

The length of time beaches took to recover 100 % of their subaerial volume after the June 2016 storm (S1) varied between classes and headland types (Figure 3.8). Please note this section refers to profiles that are number from north to south (Figure 3.1). The overall mean profile recovery rate after S1 was 0.24 ±0.11 $m^3/m/day$, ranging from 0.05 $m^3/m/day$ at Bondi (P3) to 1.2 $m^3/m/day$ at Bronte (P1) (Figure 3.9c–d). Higher class beaches (Class 3) had faster recovery rates than lower classes (Class 1 and 2). Note that no data was recorded for this storm at Class 4 Malabar. The mean recovery rate after S1 for Class 1 (Narrabeen, Moruya and Pedro) was 0.15 ±0.03 $m^3/m/day$, for Class 2 (Bondi, Bronte and Maroubra) was 0.28 ±0.15 $m^3/m/day$ and Class 3 (Tamarama and Coogee) was 0.32 ±0.01 $m^3/m/day$ (Figure 3.9c; Figure 3.8). Note that recovery rates for Moruya and Pedro were calculated using data up to June 2018 when surveys finished. Class 3 beach Coogee recovered the fastest in 6 months (Figure 3.8e). The other Class 3 beach Tamarama was close to full recovery (P5 only) in 4.5 months after S1 (P1 and P3 had only recovered by 74 % and 81 % at this time), although the beach was similarly impacted by the (S3) storm with ΔV losses across all profiles comparable to S1 (mean -68 m^3/m, 20 % subaerial beach volume loss). Recovery after S3 was ~9 mouths and the recovery to 100 % pre-S1 subaerial volumes took 13 months (P3) and 33 months (P1) (Figure 3.1f; Figure 3.8c). For the Class 1 beaches, Narrabeen recovered to 100 % pre-storm volumes (exc. P3, max 91 % by June 2019) and took on average 23 months (Figure 3.8a). Moruya (Class 1) did not fully recover by June 2018 (P1 and P2, max 89 % and 77 %) although P3 accreted post-S1 (Figure 3.8g). Pedro (Class 1) recovered to 100 % pre-S1 subaerial volumes in an average time of 22 months (exc. P2, max 76 %) by the time surveys finished in June 2018 (Figure 3.8h). The Class

2 beach Maroubra took an average of 26 months across the 5 profiles to recovery to 100 % pre-S1 subaerial volumes (Figure 3.8f). Bronte (Class 2) took an average of 10.5 months across the 5 profiles to recovery to 100 % pre-S1 subaerial volumes (Figure 3.8d); while, Bondi (Class 2) the least impacted by the S1 storm recovered (exc. P3, max 72 %) in 4.5 months (Figure 3.8b). Notably, the profiles that did not recover to 100 % pre-storm were typically at the middle-beach away from the headlands (e.g., Narrabeen, Bondi; Figure 3.8a–b). Recovery rates to S1 also varied with headland type, was 0.27 ±0.08 $m^3/m/day$ for H2, was 0.12 $m^3/m/day$ (n = 1, no standard deviation,) for H3, was 0.15 $m^3/m/day$ (n = 1, no σ) for H5, and was 0.29 ±0.15 $m^3/m/day$ for H6 (Figure 3.9d) (there were no H1 or H4 headland types).

3.5 Discussion

3.5.1 Shadow edge (X_{se}) morphodynamics

In this paper, we present a simple trigonometry-based approach for quantifying the zones of embayed beaches (X_{se}) that are protected (by wave shadowing) and exposed (not headland shadowed) (Figure 3.2c–f). During high-energy storms, exposed zones may experience 7 times more subaerial volume loss (ΔV) than protected zones (Figure 3.6a). This is largely due to wave shadowing in the zone in the lee of headland that receives largely refracted waves (Daly et al., 2014; McCarroll et al., 2014; Castelle et al., 2016) and creates an alongshore gradient of beach morphodynamics (Harley et al., 2015). Wave refraction around headlands is not linear (Masselink et al., 2014), and our X_{se} method is a simplistic approach that uses open-access imagery to characterise headland geometries combined with storm wave direction and can be applied to any embayed beach with minimal effort (Figure 3.2c–f). Shadow edge (X_{se}) shows a significant increasing subaerial volume loss (ΔV) trend with less headland shadowing and greater wave exposure (Figure 3.6a). Our research identifies beaches (and classes of beaches) that are more susceptible to storm impacts because of their inherent headland orientations and their shadowing processes, including identifying those cases where due to headland configuration, there is shadowing with shore-normal waves or the configuration is such that there are two

shadowed zones (Figure 3.2f).

The high-energy storms in this study had three main wave directions (ENE, SE–SSE and S) (Figure 3.3; Table 3.2), that caused different X_{se} locations alongshore and hence varied the morphodynamic response (Figure 3.6b). Our results show that headland shadowing is typically greater with oblique storm waves (Figure 3.6b); for example, the X_{se} was smaller during the quasi shore-normal waves of S1 (E-ENE) than with the oblique waves of S8 (SSE) (Figure 3.6b; Table 3.1). We further show that certain headland orientations (e.g., H3–H6; Figure 3.2b) can shadow the beach even more when exposed to these oblique waves (Fellowes et al., 2019). For example, at Bondi (e.g., to S3; Figure 3.6b) where the beach aspect is oblique to the regional coastal orientation and dominant wave directions (Figure 3.1e), a large proportion of the beach is shadowed. Our method contributes to understanding alongshore morphodynamics on embayed beaches, accounting for both headland impact and degree of embaymentisation.

3.5.2 Embayment class, exposure and storm response

The response of the embayed beaches in this study to high-energy storms are dependent not just on the storms (relating to the MEI phases), but also the embayment settings and degree of embaymentisation (Figure 3.3; Figure 3.4; Figure 3.9a). The percentage and absolute volume losses ΔV to storms were the greatest at the least embayed beaches (Class 1 and Class 2) which are typified by wide embayments, shallow coastal indentations and relatively long beach lengths (over 750 m). Exposure to unmodified waves at these beaches shows a mean absolute volume change $|\Delta V|$ (i.e., accretion or erosions change) after high-energy storms was 18.9 % (Figure 3.9a). The highly embayed beaches (Class 3–Class 4) in NSW, that have narrow embayments, deep coastal indentation and strong headland influences, have a mean $|\Delta V|$ to the high-energy storms of 8.4 % (Figure 3.9a). On the contrary, when we consider all beaches in the different regions of the world (this study and literature, n = 22) the subaerial beach volume losses show an increasing mean ΔV as the degree of embaymentisation (towards Class 4 beaches) becomes more influential on beach morphodynamics with regional and site-specific trends in response (Figure 3.10a; Table 3.3; Supplementary Figure S1-S2). The mean subaerial beach volume

losses combined from this study and the data in the literature (Table 3.3) increases and become more variable with the degree of embaymentisation, with Class 1 beaches having ΔV= -43.2 ±55.0 m^3/m, Class 2 beaches having ΔV= -42.6 ±79.6 m^3/m, Class 3 beaches having ΔV= -40.4 ±94.1 m^3/m and Class 4 beaches having ΔV = -110 ±159.0 m^3/m (Figure 3.10a). This variability represents changes with the narrowing of embayments and with greater wave modification by headlands (towards Class 4 beaches), which Short and Masselink (1999) show are quick to shift between morphodynamic states (e.g., in this study the Class 3 beaches of Tamarama and Coogee; Figure 3.9a). At Malabar (Class 4) for example, there is near complete wave dissipation at the shoreline which we show from minimal ΔdX and ΔV throughout this study period (Figure 3.8g; Figure 3.9a). Comparing with Class 4 beaches in Cornwall (e.g., Porthcothan; Table 3.3), the response is greater than at Malabar (Figure 3.9a; Figure 3.10a; Table 3.3). We suggest this response is due to the number of events in the Boreal Winter 2013-2014 storm-season (n = 22) in addition to the macrotidal conditions in Cornwall (compared to microtidal at Malabar) that allow more wave energy up to the shoreface. For the Class 4 beaches in Cornwall, the narrow headland widths could generate wave turbulence or reflection, exaggerating sediment redistribution in the embayment and amplifying the storm impacts (Silvester et al., 1980). Meanwhile, in southeast Australia the ΔV and ΔdX trends are greater at the mid-beach (P3) where alongshore transport redistributes sediments within the embayment or could be from beach 'breathing', recently defined by Blossier et al. (2017) as shoreline oscillation that impacts alongshore morphodynamics. Headland adjacent profiles have higher ΔV in the exposed zone, which has been show by Castelle et al. (2016) to be the result of wave deflection processes and greater rip current activity in headland adjacent areas, evident at Bondi P5 and Maroubra P1 (Figure 3.8b and f).

The greatest losses of subaerial beach volume (ΔV) are at beaches that had aspects (α_{eb}) that align and expose them to storm wave directions, with embayed beach class or headland type being secondary (Table 3.1; Table 3.3; Supplementary Figure S1-S2). The S1 storm was the most erosive storm in this study and recent decades in southeast Australia and this is evident at Boomerang which was protected to S1 with an oblique aspect (SE) to this storm (E-ENE)

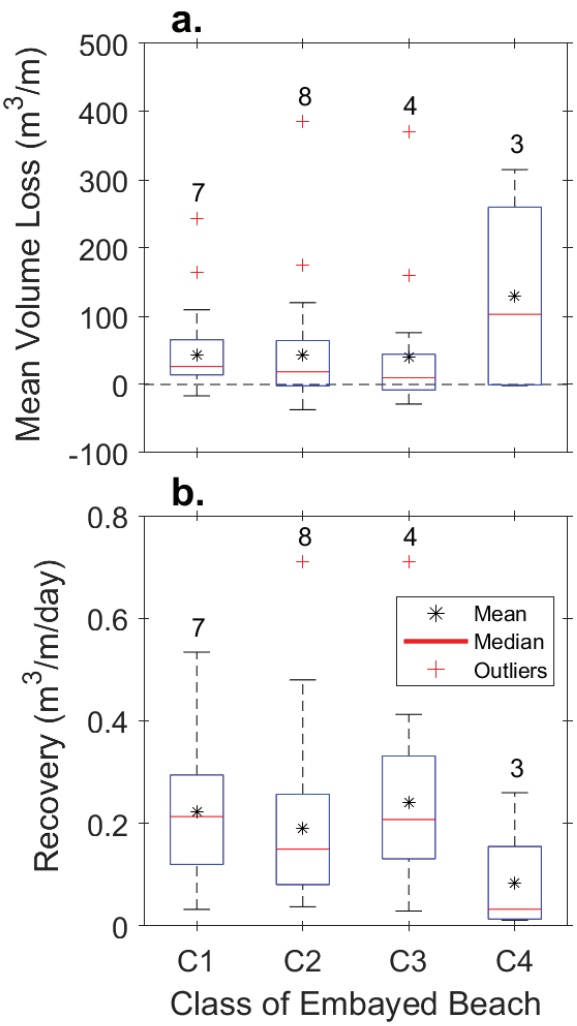

Figure 3.10: Boxplots of the combined beach data from this study and the literature (n = 22) with data from Table 3.3 and regional boxplots in Supplementary Figure S1-S2. (a) Subaerial volume loss (m^3/m) for the 4 classes and by (b) headland type. Note, the number of beaches is stated above each boxplot.

having higher than expected losses (mean -ΔV = 98 m^3/m) (Harley et al. (2017). Harley et al. (2017) also show how exposure impacts recovery to S1 at Elizabeth (0.26 $m^3/m/day$) which is modally protected to typical SE waves but was exposed to the June 2016 (S1) storm (Table 3.1), having a slower recovery than Boomerang ($0.44 m^3/m/day$) with exposure to fair-weather conditions. This reduction in recovery occurs at sheltered beaches in the mouth of estuaries exposed to storms but have α_{eb} that do not receive fair-weather swells necessary for subaerial beach recovery (Vila-Concejo et al., 2019). In Cornwall this is evident during the 2013/14 Boreal winter storm season (mean θ_w = W–WNW) with an ARI of 1:50 years, H_s reaching

over 10 m and was one of the most erosive storm seasons for 50 years that caused considerable damage to coastal infrastructure across SW England and Wales (Masselink et al., 2016b; Scott et al., 2016a). Different exposures and responses exist between Fistral (α_{eb} = NW) with losses of ΔV = -120 m^3/m which is less than the more storm exposed Constantine (α_{eb} = W) with losses of ΔV = -385 m^3/m (Table 3.3). A similar trend in Portugal to the Boreal winter 2008/09 storm season (storm α_w = N-NW) between the partially sheltered aspect at Arrifana (α_{eb} = WSW) with losses of ΔV = -115 m^3/m and the exposed Amoreira (α_{eb} = WNW) with losses of ΔV = -175 m^3/m (Table 3.3). Finally, in NSW to the June 2016 (S1, α_w = E-ENE) between the exposed Elizabeth (α_{eb} = NE) with losses of ΔV = -104 m^3/m and the partially oblique aspect of North Haven (α_{eb} = E) with losses of ΔV = -88 m^3/m (Table 3.3).

Subaerial beach volume recovery (R) in this study varies with embayed beach class (Figure 3.9c). Beach recovery is controlled largely by the exposure to typical fair-weather swells that transport sediments back to the subaerial beach (Morton et al., 1994), and at embayed beaches this recovery is further controlled by headland process and wave refraction (Loureiro et al., 2009). In southeast Australia, recovery is slowest at the least embayed beach classes (i.e., Class 1 and Class 2), for example, Coogee a higher embayed beach (Figure 3.1h) recovered to S1 after 6 months compared with Narrabeen which took up to 3 years (Figure 3.8a and e; Figure 3.9c).

For the classes of embayed beach, the combined dataset (n = 22) shows similarities in the volume recovery rates, independent of regional or storm characteristics (Figure 3.10b). The mean R rates for Class 1 beaches are 0.22 ±0.12 $m^3/m/day$, for Class 2 beach are 0.19 ±0.16 $m^3/m/day$, for Class 3 beach are 0.24 ±0.17 $m^3/m/day$ and then there was a considerable drop for Class 4 beach at 0.08 ±0.12 $m^3/m/day$ (Figure 3.10b; Supplementary Figure S1). Looking in more detail, mean R rates from the least embayed beaches (Class 1 to Class 3; n=19) are 0.22 $m^3/m/day$ and for Class 4 (n = 3) are 0.08 $m^3/m/day$ (Figure 10b). Short (2010) and Castelle and Coco (2012) show that headland refraction reduces energy when headland spacing is narrow (e.g., Class 4 beaches like Malabar in NSW or Porth in Cornwall). While Hegge et al. (1996) identify that for narrow embayments (Class 4) the small incident wave energy can cause slower recovery rates than at wider embayments (Class 1 to Class 3 beaches). If headlands extend far

Table 3.3: Mean erosion and recovery data collected from the literature. Embayed beach class and headland types quantified using the methods of Fellowes et al. (2019), volume loss ΔV, Recovery (R), R rate in $m^3/m/day$ and %, and R time in months at full recovery or last available measurement in literature. Note, DJF is Boreal winter (December, January and February).

Region	Site	Storm/ Storm-season	Storm Aspect θ_w	Beach aspect θ_{eb}	Class	HL Type	ΔV (m^3/m)	R (m^3/m)	$Rrate$ (m^3/m) /day)	$Rrate$ (%)	R time (months)	Literature
NSW, Australia	North Haven	June 2016 (S1)	E-ENE	E	C1	H2	-88	42	0.22	48	6	Harley et al. (2017)
	Boomerang			SE	C1	H2	-98	63	0.44	64	6	
	Elizabeth			NE	C2	H5	-104	41	0.26	39	6	
Portugal	Monte Clérigo	DJF 2007/08	N-NW	NW	C1	H5	-70	70	0.21	100	11	Loureiro et al. (2011); Loureiro et al. (2012a); Loureiro et al. (2014)
	Amoreira			WNW	C2	H4	-65	65	0.17	100	12	
	Arrifana			WSW	C2	H6	-66	60	0.24	90	8	
	Monte Clérigo	DJF 2008/09	N-NW	NW	C1	H5	-165	17	0.07	10	8	
	Amoreira			WNW	C2	H4	-175	53	0.22	30	8	
	Arrifana			WSW	C2	H6	-115	115	0.48	100	8	
	Perranporth	DJF 2009/10	WNWÐSW	W-NW	C1	H6	-37	37	0.12	100	10	Masselink et al. (2016a)
		DJF 2011/12					-41	41	0.12	100	13	
		DJF 2012/13					-50	39	0.12	78	11	
Cornwall, UK	Perranporth	DJF 2013/14	WNWÐSW	WNW	C1	H6	-243	121	0.3	50	12	Masselink et al. (2016a); Masselink et al. (2016b); Scott et al. (2016b); Burvingt et al. (2017); Burvingt et al. (2018)
	Sennen			WNW	C1	H6	-90	50	0.4	56	42	
	Constantine			W	C2	H5	-385	125	0.11	32	39	
	Fistral			NW	C2	H6	-120	120	0.15	32	21	
	Trenance			WNW	C3	H5	-370	250	0.4	100	21	
	Porthtowen			NW	C3	H6	-160	160	0.22	68	39	
	Porth			W	C4	H5	-315	190	0.26	100	24	
	Porthcothan			NW	C4	H6	-205	25	0.05	60	12	

offshore of the surf zone (as they did for the 9 beaches in this study), then during storms the embayments are closed littoral cells as per the definition in Short and Masselink (1999). When storms cause offshore sediment transport beyond the fair-weather depth of closure, the potential for sediment transport back onto the subaerial beach reduces greatly. As fair-weather waves are larger in Class 1-Class 2 beaches than they are in Class 3-Class 4, the potential beach recovery for highly embayed beaches is small. This is evident at Malabar (Class 4) and Porth (Class 4) that have similar embayment geometries and slow recovery rates of $0.05\ m^3/m/day$; Figure 3.1j; Figure Figure 3.9c; Figure 3.3). We suggest that this reduction in wave-energy from the deep indentation of Class 4 beach embayments creates a recovery rate threshold that highlights the complete embayment-control for these highly embayed beaches, making these beaches the most vulnerable to storms if they do experience erosion and their very low recovery rates from subsequent storms.

3.6 Conclusion

In this paper, we present a trigonometry-based approach to define the boundary between the exposed and protected (headland shadowed) zones of embayed beaches defined as the shadow edge (X_{se}). The X_{se} moves with storm wave direction, and to quantify the effect of this on embayed beach morphodynamics we focus on the storm response of 9 embayed beaches in southeast Australia to 8 high-energy storms from three main storm directions (E-NE, SE-SSE and S). The mean subaerial beach volume losses are on average 7 times higher (mean 43 m^3/m) in exposed zones compared to protected zones (mean -6 m^3/m). At the 9 beaches in southeast Australia, a case study surrounding the most erosive storm in this study (June 2016) shows beaches had mean ΔV of -73 m^3/m, with the lower classes of embayed beaches (Class 1 and Class 2) taking up to 3 years to recover while the higher classes of embayed beaches (Class 3) recovered in 6–12 months. Furthermore, combining data of storm response and recovery trends from 13 beaches from the literature (from elsewhere in NSW Australia, the United Kingdom and Portugal) show that embayed beach storm response varies with the embayment setting (geometries) and degree of embayment (level of control on morphodynamics). We show that beach exposure to fair-weather waves and the depth indentation of the embayment are the main determining factors in the rate of embayed beach recovery. Subaerial beach volume recovery (R) in this study is variable between the different classes of embayed beach, depending on the degree of embaymentisation, headland orientations and headlands shadowing processes. Mean beach recovery rates from this study and the literature for embayed beaches with low-moderate embayment control (Class 1–Class 3; n = 19) are consistent independent of region and storm characterises at 0.22 $m^3/m/day$; while, for embayed beaches with complete embayment control (Class 4; n = 3) the mean rate is 0.08 $m^3/m/day$. We propose that there is an embaymentisation threshold that indicates that more embayed beaches (Class 4) are potentially the most vulnerable to storms, are the slowest to recover and that protected and shadow zone morphodynamics are reason from multiple beach states alongshore.

3.7 Acknowledgements

Macquarie University Research Training Program funded TEF, the Re-Entry Fellowship from Women in Science at the University of Sydney funded AV-C. Thanks to Geocoastal Research Group with fieldwork assistance. Wave data is from Manly Hydraulics Laboratory (NSW Dept of Planning, Industry and Environment). The multivariate ENSO index (MEI) data is from NOAA Earth System Research Laboratory's Physical Sciences Division. The RTK network subscription was supplied by SmartNet for the Sydney beaches (excluding Narrabeen).

3.8 References

Barnard, P.L., Short, A.D., Harley, M.D., Splinter, K.D., Vitousek, S., Turner, I.L., Allan, J., Banno, M., Bryan, K.R., Doria, A., Hansen, J.E., Kato, S., Kuriyama, Y., Randall-Goodwin, E., Ruggiero, P., Walker, I.J., Heathfield, D.K., 2015. Coastal vulnerability across the Pacific dominated by El Nino/Southern Oscillation. Nature Geosci 8, 801-807.

Bishop, P., Cowell, P.J., 1997. Lithological and Drainage Network Determinants of the Character of Drowned, Embayed Coastlines. The Journal of Geology 105, 685-700.

Blossier, B., Bryan, K.R., Daly, C.J., Winter, C., 2017. Shore and bar cross-shore migration, rotation and breathing processes at an embayed beach. Journal of Geophysical Research: Earth Surface 122, 1745–1770.

Bryan, K.R., Foster, R., MacDonald, I., 2013. Beach Rotation at Two Adjacent Headland-Enclosed Beaches. Journal of Coastal Research, 2095-2100.

Burvingt, O., Masselink, G., Russell, P., Scott, T., 2017. Classification of beach response to extreme storms. Geomorphology 295, 722-737.

Burvingt, O., Masselink, G., Scott, T., Davidson, M., Russell, P., 2018. Climate forcing of regionally-coherent extreme storm impact and recovery on embayed beaches. Marine Geology 401, 112-128.

Castelle, B., Coco, G., 2012. The morphodynamics of rip channels on embayed beaches. Continental Shelf Research 43, 10-23.

Castelle, B., Scott, T., Brander, R.W., McCarroll, R.J., 2016. Rip current types, circulation and hazard. Earth-Science Reviews 163, 1-21.

Daly, C.J., Bryan, K.R., Winter, C., 2014. Wave energy distribution and morphological development in and around the shadow zone of an embayed beach. Coastal Engineering 93, 40-54.

Daly, C.J., Winter, C., Bryan, K.R., 2015. On the morphological development of embayed beaches. Geomorphology 248, 252-263.

Fellowes, T.E., Vila-Concejo, A., Gallop, S.L., 2019. Morphometric classification of swell-dominated embayed beaches. Marine Geology 411, 78-87.

George, D.A., Largier, J.L., Storlazzi, C.D., Barnard, P.L., 2015. Classification of rocky headlands in California with relevance to littoral cell boundary delineation. Marine

Geology 369, 137-152.
Harley, M.D., 2017. Coastal Storm Definition, In: Coastal Storms (Editors: Ciavola and Coco), Wiley, Chichester, United Kingdom, 1-19.
Harley, M.D., Turner, I.L., Middleton, J.H., Kinsela, M.A., Hanslow, D., Splinter, K.D., Mumford, P., 2017. Observations of beach recovery in SE Australia following the June 2016 east coast low. Australasian Coasts Ports 2017: Working with Nature, 559.
Harley, M.D., Turner, I.L., Short, A.D., 2015. New insights into embayed beach rotation: The importance of wave exposure and cross-shore processes. Journal of Geophysical Research: Earth Surface 120, 1470-1484.
Harley, M.D., Turner, I.L., Short, A.D., Ranasinghe, R., 2010. Interannual variability and controls of the Sydney wave climate. International Journal of Climatology 30, 1322-1335.
Harley, M.D., Turner, I.L., Short, A.D., Ranasinghe, R., 2011a. Assessment and integration of conventional, RTK-GPS and image-derived beach survey methods for daily to decadal coastal monitoring. Coastal Engineering 58, 194-205.
Harley, M.D., Turner, I.L., Short, A.D., Ranasinghe, R., 2011b. A reevaluation of coastal embayment rotation: The dominance of cross-shore versus alongshore sediment transport processes, Collaroy-Narrabeen Beach, southeast Australia. Journal of Geophysical Research: Earth Surface 116, n/a-n/a.
Hegge, B., Ian, E., H_su, J., 1996. Sheltered Sandy Beaches of Southwestern Australia. Journal of Coastal Research 12, 748-760.
Hsu, J., Evans, C., 1989. Parabolic Bay Shapes and Applications. Proceedings of the Institution of Civil Engineers 87, 557-570.
Klein, A.H.d.F., Ferreira, Ó., Dias, J.M.A., Tessler, M.G., Silveira, L.F., Benedet, L., de Menezes, J.T., de Abreu, J.G.N., 2010. Morphodynamics of structurally controlled headland-bay beaches in southeastern Brazil: A review. Coastal Engineering 57, 98-111.
Komar, P.D., 1998. Beach Processes and Sedimentation. Prentice Hall.
Loureiro, C., Ferreira, O., Cooper, J.A.G., 2009. Contrasting Morphologic Behaviour at Embayed Beaches in Southern Portugal. Journal of Coastal Research, 83-87.
Loureiro, C., Ferreira, O., Cooper, J.A.G., 2014. Non-uniformity of storm impacts on three high-energy embayed beaches.
Loureiro, C., Ferreira, Ó., COOPER, J.A.G., 2011. Morphologic change and morphodynamics at high-energy embayed beaches in southwestern Portugal, The Proceedings of the Coastal Sediments 2011: In 3 Volumes. World Scientific, pp. 1375-1389.
Loureiro, C., Ferreira, Ó., Cooper, J.A.G., 2012a. Extreme erosion on high-energy embayed beaches: Influence of megarips and storm grouping. Geomorphology 139–140, 155-171.
Loureiro, C., Ferreira, Ó., Cooper, J.A.G., 2012b. Geologically constrained morphological variability and boundary effects on embayed beaches. Marine Geology 329–331, 1-15.
Masselink, G., Castelle, B., Scott, T., Dodet, G., Suanez, S., Jackson, D., Floc'h, F., 2016a. Extreme wave activity during 2013/2014 winter and morphological impacts along the Atlantic coast of Europe. Geophysical Research Letters 43, 2135-2143.
Masselink, G., Hughes, M., Knight, J., 2014. Introduction to Coastal Processes and Geomorphology. Taylor Francis.
Masselink, G., Scott, T., Poate, T., Russell, P., Davidson, M., Conley, D., 2016b. The extreme 2013/2014 winter storms: hydrodynamic forcing and coastal response along the southwest coast of England. Earth surface processes and Landforms 41, 378-391.

McCarroll, R.J., Brander, R.W., Turner, I.L., Power, H.E., Mortlock, T.R., 2014. Lagrangian observations of circulation on an embayed beach with headland rip currents. Marine Geology 355, 173-188.

McCarroll, R.J., Brander, R.W., Turner, I.L., Van Leeuwen, B., 2016. Shoreface storm morphodynamics and mega-rip evolution at an embayed beach: Bondi Beach, NSW, Australia. Continental Shelf Research 116, 74-88.

Mortlock, T., Goodwin, I., McAneney, J., Roche, K., 2017. The June 2016 Australian East Coast Low: Importance of Wave Direction for Coastal Erosion Assessment. Water 9, 121.

Mortlock, T.R., Goodwin, I.D., 2015. Directional wave climate and power variability along the Southeast Australian shelf. Continental Shelf Research 98, 36-53.

Mortlock, T.R., Goodwin, I.D., 2016. Impacts of enhanced central Pacific ENSO on wave climate and headland-bay beach morphology. Continental Shelf Research 120, 14-25.

Morton, R.A., Jeffrey, G.P., James, C.G., 1994. Stages and Durations of Post-Storm Beach Recovery, Southeastern Texas Coast, U.S.A. Journal of Coastal Research 10, 884-908.

Pitman, S., Gallop, S.L., Haigh, I.D., Masselink, G., Ranasinghe, R., 2016. Wave breaking patterns control rip current flow regimes and surfzone retention. Marine Geology 382, 176-190.

Shand, T., Goodwin, I., Mole, M., Carley, J., Browning, S., Coghlan, I., Harley, M., Preston, W., 2010. NSW coastal inundation hazard study: coastal storms and extreme waves, Water Research Laboratory Technical Report, pp. 1-45.

Scott, T., Austin, M., Masselink, G., Russell, P., 2016a. Dynamics of rip currents associated with groynes — field measurements, modelling and implications for beach safety. Coastal Engineering 107, 53-69.

Scott, T., Masselink, G., O'Hare, T., Saulter, A., Poate, T., Russell, P., Davidson, M., Conley, D., 2016b. The extreme 2013/2014 winter storms: Beach recovery along the southwest coast of England. Marine Geology.

Shand, T., Goodwin, I., Mole, M., Carley, J., Browning, S., Coghlan, I., Harley, M., Preston, W., 2010. NSW coastal inundation hazard study: coastal storms and extreme waves, Water Research Laboratory Technical Report, pp. 1-45.

Short, A., 1978. Characteristic beach morphodynamics on the southeast Australian coast, Fourth Australian Conference on Coastal and Ocean Engineering, 1978: Managing the Coast; Preprints of Papers. Institution of Engineers, Australia, pp. 150-154.

Short, A., Trenaman, N., 1992. Wave climate of the Sydney region, an energetic and highly variable ocean wave regime. Marine and freshwater research 43, 765-791.

Short, A.D., 1993. Beaches of the New South Wales Coast; a guide to their nature, characteristics, surf and safety. Sydney University Press, Sydney.

Short, A.D., 2010. Role of geological inheritance in Australian beach morphodynamics. Coastal Engineering 57, 92-97.

Short, A.D., Masselink, G., 1999. Embayed and structurally controlled embayed beaches, Handbook of beach and shoreface morphodynamics. Wiley, Chichester, pp. 230-250.

Silvester, R., 1985. Natural headland control of beaches. Continental Shelf Research 4, 581-596.

Silvester, R., Tsuchtya, Y., Shibano, Y., 1980. Zeta bays, pocket beaches and headland control, Coastal Engineering 1980. American Society of Civil Engineers, Sydney, Australia, pp. 1306-1319.

Thom, B.G., Eliot, I., Eliot, M., Harvey, N., Rissik, D., Sharples, C., Short, A.D., Woodroffe, C.D., 2018. National sediment compartment framework for Australian coastal

management. Ocean Coastal Management 154, 103-120.
Valiente, N.G., Masselink, G., Scott, T., Conley, D., McCarroll, R.J., 2019. Role of waves and tides on depth of closure and potential for headland bypassing. Marine Geology 407, 60-75.
Vila-Concejo, A., Gallop, S.L., Largier, J.L., 2019. Sandy beaches in estuaries and bays, in: Jackson, D.W.T., Short, A.D. (Eds.), Sandy Beach Morphodynamics. Elsevier.
Wright, L.D., Short, A.D., 1984. Morphodynamic variability of surf zones and beaches: A synthesis. Marine Geology 56, 93-118.

4

Quantifying sand bar migration and vorticity from video on an embayed beach

This chapter is based on the following publication (in preparation):

Fellowes, T.E., Bryan, K., Gallop, S.L., McCarroll, R.J., Vila-Concejo, A., *In Prep*. Quantifying sand bar migration and vorticity from video on an embayed beach.

4.1 Abstract

Sand bars dynamics are extremely variable both in space and time. Their complexity is not captured well by bulk quantitative measures, such as the commonly-used cross-shore bar position. This is a particular problem for beaches embayed by headlands, where more detailed information is needed to understand how headlands influence the sand bar dynamics and overall beach and surf zone behaviour. Here we use 6 years (2012–2018) of video observations at the embayed Bondi Beach in Sydney (Australia), to quantify daily sand bar migration (M) rates and directions, and concurrent sand bar vorticity (i.e., spinning motion) (Γ). Counter-clockwise vorticity (Γ_{ccw}) occurred at locations when pixel intensity in the video images shifted from dark (rip channel) to light (sand bar with breaking waves), and vice versa for clockwise vorticity (Γ_{cw}). During fair-weather conditions, the mean M rate was $1\ m/day$ and Γ was $1.8\ x10^{-2}s^{-1}$, while during high-energy storms mean M reached up to 22.3 m/storm and mean Γ reached up to $4.1\ x10^{-2}s^{-1}$. We identified two wave energy zones alongshore (exposed and shadowed protected zone), with the zone protected by the headland experiencing 75 % of M and Γ rates of the exposed zone. We identified 4 examples of sand bar storms response patterns (combining M and Γ) from a total of 58 individual sand bar patterns to the high-energy storms including, opened sand bar-rip channel ($n = 26$), meandering sand bar/trough ($n = 15$), concentric sand bar ($n = 10$), and sand bar curvature switching ($n = 7$). Sand bar Γ and the patterns are important in up-state and down-state transitions in sand bar morphology over storm-scales. While this study extends video analyses techniques, allowing semi-automated quantification of M and Γ, and the application to the embayed Bondi Beach provides new insights into the morphological relationship with headlands and alongshore gradients during storms.

4.2 Introduction

Sand bars are sedimentary bodies that commonly characterise the surf zone of wave-dominated beaches and their morphology is a key attribute in beach state classifications (Wright and Short, 1984; Masselink and Short, 1993; Loureiro et al., 2013; van de Lageweg et al., 2013). Sand bars

influence the patterns of wave dissipation and therefore surf zone circulation (MacMahan et al., 2006; Harley et al., 2015; Pitman et al., 2016b). For example, sand bar morphology controls the location and alongshore spacing of rip channels that contain rip currents, which transport sediment and other materials within and outside of the surf zone (MacMahan et al., 2010; Gallop et al., 2011; Loureiro et al., 2012b). Sand bar migration (cross-shore and longshore) is driven by wave energy (Holman et al., 2006; Harley et al., 2015). Variations in wave energy can transition morphodynamic beach states up (more energy) or down (less energy), shifting sand bar locations, orientation and distance offshore (Wright and Short, 1984; Jackson et al., 2005; Gallop et al., 2011).

Most sand bar studies are based on open coast beaches that do not have strong geological controls. However, beaches embayed by headlands are common on the hill and cliff dominated coastlines that represent over half of the world's coast (Inman and Nordstrom, 1971). Embayed beaches are strongly controlled by their geology including the headlands (Loureiro et al., 2012b) which modify incident wave climates and sand bar morphodynamics (Cooper et al., 2004; Scott et al., 2011; Castelle and Coco, 2012). On embayed beaches, sand bar migration can be significantly impacted by wave shadowing due to the headlands (Daly et al., 2014), and headland boundary currents (Loureiro et al., 2012b). The alongshore energy-gradients due to headland shadowing can result in a gradient of high to low wave energy, with multiple morphodynamic beach states present simultaneously alongshore (McCarroll et al., 2014). Headlands can also act as barriers that contain sediment within the embayment, further impacting the nearshore sediment budget and morphodynamics (Valiente et al., 2017). The sand bar dynamics of embayed beaches are complicated further as the larger-scale embayment geometry during storms can lead to the development of powerful headland boundary rips and in extreme storms mega-rips (Loureiro et al., 2012a).

Sand bar morphodynamics and their intrinsic rip channels can be studied by observing a range of motions, including changes in orientation relative to the shoreline (Gallop et al., 2011), shifts from transverse to rhythmic morphology (Wright and Short, 1984), rip-head widening which moves the sand bar-rip boundaries alongshore increasing rip channel width (Gallop et al., 2011;

Loureiro et al., 2012a; McCarroll et al., 2016), and opening and closing of the rip channels at the seaward boundary (Pitman et al., 2016b). These changes to the sand bars and the sediment fed by rip currents can impact and modify beach cusps and the shoreline position (Orzech et al., 2011), move sand bars further offshore increasing surf zone widths (Splinter et al., 2011), or change sand bar size and number (Gallop et al., 2011; Harley et al., 2015). Changes to flow velocities and wave directions can change the sand bar orientations or even result in sand bar rotation (Bruneau et al., 2011; Pitman et al., 2016b). Under oblique waves sand bars may migrate upstream towards the exposed headland (Castelle and Coco, 2012), may merge together or separate to form new sand bars (van Enckevort and Ruessink, 2003; Coco and Murray, 2007; Blossier et al., 2017). These sand bar dynamics are captured using a range video and field techniques, but quantitatively extracting this information remains a challenge.

This study builds on the well-established field of monitoring surf zone morphology with video imagery. Detection methods for sand bars in video imagery generally use the high light intensity associated with breaking waves to locate nearshore features, by differentiating them from low light intensity associated with greater depth (rip channels and other deeper areas) and little or no wave breaking (Lippmann and Holman, 1989; Harrison et al., 2017). This differentiation has been used to study migration of flood tide deltas (Harrison et al., 2017), rip channel and sand bar locations, aspects (perpendicular or oblique) to the shoreline and migration (Gallop et al., 2009; van de Lageweg et al., 2013; Pitman et al., 2016a; Harrison et al., 2017). The majority of these studies reduce sand bar morphologies into basic measures such as embayment spacing, average migrations rates and position of the bar (the “simple” behaviour), losing much valuable information on the underlying processes. There is still much scope to move beyond qualitative descriptions of the sand bar evolution patterns such as bending, rotation, splitting, merging and changes to convexity of bars (the “complex” behaviour).

Here we propose to use vorticity (i.e., spinning motion) as an additional way to measure the non-uniformity of sand bar movement. Observations of rip currents that are present in the channels created by sand bars, often quantify the rip current vorticity (Bruneau et al., 2011; Gallop et al., 2018), generated by the strong shear zone on either side of the rip (MacMahan et

al., 2010). Vorticity in rip currents has been measured with GPS drifters (Austin et al., 2010; McCarroll et al., 2014) and numerically modelled (Reniers et al., 2004; Reniers et al., 2010). These studies have changed our understanding of sediment retention (Pitman et al., 2016b) and rip current hazards (McCarroll, 2014), by giving insight into exit points, rates and trajectories of rip currents (Gallop et al., 2018). We propose that vorticity could also be a useful measure of the rotational movement of sand bars, and, combined with more standard measures, could be used to provide new information on non-uniform beach processes. Such an approach would be particularly useful to understand the complex sand bar dynamics where there are multiple constraints and drivers, such as on embayed beaches where geological controls influence the surf zone and beach morphodynamics (Castelle and Coco, 2013).

This study has two aims. First, to develop semi-automated video analysis techniques to quantify complex and non-uniform sand bar dynamics, including their rotational component and concurrent migration rates in the cross-shore and longshore. Our spatially-resolved application of these techniques will allow, for example, quantification of subtle cross-shore variations to sand bar dynamics. Second, we aim to apply these new techniques to provide new insights into a challengingly non-uniform case: an embayed beach, where geologic control causes strongly spatially-varying processes. In the case study, we will explore how the dynamics of sand bars differ in storm and fair-weather conditions, and use our new techniques to deepen understanding of interplay between spatial gradients in wave exposure (such as caused by headland shadowing) and the non-uniform sand bar morphodynamics on embayed beaches.

4.2.1 Study site

Bondi Beach in Sydney, Australia is an 850 m-long sandy embayed beach (Figure 4.1a–c). Bondi is characterised by moderate headland influence on waves and beach morphology and accordingly is classified as a Class 2 embayed beach with respect to its degree of embaymentisation, according to Fellowes et al. (2019), Class 2 embayed beaches are the most common class (representing 43 % of embayed beaches a global assessment by Fellowes et al.

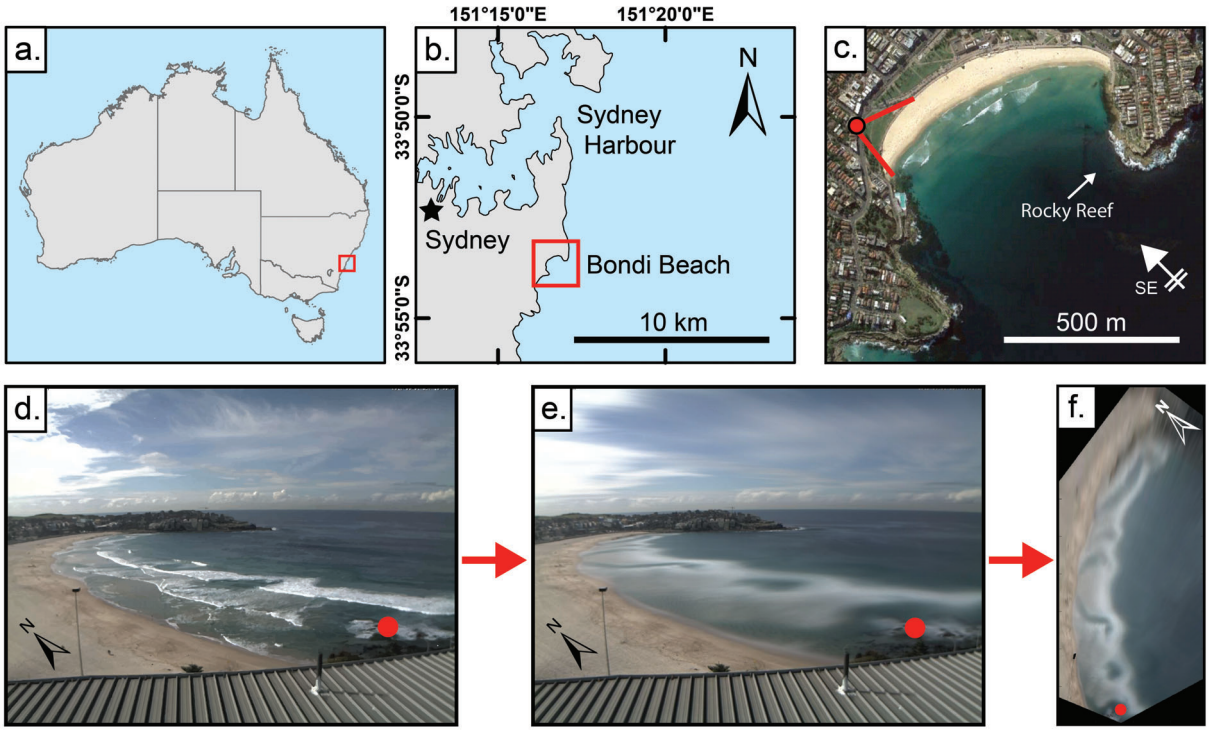

Figure 4.1: (a) Australian context, (b) Sydney and Bondi Beach (Class 2 beach, headland type H2, see Chapter 2) in the red box, (c) camera location, field of view (red), typical wave direction (white arrow) and rocky reef. Pre-processing imagery techniques (01/06/2012) at low tide with a reference point (red circle) in (d) snapshot image, (e) time-averaged (Timex) image and, (f) rectified-rotated image.

(2019)). The headlands at Bondi are asymmetrical, with one acutely and one obtusely angled from beach aspect (orientation type H2; from Fellowes et al. (2019)). The northern headland also extends into a rocky platform that further protects the beach (beach length, X_d < 200 m) and creates an alongshore wave energy gradient (Short, 2007; McCarroll et al., 2016). The beach aspect is south-southeast (SSE) overall, SSE near the southern headland and south (S) near the northern headland (Figure 4.1c). The southern end is exposed to waves (modal = SE) and common beach states are transverse bar and beach (TBR), rhythmic bar and beach (RBB) or longshore bar and trough (LBT); while, the north commonly has low tide terrace (LTT) morphology, according to the Wright and Short (1984) classification. The surf zone is typically characterised by a prominent south headland rip, several transverse (or oblique) rip channels separated by established sand bars away from the headlands, a typical low tide terrace at the north end and a typically single outer alongshore sand bar (McCarroll et al., 2016).

4.3 Methods

4.3.1 Hydrodynamics

The Sydney region is micro-tidal (< 2 m) with a spring tide range of 1.3 m, a mean significant wave height (H_s) of 1.6 m, mean peak wave period (T_p) of 10 s, and mean wave direction (θ_m) of 135° (Short and Trenaman, 1992; Harley et al., 2010). Storms were identified with the Peaks-Over-Threshold method defined in Harley (2017), using the long-term storm threshold of H_s > 3 m, a minimum storm duration of 6 hours, and defining independent storms as separated by more than 24 hours (Shand et al., 2010). Storms occur here throughout the year (Short and Trenaman, 1992) with minimal seaosnality (seasons defined using the solstice and equinox), generated by mid-latitude cyclonic systems originating from northeast to south (Mortlock and Goodwin, 2015). Wave energy (E) and power energy flux (P) were calculated following Komar (1998) as,

$$P = EC_g \tag{4.1}$$

where, wave energy E is expressed as,

$$E = \frac{1}{16}\rho g H_s^2 \tag{4.2}$$

where, ρ is seawater density (1025 kg/m^3), g is the gravitational acceleration (9.81 m/s), and wave group velocity C_g (m/s) is expressed as,

$$C_g = \frac{gT_z}{2\pi}n \tag{4.3}$$

where, n is 0.5 for deep water and T_z (s) is zero crossing period (mean period). Our investigation will look in depth at storms that exceeded the 90^{th} percentile of cumulative storm power P_{sum} (sum of hourly wave power measures per storm, when H_s > 3 m), which are herein referred to as the "high-energy storms". high-energy storms that occurred in close succession (less than 1 month apart, as defined by Birkemeier et al. (1999) are considered as a storm cluster (SC).Wave

and tide data were from the Sydney offshore Waverider (SYD) located 21 km north of Bondi in 90 m water depth and the Sydney Middle Head tide gauge, located 7.5 km north of Bondi in Sydney Harbour.

4.3.2 Image pre-processes

A 1-megapixel Mobotix M24 video camera was located 55 m above mean sea level (MSL) at the southern end of Bondi Beach from 01/06/2012 to 14/06/2018 (Figure 4.1c). Images were collected daily between 09:00–17:00 at 1 Hz (Figure 4.1d). Ten minutes of images (600 images), centred around low-tide of each day, were time-averaged (Timex) and light intensities were used to identify sand bars and rip channels (Lippmann and Holman, 1989; Smith and Bryan, 2007; van de Lageweg et al., 2013) (Figure 4.1e). These daily Timex images were rectified using COSMOS (Taborda and Silva, 2012) then rotated into planview (Figure 4.1f). We collected usable images for 60 % of all days (n = 1305) from the 6-year study period (n = 2205). Periods with no images were due to poor image quality from environmental factors (e.g., shadows, light reflection, rain) or camera maintenance (e.g., March to May 2014).

The shoreline position dX was detected using a k-means cluster analysis of the RGB (red, green blue) image intensities into 3 clusters following Wang and Adelson (1994). The cluster dominated by red pixels corresponds to exposed sand, which contrasts with the blue/green dominated cluster that represents water, swash and breaking waves in the surf zone (Smith and Bryan, 2007). The boundary between the sand and nearshore clusters is therefore an approximation of the shoreline position (Pitman et al., 2016a). Next, pixels landward of this shoreline were removed using a mask, then the remaining image was converted to greyscale. We then applied a contrast adjustment to increase contrast between breaking waves (high pixel intensity, i.e., white) and rip channels (low pixel intensity) (Kovesi, 2012).

4.3.3 Image timestacks

Timestacks are images built from rows or columns of a sequence of pixels extracted from each video image frame at the same location, so that they represent space-timeseries patterns.

Timestacks have been used to identify moving features in the morphology, for example, ebb and flood tide delta morphology (Harrison et al., 2017), beach runup and cusps (Smith and Bryan, 2007; Almar et al., 2008) and nearshore sand bars (van Enckevort et al., 2004; van de Lageweg et al., 2013). Timestacks were extracted by selecting a line of pixels (ranging from 1 to more pixels wide) at locations (x, y) from a series of daily Timex images, where each time is stored as a row in timestack array (Figure 4.2a-b). In this study, u and v were cross-shore and alongshore sand bar velocities, which were calculated using the movement of high pixel intensities in each row of the timestacks (Figure 4.2b). We used a timestack width of 80 pixels (40 m) in both the along-beach (x) and across-beach (y) directions, which for Bondi covered the approximate scale (~30 m) of sand bars and rip channels, as defined by McCarroll et al. (2016). The locations where timestacks (n = 1197) were extracted were separated by 20 pixels (10 m) to allow for timestack overlapping to capture sand bar migrations from one stack to another (Figure 4.2a).

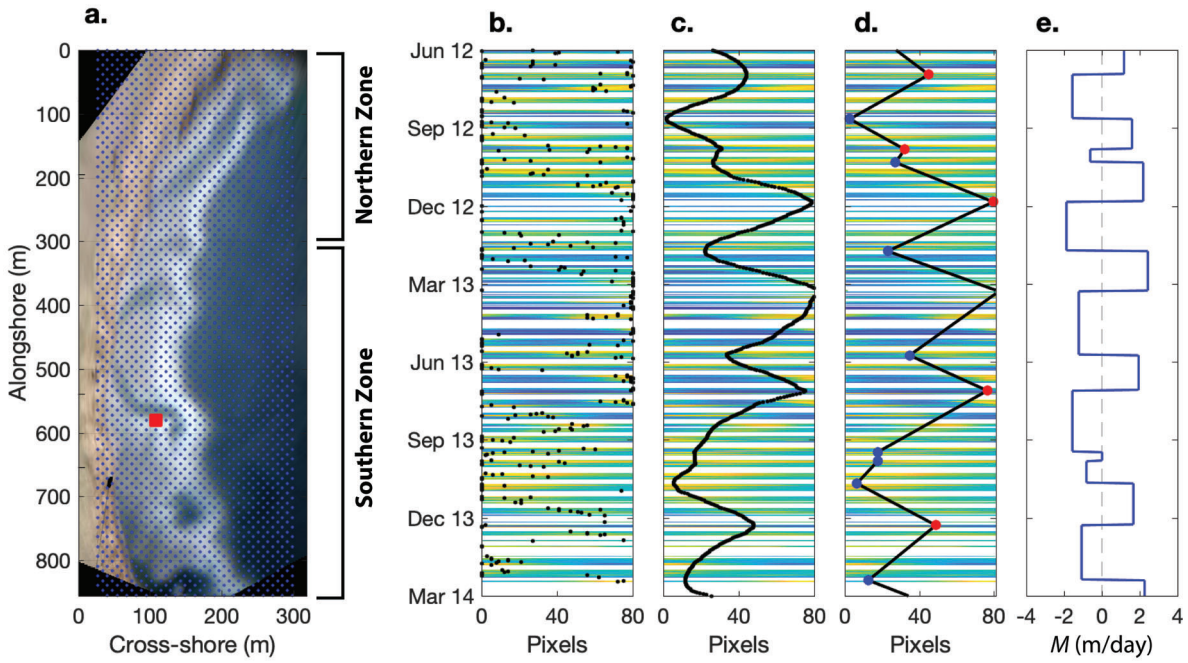

Figure 4.2: (a) Timestacks locations superimposed on rectified rotated image (01/06/2012) with extent of northern and southern zones shown. (b) alongshore timestack (red square in (a); X_d = 580 m) from 06/2012–03/2014, (b) colour represents pixel-intensity across timestack (minima=blue, maxima=yellow) with data gaps (white) and local maximum (dots), (c) smoothed line, (d) breakpoints (peaks and troughs) between migration events, and (e) migration rates M (southerly +, northerly −).

4.3.4 Sand bar analysis

Sand bars were located in each row (day) of the timestack by identifying the pixel position of maximum light intensity caused by breaking waves over the sand bars, following methods of Harrison et al. (2017) and Kovesi (2012) (Figure 4.2b). From this, locations of maximum intensity in the timestack (a timeseries of bar position) were smoothed over time to remove noise using a locally-weighted regression 2^{nd} degree polynomial model similar to smoothing methods of van de Lageweg et al. (2013). We used a model span of 60 days based on a visual assessment of typical length of sand bar migration events at Bondi. This process assigned a lower weight to outlying maximum pixel positions (Figure 4.2c) and the modelled curve reduces the influence of variations in maximum pixel-intensity from temporal changes in wave breaking (Kovesi, 2012). The slope of the line tracks the sand bar migration through the timestack. Slope breakpoints (local maxima and minima) in the curve were identified as points in time when a migration event started or finished (Figure 4.2d). The slope between two breakpoints is used to represent the behaviour (i.e., speed and direction) of each identified sand bar event (m/day), expressed as,

$$u = \frac{x_2 - x_1}{t_2 - t_1} \tag{4.4}$$

where, x_1 and x_2 to are the start and finish breakpoints and t_1 and t_2 are the start and finish dates for the migration between these breakpoints, from here on called a "migration event" (Figure 4.2e). Each slope value was assigned to all days covered by sand bar migration event between these breakpoints (Figure 4.2e). This process allowed interpolation of the data for days with missing images, resulting in a complete dataset. Sand bar migrations (M) were converted to vector form by combining alongshore u and cross-shore v velocity components (which were extracted from alongshore M_{along} and cross-shore M_{cross} timestacks respectively),

$$M = \sqrt{u^2 + v^2} \tag{4.5}$$

The final step was to calculate sand bar vorticity (Γ) calculated using the discrete form of the weighted central-difference method of MacMahan et al. (2010),

$$\Gamma = \frac{dv}{dx} - \frac{du}{dy} \tag{4.6}$$

where, v and u are the alongshore and cross-shore velocities at location (x, y) with Γ in either a positive counter-clockwise Γ_{ccw} or negative clockwise Γ_{cw} direction.

4.4 Results

4.4.1 Hydrodynamics

During the study (2012–2018), the mean offshore mean wave climate was H_s of 1.6 m, T of 6.5 m, T_p of 10 s and θ_m of 135° and mean hourly P was 0.011 $x10^3 Kw/m$ (Figure 4.3). Using the Peaks-Over-Threshold method, we identified 114 storms with a mean duration of 33 hours and cumulative storm power P_{sum} (summation of storm hourly P) of 1.37 $x10^3 Kw/m$ (Figure 4.3d). There were 11 high-energy storms (S1–S11) that exceeded the 90^{th} percentile for P_{sum} (3.04 $x10^3 Kw/m$), that form the basis of our investigation into sand bar dynamics (Figure 4.3d; Table 4.1). The mean spacing for these high-energy storms was 215 days (~7 months) and seasonally there were 5 in Austral autumn (S1, S3, S8, S9 and S11) and winter (S2, S4, S5, S6 and S7), 1 in summer (S10) and none recorded in spring. Additionally, two storm-clusters were identified (where storms were less than 1 month apart), with the first cluster (SC1) in June 2013 (n = 2; S3–S4) separated by 5 days and the second cluster (SC2) in July–September 2014 (n = 3; S5–S7) and were separated by 29 and 13 days respectively (Figure 4.3d; Table 4.1).

4.4.2 Sand bar morphodynamics

4.4.2.1 Migration and vorticity correlations to storm wave power

Sand bar morphodynamics were studied within two zones (measured as beach length, X_d from north) that were separated based on their geomorphological setting (Figure 4.1c). The northern

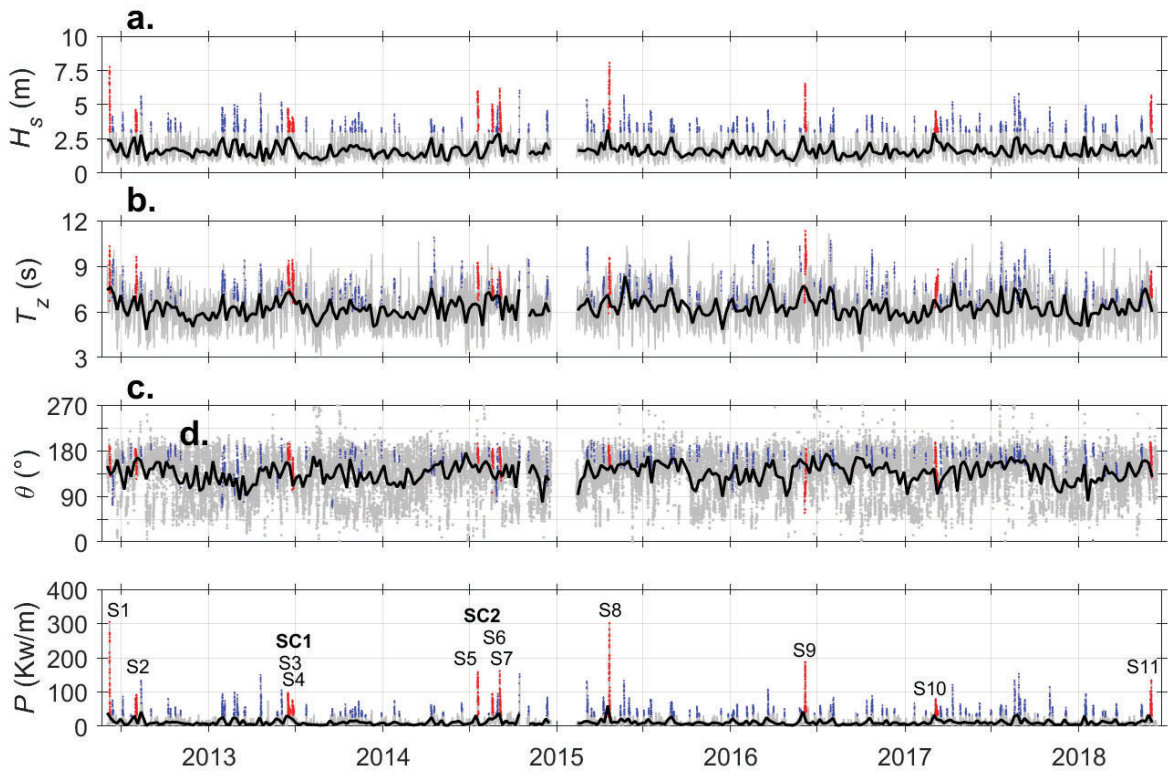

Figure 4.3: Sydney hourly offshore wave data (grey), 7-day running-averages (black), storm data (blue) and high-energy storms (S1–S11) in red and storm clusters (SC1–SC2). (a) Significant wave height (H_s), (b) mean wave period (T_z), (c) wave direction (θ) and (d) wave power energy flux (P). Note instrument maintenance in late 2014–early 2015.

zone (X_d < 300 m) was largely shadowed from waves by the northern headland and typically received only modified waves that were refracted by this headland and the associated rocky reef. Conversely, the southern zone (X_d = 300–850 m) was typically exposed to unmodified waves (Figure 4.3c) (see Chapter 3 for headland shadow analysis). An assessment of sand bar behaviour during all storms (n = 114) showed that cumulative sand bar migration during each storm (M_{sum}; summation of M_{along} and M_{cross}) was positively and significantly correlated with P_{sum} (Figure 4.4a). Furthermore, there was a wave power energy threshold (P_{sum} $x10^2 Kw/m$) whereby there was no significant correlation between P_{sum} and M_{sum} for storms below this P_{sum} amount as the values showed a wide distribution in both variables (Figure 4.4a). For the high-energy storms (S1–S11) there was no significant correlation found between P_{sum} and M_{sum} (Figure 4.4a). The relationship between cumulative storm vorticity for each storm (sum; summation of θ_{ccw} and θ_{cw}) and P_{sum} had a similar pattern, in that there was a P_{sum} threshold at the same 0.75

$x10^3 Kw/m$; whereby above this threshold there was a significant positive correlation between P_{sum} and Γ_{sum}, but below there was no significant correlation (Figure 4.4b).

Table 4.1: Storm statistics from the high-energy storms (H_s > 3 m and > 90^{th} percentile P_{sum}) (S1–S11) from the SYD buoy 2015–2018.

Storm ID	**S1**	**S2**	**S3**	**S4**	**S5**	**S6**	**S7**	**S8**	**S9**	**S10**	**S11**
Storm Dates	05–07 Jun 2012	30 Jul–2-Aug 2012	15–19 Jun 2013	24–28 Jun 2013	18–20 Jul 2014	18–20 Aug 2014	02–06 Sept 2014	19–22 Apr 2015	04–07 Jun 2016	04–11 Mar 2017	31 May – 3-Jun 2018
Duration (hours)	41	71	112	80	47	62	80	73	75	168	69
Mean H_s (m)	5.3	3.8	3.7	3.4	4.8	4	4.1	5.1	4.2	3.5	4.2
Max H_{max} (m)	13.8	8.5	9.1	7.7	11.4	9.6	12.1	14.9	12	8.6	10
Mean T_z (s)	8.6	7.9	8.1	8.1	8.2	7.4	7.6	7.9	9.1	7.4	7.6
Mean T_p (s)	12.7	12.5	11.3	10.9	11.9	10.4	11.6	11.3	14	11.2	11.5
Mean θ_w (°)	163	158	173	131	172	164	160	167	119	146	171
Mean θ_w (bearing)	SSE	S	S	ESE	S	SSE	SSE	SSE	ESE	SE	S
P_{sum} $x10^3$ **(Kw/m)**	5.25	3.41	4.84	3.04	4.59	3.25	4.96	7.86	6.35	3.89	4.24

Normalised migration (M_{norm}; M_{sum} divided by number of storm days) and normalised vorticity (Γ_{norm}; Γ_{sum} divided by number of storm days) showed a weak but significant positive correlation for all the storms (n = 114) (Figure 4.4c). Moreover, those storms that fall below the P_{sum} threshold of 0.75 $x10^3 Kw/m$ still showed a strong significant correlation between M_{norm} and Γ_{norm}, while the high-energy storms showed no correlation between these two variables (Figure 4.4c). A comparison of M_{norm} and storm duration showed that there was a duration threshold of 14 hours, whereby storms that were shorter than these events, showed a great range in both M_{norm} and Γ_{norm} and that both were not correlated with duration (Figure 4.4d). The storms with a length above this duration threshold showed a significant positive correlation with M_{norm} and a significant decreasing correlation Γ_{norm} (Figure 4.4d). Also, the duration and M_{norm} of the high-energy storms (S1–S11) were positively correlated, while Γ_{norm} was not correlated (Figure 4.4d).

4.4.2.2 Sand bar migration rates with wave exposure

Sand bar morphodynamics were assessed during fair weather conditions and the high-energy storms (S1–S11), with the detailed migration and vorticity patterns presented in Supplementary

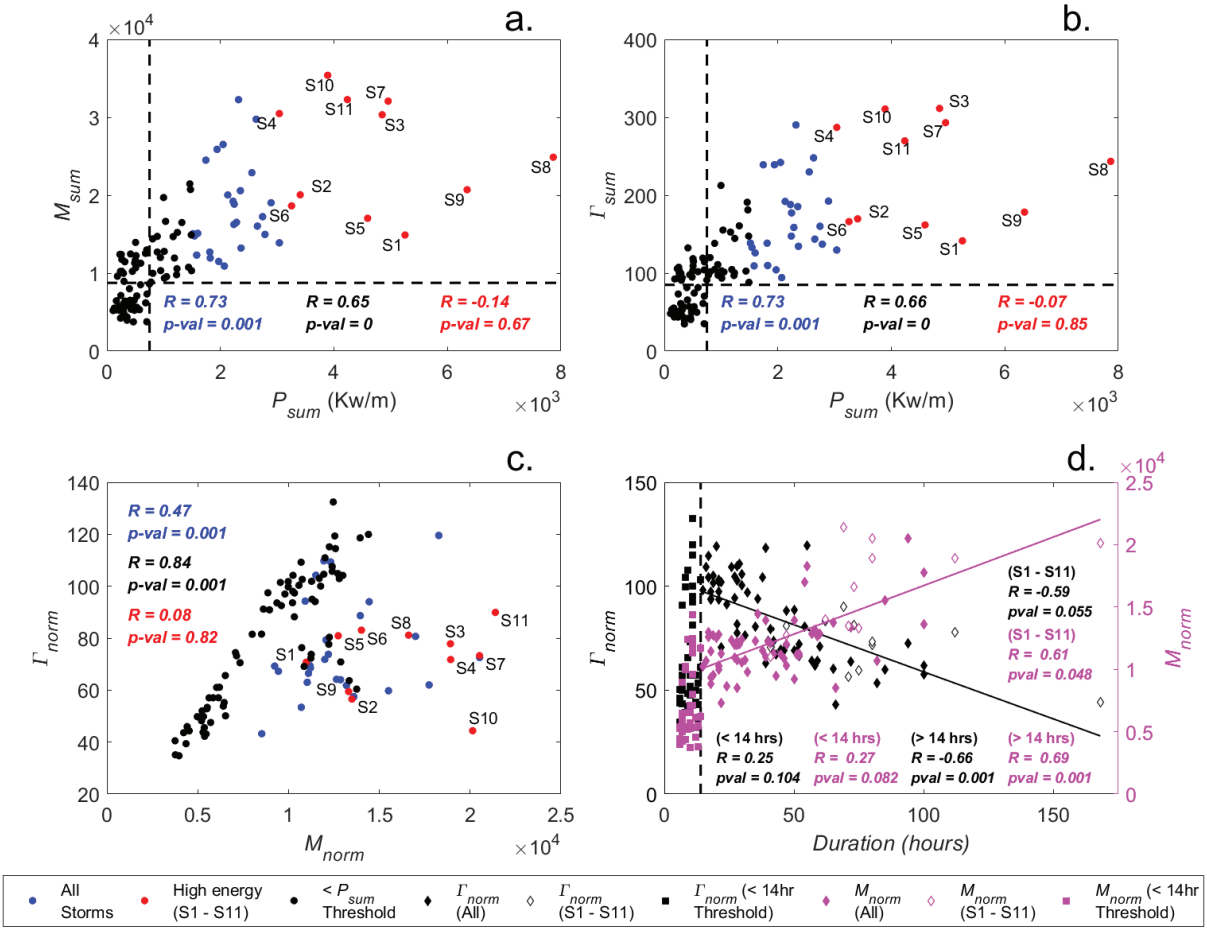

Figure 4.4: Storm statistics and sand bar behaviour. (a) M_{sum} (summation of M_{along} and M_{cross} from all days of storm) and cumulative storm power P_{sum} (summation of all hourly power P within storm when H_s > 3 m) for all storms (blue), storms below a P_{sum} threshold of 0.75 $x10^3 Kw/m$ (black) and the high-energy storms (red), (b) Γ_{sum} (summation of Γ_{ccw} and $|\Gamma_{cw}|$ from all days of storm) and P_{sum} for the same three categories in (a), (c), M_{norm} (M_{sum} divided by number of storm days) and norm (sum divided by number of storm days) for the same three coloured categories in (a), and (d) comparisons between M_{norm} and norm with storm duration (hours) with all storms (solid pink and black diamond), those below the duration threshold of 14 hours (solid pink and black squares) and high-energy storms (hollow pink and black diamonds).

Tables S2-S3 and Supplementary Figures S3-S13, and we summarised these here. During fair-weather conditions, the mean sand bar migration rates were 1 m/day for alongshore migration (M_{along}) and 0.9 m/day for cross-shore migration (M_{cross}). The northern zone (defined as all migration values in the northern zone X_d = 0–300 m) had mean M_{along} of 0.8 m/day and M_{cross} of 0.9 m/day compared to the southern zone (defined as all migration values for X_d > 300 m in the southern zone) which had mean M_{along} of 0.95 m/day and M_{cross} of 1 m/day (Table 4.2).

For the 11 high-energy storms, the mean and maximum rates were significantly higher than the study average, with mean M of 2.8 m/storm for both M_{along} and M_{cross} (Table 4.2). The mean maximum migration (M) from the high-energy storms was 15.7 m/storm for M_{along} and 16.1 m/storm for M_{cross} (Table 4.2). The maximum migration recorded from an individual event for M_{along} was 22 m/storm (event mean = 4 m) during March 2017 (S10; θ_w = SE) (Figure 4.5a) and for M_{cross} was 22.3 m/storm (event mean = 3.4 m) during June 2013 (S4; θ_w = ESE) (Table 2). Other high-energy storms that had mean M over 15 m/storm for both M_{along} and M_{cross} include June 2013 (S3; θ_w = S), September 2015 (S7; θ_w = SSE) and June 2018 (S11; θ_w = S), while April 2017 (S8; θ_w = SSE) had > 15 m/storm for M_{cross} only (Table 4.2; Figure 4.5d).

Table 4.2: Sand bar migration (M) in both M_{along} and M_{cross} directions for the high-energy storms (S1–S11) with mean, maximum and standard deviation (σ) for the northern zone (X_d = 0–300 m), the southern zone (X_d = 0–300 m) and the whole beach (both zones).

	Northern Zone						**Southern Zone**						**Beach (both zones)**					
	M_{along}			M_{cross}			M_{along}			M_{cross}			M_{along}			M_{cross}		
Storm	**Mean**	**Max**	σ	**Mean**	**Max**	σ	**Mean**	**Max**	σ	**Mean**	**Max**	σ	**Mean**	**Max**	σ	**Mean**	**Max**	σ
S1	0.9	7.1	1.2	1.1	7.5	1.6	1.7	11.4	2.1	1.9	13.3	2.2	1.5	11.4	1.8	1.7	13.3	2
S2	1.4	9.2	1.7	1.3	9	1.6	2.6	13.3	2.8	2.6	13.8	2.7	2.3	13.3	2.5	2.3	13.8	2.4
S3	2.5	13	3.2	2.7	13.5	3.4	3.7	17.8	4	3.6	17.1	3.8	3.4	17.8	3.8	3.4	17.1	3.7
S4	2.6	13.2	3.3	2.8	13.5	3.6	3.7	18.7	4	3.7	22.3	3.8	3.4	18.7	3.8	3.4	22.3	3.7
S5	1.3	7.2	1.6	1.3	9.5	1.6	2.1	9.7	2.2	2.1	11.6	2.2	1.8	9.7	2	1.9	11.6	2.1
S6	1.4	8.5	1.7	1.3	8	1.6	2.3	10.6	2.5	2.3	11.8	2.4	2.1	10.6	2.2	2	11.8	2.2
S7	2.4	14.4	2.9	2.2	13.2	2.7	4.3	20.9	4.6	4	17.7	4.1	3.8	20.9	4.1	3.5	17.7	3.7
S8	2.3	11.2	2.7	2.2	12.9	2.7	2.9	14.4	3.3	2.9	15.4	3.3	2.7	14.4	3.1	2.7	15.4	3.2
S9	1.8	10.2	2.2	1.9	11.1	2.5	2.2	14.6	2.6	2.6	11.7	2.8	2.1	14.6	2.5	2.4	11.7	2.7
S10	3.5	21.4	4.4	3.7	21.7	4.8	4.1	22	4.5	4.3	21.3	4.8	4	22	4.5	4.1	21.7	4.8
S11	3.1	18.8	3.9	3.3	17.9	4.1	3.6	19.6	4.5	3.6	20.6	4.4	3.5	19.6	4.3	3.5	20.6	4.3

4.4.2.3 Sand bar vorticity and wave exposure

During fair-weather conditions, the mean daily Γ_{ccw} and Γ_{cw} were both 1.8 $x10^{-2}s^{-1}$ (Table 4.3). The northern zone had mean Γ_{ccw} and Γ_{cw} each of 1.6 $x10^{-2}s^{-1}$ which is 20 % lower vorticity compared with the southern zone that had mean Γ_{ccw} and Γ_{cw} of 2.0 and 2.1 $x10^{-2}s^{-1}$ respectively (Table 4.3). This compares to the Γ experienced during the high-energy storms that had means of 2.5 $x10^{-2}s^{-1}$ for Γ_{ccw} and 2.6 $x10^{-2}s^{-1}$ for Γ_{cw} (Table 4.3). The mean maximum

from the high-energy storms was 5.3 $x10^{-2}s^{-1}$ for Γ_{ccw} and 5.6 $x10^{-2}s^{-1}$ for Γ_{cw}; while the storm with the highest recorded Γ occurred from the unusual southerly wave direction during June 2013 (S3; Γ_w = S) with Γ_{ccw} = 7.9 $x10^{-2}s^{-1}$ and Γ_{cw} = 101.8 $x10^{-2}s^{-1}$ (Table 4.3). The northern zone typically had lower Γ_{ccw} and Γ_{cw} than the southern zone (Table 4.3).

Table 4.3: Sand bar vorticity (Γ) ($x10^{-2}s^{-1}$) in both directions (Γ_{ccw} and $|\Gamma_{cw}|$) for the high-energy storms (S1–S11) with mean, maximum and standard deviation (σ) for the northern zone (X_d = 0–300 m), the southern zone (X_d = 0–300 m) and the whole beach (both zones).

	Northern Zone						**Southern Zone**						**Beach (both zones)**					
	Γ_{ccw}			Γ_{cw}			Γ_{ccw}			Γ_{cw}			Γ_{ccw}			Γ_{cw}		
Storm	Mean	Max	σ	Mean	Max	σ	Mean	Max	σ	Mean	Max	σ	Mean	Max	σ	Mean	Max	σ
S1	0.8	12.8	1.8	1	21.2	2.2	1.6	39.4	3.6	1.9	24.2	3.5	1.4	39.5	3.1	1.6	24.2	3.2
S2	1	21.3	2.4	1.1	17.3	2.5	2.3	36.7	4.4	2.2	43.8	4.1	1.9	36.7	3.8	1.9	43.8	3.7
S3	2.3	45.9	5.5	2.2	43.6	5	3.7	79.3	7.8	4.1	101.8	8.5	3.3	79.3	7.2	3.6	101.8	7.6
S4	1.7	59.9	4.9	1.7	44.2	3.7	3.9	54.1	7.8	3.7	80	7.7	3.3	59.9	7	3.2	80.1	6.6
S5	1.1	25.6	2.7	1.1	24.8	2.5	1.9	41.1	4	2.1	38.3	4	1.7	41.1	3.7	1.8	38.3	3.6
S6	1.2	25.1	3	1.3	32.1	3	1.9	54.6	4	2.1	34	4.5	1.7	54.6	3.8	1.9	34	4.1
S7	2.1	51.6	4.8	2.3	47.7	5.5	3.6	65.7	7.2	3.9	74	8.1	3.2	65.7	6.6	3.5	74	7.4
S8	2	39.6	4.6	1.9	53.8	4.6	2.9	57.8	6.9	3	48.1	5.5	2.7	57.8	6.3	2.7	53.8	5.3
S9	1.5	31.9	3.5	1.4	28.6	3.2	2.2	37.9	4.1	2.1	43.5	4.6	2	37.9	3.9	1.9	43.5	4.2
S10	2.6	50.8	5.7	2.9	60.9	6.2	3.8	55.5	6.8	4.1	66.2	8	3.4	55.5	6.5	3.8	66.2	7.5
S11	2.4	51.6	5.7	2.4	29.9	4.8	3.2	53.9	6.9	3.1	55.7	6.9	3	53.9	6.5	2.9	55.7	6.3

4.4.2.4 Example sand bar storm response patterns

Here we present 4 key examples (types) of sand bar storm responses at Bondi that combine vorticity (Γ_{cw} or Γ_{ccw}) and migration, that supported the observed changes in pixel light intensity, sand bar morphology pre- and post-storm (Figure 4.5a–d; Supplementary Figures S3-S13) and visualised the storm correlations between Γ and M (Figure 4.4). Our observations at Bondi showed that changes from high intensity (sand bar) to low intensity (rip channel) were associated with Γ_{cw} (e.g., X_d = 700m; Figure 4.4b); while the reverse was seen for Γ_{ccw} (e.g., X_d = 550 m; Figure 4.5c). The 4 key examples of sand bar response pattern are listed for each high-energy storm in Supplementary Table S3 and pre and post storm images and sand bar dynamics (M and Γ) for each high-energy storm and these response patterns can be seen in Supplementary Figures S3-S13. General discussions presented here come from 58 individual sand bar observations from the 11 high-energy storms (Figure 4.5).

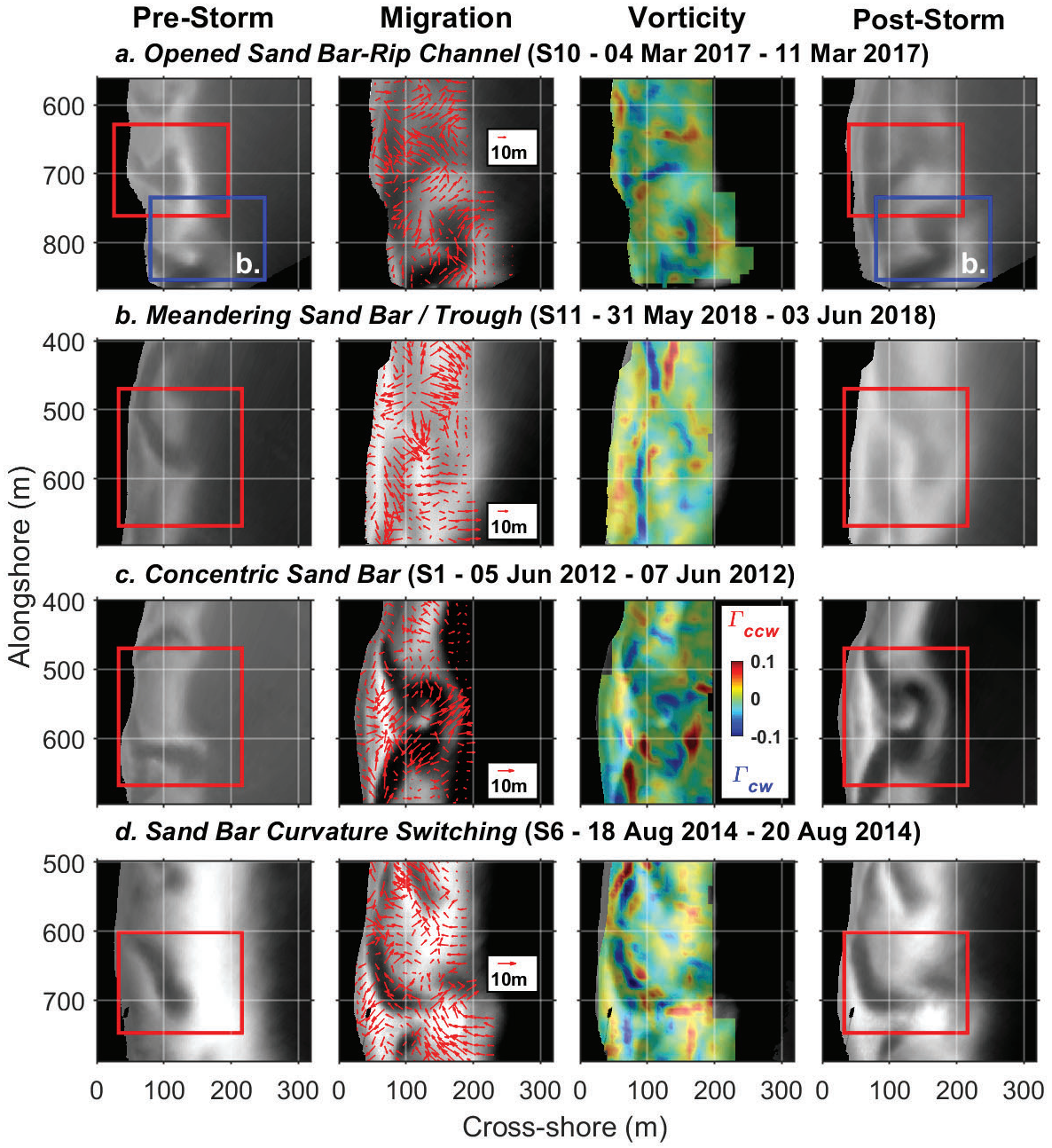

Figure 4.5: Common sand bar response patterns to storms including, (a) opened sand bar-rip channel, (b) sand bar curvature switching, (c) concentric sand bar, and (d) meandering sand bar/trough (S11, May 2018) with a second example in (a) (blue box). Note, that 75 % of presented patterns occurred in the exposed southern zone.

These example patterns included, *opened sand bar – rip channel* (Figure 4.5a; n = 26 or 45 % observations), that occurred under all storm wave directions and saw sand bar-rip channel boundaries migrate seaward with boundary spreading alongshore and migration away from the

channel resulting in an opened rip channel head (Figure 4.5a). This migration was coupled with Γ_{ccw} along channel boundaries and with Γ_{cw} at the pre-storm location of closed sand bar rip channel head (Figure 4.5a). The *meandering sand bar/trough* (Figure 4.5b; n = 15 or 26 % observations) occurred under all storm wave directions and saw meanders resulting in oblique or rhythmic rip channels that formed morphologies that span multiple beach state formations and may represent shift from TBR to RBB (4.5b). This was coupled with convergent migration and Γ_{ccw} at newly formed sand bars and Γ_{cw} on the edges of the alongshore troughs (Figure 4.5b). The *concentric sand bar* (Figure 4.5c; n = 10 or 17 % observations), occurred under all storm wave directions and saw extension of the sand bars seawards with Γ_{ccw} with Γ_{cw} along the troughs and convergent migrations that formed a developed concentric (circular) sand bar, potentially representing shifts from TBR to RBB (Figure 4.5c). The *sand bar curvature switching* (4.5d; n = 7 or 12 % observations) occurred under oblique waves and saw sand bar curvature or orientation (angle) switch (e.g., convex to concave or oblique to perpendicular) with Γ_{cw} along the seaward rip channel margins and Γ_{ccw} at locations of sand bar boundary extension resulting in an orientation curvature switch (Figure 4.5d).

4.4.3 Temporal analysis

Daily mean migration showed a general trend that when M_{along} was southerly, the bars also tended to move offshore, while when M_{along} was moving northerly, bars also tended to move onshore (Figure 4.6b–d). While, mean M_{cross} varied alongshore and showed more localised cross-shore migration patterns that were most variable in the southern zone over the northern zone (Figure 4.6b). Locations and morphodynamics of the typical transverse and oblique sand bars and rip channels were predominantly (~75 %) in the southern exposed zone (Figure 4.5; Supplementary Table S3). Both M_{along} and M_{cross} were significantly correlated with daily mean P (R = 0.063, $p - value$ = 0.023 and R = -0.056, $p - value$ = 0.044 respectively). Following the high-energy storms, the M_{along} and M_{cross} sand bar reorganisation commonly occurred along the entire beach length (e.g., post-S4 in June 2013 and post-S10) (Figure 4.6a–d). These post-storm migration responses, showed that response to the storms lasted on average 36 days (σ ±16 days), ranging from 12 (S10 March 2017) to 57 days (S4 September 2014 and post-SC1)

(Figure 4.6b–c), before a new sand bar response began (Figure 4.6d).

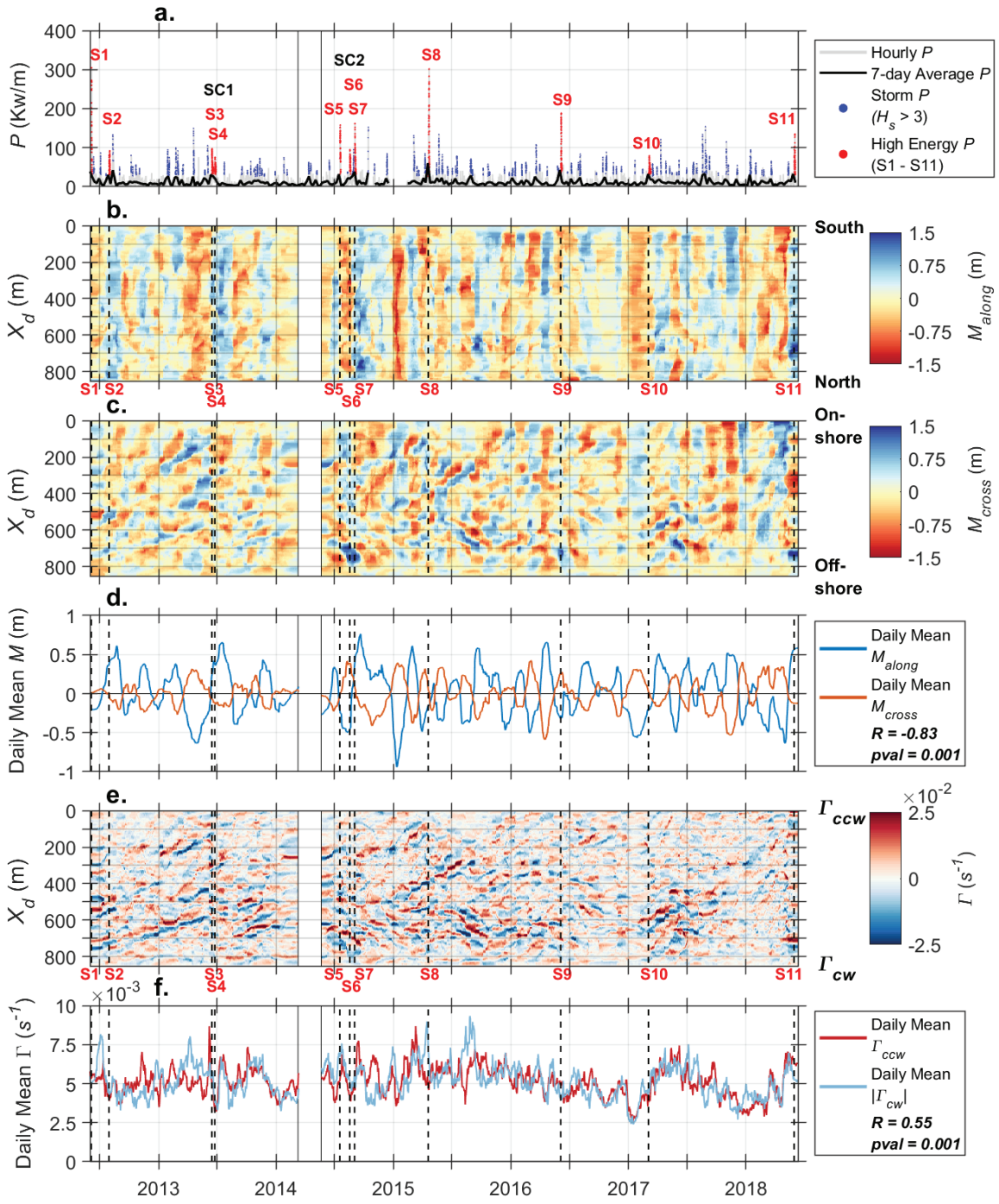

Figure 4.6: Temporal analysis of sand bars along the beach (X_d) with corresponding correlations. (a) wave power P with hourly (grey), 7 day moving average (black), all storms (blue) and high-energy storms (red), (b) alongshore migration M_{along} (m) north (red) and south (blue), (c) cross-shore migration M_{cross} (m) offshore (blue) and onshore (red), (d) daily mean M_{along} (light blue) and M_{cross} (orange), (e) sand bar vorticity Γ in both directions Γ_{ccw} (red) and Γ_{cw} (blue), and, (f) daily mean Γ_{ccw} (red) and absolute daily mean $|\Gamma_{cw}|$ (light blue). Black-edged box is a time of camera maintenance (March–May 2014, 72 days).

Seasonally, the sand bars were the most active in the Austral autumn and winter when 10 of the 11 high-energy storms occurred and the sand bar dynamics were most variable (Figure 4.6a–c and e; Figure 4.7). Austral summer conditions were below the average for migration and vorticity compared to the other seasons which all have mean values above or similar the study averages (Figure 4.7); while Autumn consistently had the highest seasonal migration and vorticity. Meanwhile vorticity was below average also in winter but more than summer (Figure 4.7a–d). Seasonally M_{cross} was higher than M_{along} which peaked in spring (Figure 4.7a–b).

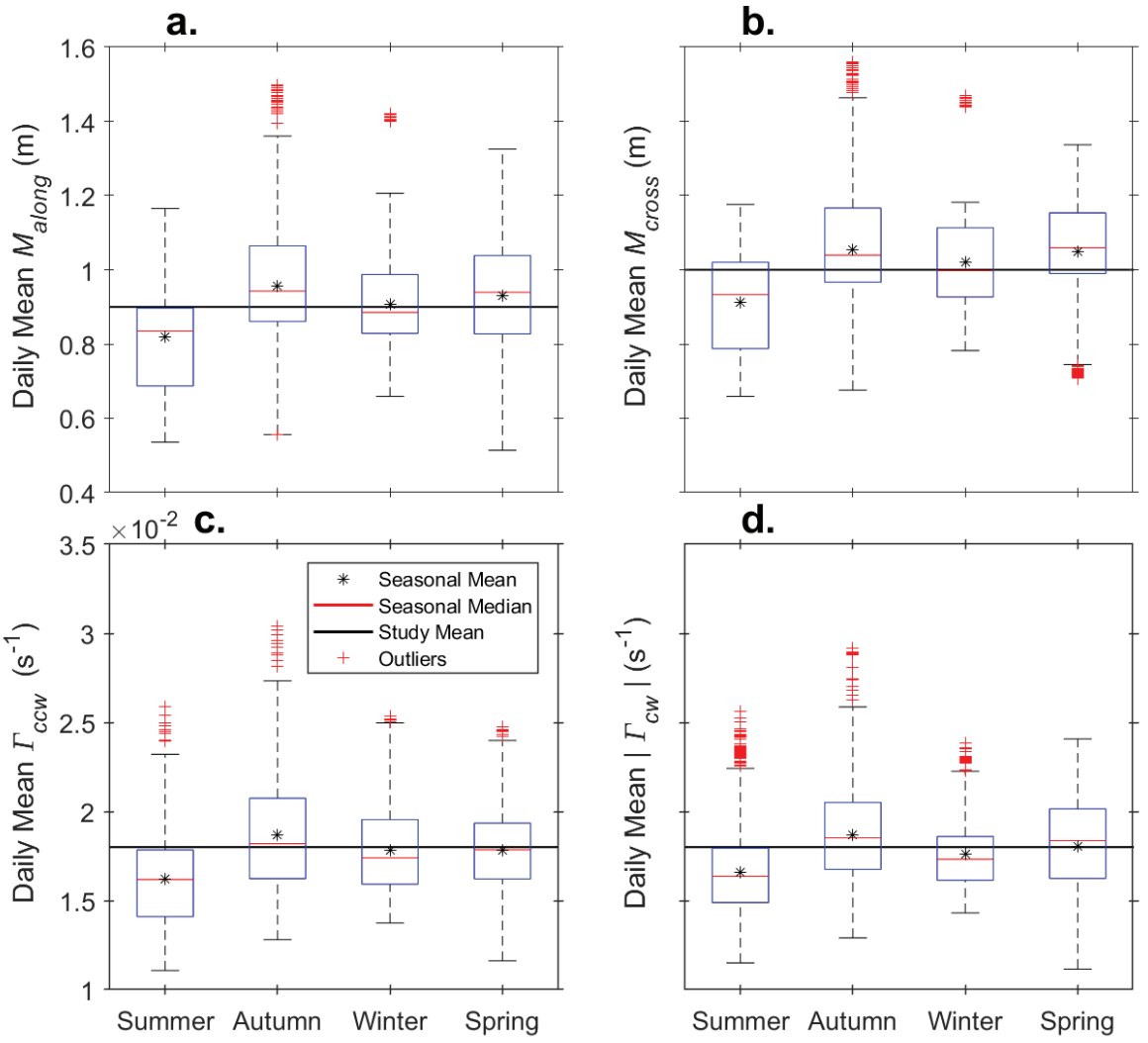

Figure 4.7: Austral seasonal daily sand bar migration (a) M_{along} and (b) M_{cross} in m and vorticity (Γ_{ccw} or $|\Gamma_{cw}|$) in s^{-1}, with seasonal mean (star), seasonal median (red line), study mean (black lines) and outlying data points (red cross).

4.5 Discussion

4.5.1 Sand bar vorticity and migration patterns during storms

In this study, we provide new techniques for providing detailed understanding of sand bar movement from video imagery, applying this to an embayed beach (Figure 4.2). These methods allow deeper exploration of sand bar evolution patterns such as bending, rotation, splitting, merging and changes to convexity of bars (Figure 4.5). We quantify sand bar vorticity (Γ) by modifying an approach detailed in MacMahan et al. (2010) that is typically for rip current flows. Rip current vorticity commonly occurs from strong shear zones on either side of the rip channel (MacMahan et al., 2010) or lagrangian coherent structure processes (Reniers et al., 2010). We suggest that these edge-related current flows initiate the erosion/accretion patterns associated with our sand bar vorticity measurements (Figure 4.5). Tributary or exiting vorticity currents have been shown to be lower in velocity and energy than the main rip current flow (Gallop et al., 2018) and reductions in energy allow the deposition of suspended sediments from interactions with the bed or shear zones and with incident wave dissipation over the sand bars (Pitman et al., 2016b). We show that there is a change in pixel intensity in locations where our methods detect sand bar Γ on the leading edges of prograding sand bars that are characterised by locations of Γ_{ccw} (Figure 4.5b–c). On the contrary, change in pixel intensity in locations at the centre of deep channels or areas in the surf zone become deeper with Γ_{cw} signals (Figure 4.5; Supplementary Figure S3). MacMahan et al. (2010) shows that the maximum flow vorticities associate with the main rip current found in the deepest part of the channel. We also show that sand bar vorticity Γ correlates with M_{cross} 4.6b–d), suggesting vorticity is an important component in the offshore migration of sand bar during storms (Figure 4.5d). Offshore migration links to increases in wave energy (Masselink et al., 2014; Blossier et al., 2016), with elevations to M_{cross} due to the high-energy storms (Table 4.2; Table 4.3) and post-storm (Figure 4.6b–c).

Here we show 4 key examples of sand bar response patterns to high energy-storms (Figure 4.5; Supplementary Table S3), that visualise the migration and vorticity storm correlations (e.g.,

Γ_{sum} and M_{sum}, and Γ_{norm} and M_{norm}) in Figure 4.4. The opened sand bar/rip channel pattern (Figure 4.5a) associates with the opening of closed rip channels, that is known to occur from fast rip currents offshore (Castelle et al., 2016) and recirculation and retention of sediments (Pitman et al., 2016b) and supports typical up-state morphological changes (Wright and Short, 1984). We associate meandering sand bar and trough and concentric sand bar response patterns (Figure 4.5b–c) with alongshore currents, which Deigaard et al. (1999) shows mobilises sediments and encourages sand bar progradation. Coco and Murray (2007) further show meandering or concentric channels add sediments to prograding rhythmic sand bars. The sand bar curvature switching pattern (Figure 4.5d) occurs predominantly under oblique waves (e.g., ESE or S) to the beach aspect (SSE), with McCarroll et al. (2018) showing wave obliquity promotes vorticity in rip channels, in conjunction with headland boundary currents and wave deflection processes on embayed beaches (Castelle et al., 2016; Gallop et al., 2018). Sediment redistribution typically follows circulation patterns through rip channels with exit points, trajectories and vorticity hard to predict (Castelle and Coco, 2012; McCarroll, 2014; Gallop et al., 2018).

4.5.2 Influence of headlands on sand bars

Sand bar migration rates and vorticity due to storms are higher (up to 50 %) and modally 15–25 % higher in the zone of the beach that is not shadowed by headlands or an offshore rocky reef (southern zone) and that receives unmodified ocean waves (Figure 4.2a; Table 4.2; Table 4.3). A general trend of southerly and offshore migration and northerly onshore is evident at Bondi (Figure 4.6d). This relates to alongshore wave exposure variance, which at Bondi Beach is from headland asymmetry (north protected from acute orientation to beach aspect) and the resulting alongshore energy gradient in waves and morphodynamic (McCarroll et al., 2016). In the exposed southern zone, the headland boundary rip at the upstream south headland opened during multiple high-energy storms (e.g., S2, S7, S9 S11) that were predominantly from SSE to S when wave exposure was greatest (Table 4.1). This headland wave deflection to waves encourages alongshore currents towards the upstream headland (Castelle et al., 2016) and can encourage mega-rip formations. For example, McCarroll et al. (2016) found at that Bondi, mega-rips form elaborate rhythmic sand bars at the offshore adjacent area near the headland

and that this sand bar morphologies did not conform to the established morphology frameworks of Wright and Short (1984). Meanwhile, reductions in sand bar migration and vorticity in the protected zone relates to the processes of headland shadowing, evident in the previous works of Castelle et al. (2016). We further show that an alongshore wave energy gradient impacts the occurrences of the 4 key example sand bar response patterns (Figure 4.5), with 75 % of sand bar response patterns observations in the exposed zone (Supplementary Table S3). We show that wave exposure is required to significantly cause a sand bar response to storms (Figure 4.4a–d) or encourage up-state shifts (e.g., TBR to RBB) in sand bar morphologies (Figure 4.5; Supplementary Figures S3, S6, S12-S13; Supplementary Table S3). This is shown to require unmodified waves without headland shadowing (Coco and Murray, 2007; McCarroll et al., 2014). Our general sand bar storm responses, particularly the morphological shifts (e.g., TBR to RBB), the spacing and the number of sand bars (and rip channels) align with previous findings that relate morphodynamics to wave exposure and headland shadowing (Gallop et al., 2011). However, our sand bar response patterns utilise concurrent sand bar migration and vorticity to give greater understanding of wave impacts, headland exposure and antecedent sand bar morphology on storm sand bar morphodynamics.

4.5.3 Storm power, clusters and sand bar response

Wave energy and the frequency of high-energy storms are a main control of sand bar morphodynamics at Bondi (Figure 4.3; Figure 4.6b–f; Table 4.1). Seasonally, the high-energy storms and storm clusters impact beach sand bar response where reworking dominates migration for at least a month (mean 36 days) (Figure 4.3b–c; Table 4.1). This type of sand bar response is suggested to be part of positive feedback that adjusts sand bar morphology though self-organisation instead of waves directly (van Enckevort et al., 2004; Coco and Murray, 2007; Castelle and Coco, 2012). The data shows that low power ($P_{sum} < 15\ x10^2 Kw/m$) or short storm durations do not have the capacity to initiate significant changes to sand bar morphologies (Figure 4a–d). While high-energy storms ($P_{sum} > 3.04\ x10^3 Kw/m$) that also have long durations have the potential to completely reset sand bar morphology, by reorganising locations and in such present lower than expected vorticity (Figure 4.4b–d; S8 in

Supplementary Figure S10). A similar finding was also found by Gallop et al. (2011) for changes in rip channel morphology at another embayed beach. Lower than expected vorticity during high-energy storms may relate to high storm migration rates (Figure 4.4d), that Holman et al. (2006) show can dominate the surf zone through rapid re-working of sand bar morphology. The high-energy storms and storm-clusters can cause considerable shifts in sand bar morphology and response patterns (Splinter et al., 2014), evident by the compounding responses of M and Γ seen in this study between S5 and S7 (Figure 4.4c; Figure 4.5; Figure 4.6b–c; Table 4.2; Table 4.3). This confirms what multiple studies have shown, that sand bar morphology relates to increases in seasonal wave energy (van de Lageweg et al., 2013), whereby the surf zone develops seaward during more energetic times (Splinter et al., 2011), sand bar width increase alongshore and rip channel width can decrease (Short, 1985; Gallop et al., 2011). Our data suggests that sand bars response patterns to storms (and especially storm clusters) are the result of sediment travelling though the rip channels and trough (Figure 4.5); for instance, this is shown by Γ_{ccw} at locations prograding sand bars where sand bars open or when meandering formations extend from antecedent bar formations (Figure 4.5a and b).

Seasonally, sand bars were more active in Austral autumn and winter (Figure 4.7), which correlates with the high-energy storm (Figure 4.3). Sand bar migration is energy driven (Castelle et al., 2007; Masselink et al., 2014) and this is evident in this study by below average migration rates seen in the summer months when no high-energy storms occurred (Table 4.1; Table 4.2). Fair-weather conditions in the Austral summer of 2015/16 show migration and vorticity were low, and that sandbars typically migrated north following storm induced southerly and offshore migration (Figure 4.3; Figure 4.6a–d). These fair-weather times are typically characterised by beaches recovery processes (Short, 1985), that see sand bars migrate onshore (Ojeda et al., 2011; Phillips et al., 2017) and see alongshore spacings and number of sandbars return to equilibrium through self-organisation feedback processes (Gallop et al., 2011; Castelle and Coco, 2012).

4.6 Conclusion

This paper presents a pattern recognition methodology to quantify sand bar migration and vorticity from video. We found that at the embayed beach study site of Bondi Beach, sand bar migration is controlled by alongshore gradients in wave energy due to headlands. The mean rate of sand bar migration here is $1m/day$ and mean vorticity is $1.8\ x10^{-2}s^{-1}$. During high-energy storms, the headland-shadowed northern zone of the beach experiences ~75 % of the migration and vorticity of the southern zone, which reached maxima of 22.3 $m/storm$ and 4.1 $x10^{-2}s^{-1}$. The general migration trend shows that when sand bars migrate south, they tend to move offshore with typical wave direction and when migrating north, they typically move onshore against typical wave direction. At Bondi Beach there are 4 key examples of sand bar response patterns to high-energy storms observed: opened sand bar-rip channel, meandering sand bar/trough, concentric sand bar, and sand bar curvature switching. These example patterns give insight into the storm induced transitions between sand bar morphologies and beach states at an embayed beach. The strongest Γ signals are most prevalent on sand bar and rip channel boundaries and at the centre rip channels. The two directions of vorticity motion represent changes in pixel intensities and show different processes, with counter-clockwise Γ_{ccw} at locations of rip channels that are replaced by sand bar, and clockwise Γ_{cw} at locations of sand bar that are replaced by rip channels. This study provided new insights into the morphological relationship of sand bars and surf zone dynamics with headlands, and a deeper understanding of how sand bars respond to storm events.

4.7 Acknowledgements

The Macquarie University (MQ) Research Training Programme (PhD Scholarship) and MQ Post Graduate Research Fund supported TEF. The Re-Entry Fellowship from Women in Science at the University of Sydney funded AV-C. Robert Brander from University of New South Wales (UNSW) established the camera. Wave data is from Manly Hydraulics Laboratory (NSW Dept of Planning, Industry and Environment). Thanks to Mitchell Harley from the Water Research

Laboratory (UNSW) for providing the storm Peak-Over-Threshold algorithm and to the Bondi Astra Retirement Village for hosting the camera.

4.8 References

Almar, R., Coco, G., Bryan, K.R., Huntley, D.A., Short, A.D., Senechal, N., 2008. Video observations of beach cusp morphodynamics. Marine Geology 254, 216-223.

Austin, M., Scott, T., Brown, J., Brown, J., MacMahan, J., Masselink, G., Russell, P., 2010. Temporal observations of rip current circulation on a macro-tidal beach. Continental Shelf Research 30, 1149-1165.

Birkemeier, W.A., Nicholls, R.J., Lee, G.-h., 1999. Storms, storm groups and nearshore morphologic change, Coastal Sediments. ASCE, pp. 1109-1122.

Blossier, B., Bryan, K.R., Daly, C.J., Winter, C., 2016. Nearshore sandbar rotation at single-barred embayed beaches. Journal of Geophysical Research: Oceans 121, 2286-2313.

Blossier, B., Bryan, K.R., Daly, C.J., Winter, C., 2017. Shore and bar cross-shore migration, rotation and breathing processes at an embayed beach. Journal of Geophysical Research: Earth Surface 122, 1745–1770.

Bruneau, N., Bonneton, P., Castelle, B., Pedreros, R., 2011. Modeling rip current circulations and vorticity in a high-energy mesotidal-macrotidal environment. Journal of Geophysical Research: Oceans 116.

Castelle, B., Bonneton, P., Dupuis, H., Sénéchal, N., 2007. Double bar beach dynamics on the high-energy meso-macrotidal French Aquitanian Coast: A review. Marine Geology 245, 141-159.

Castelle, B., Coco, G., 2012. The morphodynamics of rip channels on embayed beaches. Continental Shelf Research 43, 10-23.

Castelle, B., Coco, G., 2013. Surf zone flushing on embayed beaches. Geophysical Research Letters 40, 2206-2210.

Castelle, B., Scott, T., Brander, R.W., McCarroll, R.J., 2016. Rip current types, circulation and hazard. Earth-Science Reviews 163, 1-21.

Coco, G., Murray, A.B., 2007. Patterns in the sand: From forcing templates to self-organization. Geomorphology 91, 271-290.

Cooper, J.A.G., Jackson, D.W.T., Navas, F., McKenna, J., Malvarez, G., 2004. Identifying storm impacts on an embayed, high-energy coastline: examples from western Ireland. Marine Geology 210, 261-280.

Daly, C.J., Bryan, K.R., Winter, C., 2014. Wave energy distribution and morphological development in and around the shadow zone of an embayed beach. Coastal Engineering 93, 40-54.

Deigaard, R., Drønen, N., Fredsøe, J., Jensen, J.H., Jørgensen, M.P., 1999. A morphological stability analysis for a long straight barred coast. Coastal Engineering 36, 171-195.

Fellowes, T.E., Vila-Concejo, A., Gallop, S.L., 2019. Morphometric classification of swell-dominated embayed beaches. Marine Geology 411, 78-87.

Gallop, S.L., Bryan, K.R., Coco, G., 2009. Video Observations of Rip Currents on an Embayed Beach. Journal of Coastal Research, 49-53.

Gallop, S.L., Bryan, K.R., Coco, G., Stephens, S.A., 2011. Storm-driven changes in rip channel

patterns on an embayed beach. Geomorphology 127, 179-188.
Gallop, S.L., Bryan, K.R., Pitman, S.J., Ranasinghe, R., Sandwell, D.R., Harrison, S.R., 2018. Rip current circulation and surf zone retention on a double barred beach. Marine Geology 405, 12-22.
Harley, M.D., 2017. Coastal Storm Definition, In: Coastal Storms (Editors: Ciavola and Coco), Wiley, Chichester, United Kingdom, 1-19.
Harley, M.D., Turner, I.L., Short, A.D., 2015. New insights into embayed beach rotation: The importance of wave exposure and cross-shore processes. Journal of Geophysical Research: Earth Surface 120, 1470-1484.
Harley, M.D., Turner, I.L., Short, A.D., Ranasinghe, R., 2010. Interannual variability and controls of the Sydney wave climate. International Journal of Climatology 30, 1322-1335.
Harrison, S.R., Bryan, K.R., Mullarney, J.C., 2017. Observations of morphological change at an ebb-tidal delta. Marine Geology 385, 131-145.
Holman, R.A., Symonds, G., Thornton, E.B., Ranasinghe, R., 2006. Rip spacing and persistence on an embayed beach. Journal of Geophysical Research: Oceans 111, C01006.
Inman, D.L., Nordstrom, C.E., 1971. On the Tectonic and Morphologic Classification of Coasts. The Journal of Geology 79, 1-21. Jackson, D.W.T., Cooper, J.A.G., del Rio, L., 2005. Geological control of beach morphodynamic state. Marine Geology 216, 297-314.
Komar, P.D., 1998. Beach Processes and Sedimentation. Prentice Hall.
Kovesi, P., 2012. Phase Preserving Tone Mapping of Non-Photographic High Dynamic Range Images, 2012 International Conference on Digital Image Computing Techniques and Applications (DICTA), pp. 1-8.
Lippmann, T.C., Holman, R.A., 1989. Quantification of sand bar morphology: A video technique based on wave dissipation. Journal of Geophysical Research: Oceans 94, 995-1011.
Loureiro, C., Ferreira, Ó., Cooper, J.A.G., 2012a. Extreme erosion on high-energy embayed beaches: Influence of megarips and storm grouping. Geomorphology 139–140, 155-171.
Loureiro, C., Ferreira, Ó., Cooper, J.A.G., 2012b. Geologically constrained morphological variability and boundary effects on embayed beaches. Marine Geology 329–331, 1-15.
Loureiro, C., Ferreira, Ó., Cooper, J.A.G., 2013. Applicability of parametric beach morphodynamic state classification on embayed beaches. Marine Geology 346, 153-164.
MacMahan, J., Brown, J., Brown, J., Thornton, E., Reniers, A., Stanton, T., Henriquez, M., Gallagher, E., Morrison, J., Austin, M.J., Scott, T.M., Senechal, N., 2010. Mean Lagrangian flow behavior on an open coast rip-channeled beach: A new perspective. Marine Geology 268, 1-15.
MacMahan, J.H., Thornton, E.B., Reniers, A.J., 2006. Rip current review. Coastal Engineering 53, 191-208.
Masselink, G., Austin, M., Scott, T., Poate, T., Russell, P., 2014. Role of wave forcing, storms and NAO in outer bar dynamics on a high-energy, macro-tidal beach. Geomorphology 226, 76-93.
Masselink, G., Short, A.D., 1993. The effect of tide range on beach morphodynamics and morphology: A conceptual beach model. Journal of Coastal Research 9, 785-800.
McCarroll, R., Brander Rob, W., Scott, T., Castelle, B., 2018. Bathymetric Controls on Rotational Surfzone Currents. Journal of Geophysical Research: Earth Surface 0.
McCarroll, R.J., 2014. Field observations of embayed beaches: lagrangiancirculation,

morphodynamics and the rip current hazard. The University of New South Wales.
McCarroll, R.J., Brander, R.W., Turner, I.L., Power, H.E., Mortlock, T.R., 2014. Lagrangian observations of circulation on an embayed beach with headland rip currents. Marine Geology 355, 173-188.
McCarroll, R.J., Brander, R.W., Turner, I.L., Van Leeuwen, B., 2016. Shoreface storm morphodynamics and mega-rip evolution at an embayed beach: Bondi Beach, NSW, Australia. Continental Shelf Research 116, 74-88.
Mortlock, T.R., Goodwin, I.D., 2015. Directional wave climate and power variability along the Southeast Australian shelf. Continental Shelf Research 98, 36-53.
Ojeda, E., Guillén, J., Ribas, F., 2011. Dynamics of single-barred embayed beaches. Marine Geology 280, 76-90.
Orzech, M.D., Reniers, A.J.H.M., Thornton, E.B., MacMahan, J.H., 2011. Megacusps on rip channel bathymetry: Observations and modeling. Coastal Engineering 58, 890-907.
Phillips, M.S., Harley, M.D., Turner, I.L., Splinter, K.D., Cox, R.J., 2017. Shoreline recovery on wave-dominated sandy coastlines: the role of sandbar morphodynamics and nearshore wave parameters. Marine Geology 385, 146-159.
Pitman, S., Gallop, S.L., Haigh, I.D., Mahmoodi, S., Masselink, G., Ranasinghe, R., 2016a. Synthetic Imagery for the Automated Detection of Rip Currents. Journal of Coastal Research, 912-916.
Pitman, S., Gallop, S.L., Haigh, I.D., Masselink, G., Ranasinghe, R., 2016b. Wave breaking patterns control rip current flow regimes and surfzone retention. Marine Geology 382, 176-190.
Reniers, A.J.H.M., MacMahan, J.H., Beron-Vera, F.J., Olascoaga, M.J., 2010. Rip-current pulses tied to Lagrangian coherent structures. Geophysical Research Letters 37.
Reniers, A.J.H.M., Roelvink, J.A., Thornton, E.B., 2004. Morphodynamic modeling of an embayed beach under wave group forcing. Journal of Geophysical Research: Oceans 109, n/a-n/a.
Scott, T., Masselink, G., Russell, P., 2011. Morphodynamic characteristics and classification of beaches in England and Wales. Marine Geology 286, 1-20.
Shand, T., Goodwin, I., Mole, M., Carley, J., Browning, S., Coghlan, I., Harley, M., Preston, W., 2010. NSW coastal inundation hazard study: coastal storms and extreme waves, Water Research Laboratory Technical Report, pp. 1-45.
Short, A., Trenaman, N., 1992. Wave climate of the Sydney region, an energetic and highly variable ocean wave regime. Marine and freshwater research 43, 765-791.
Short, A.D., 1985. Rip-current type, spacing and persistence, Narrabeen Beach, Australia. Marine Geology 65, 47-71.
Short, A.D., 2007. Beaches of the New South Wales coast: a guide to their nature, characteristics, surf and safety. Sydney University Press.
Smith, R.K., Bryan, K.R., 2007. Monitoring Beach Face Volume with a Combination of Intermittent Profiling and Video Imagery. Journal of Coastal Research, 892-898.
Splinter, K.D., Carley, J.T., Golshani, A., Tomlinson, R., 2014. A relationship to describe the cumulative impact of storm clusters on beach erosion. Coastal Engineering 83, 49-55.
Splinter, K.D., Holman, R.A., Plant, N.G., 2011. A behavior-oriented dynamic model for sandbar migration and 2DH evolution. Journal of Geophysical Research: Oceans 116, n/a-n/a.
Taborda, R., Silva, A., 2012. COSMOS: A lightweight coastal video monitoring system.

Computers Geosciences 49, 248-255.
Valiente, N.G., Masselink, G., Scott, T., Conley, D., 2017. Depth of Closure Along an Embayed, Macro-Tidal and Exposed Coast: A Multi-Criteria Approach. Coast. Dyn, 1211-1222.
van de Lageweg, W.I., Bryan, K.R., Coco, G., Ruessink, B.G., 2013. Observations of shoreline–sandbar coupling on an embayed beach. Marine Geology 344, 101-114.
van Enckevort, I.M.J., Ruessink, B.G., 2003. Video observations of nearshore bar behaviour. Part 2: alongshore non-uniform variability. Continental Shelf Research 23, 513-532.
van Enckevort, I.M.J., Ruessink, B.G., Coco, G., Suzuki, K., Turner, I.L., Plant, N.G., Holman, R.A., 2004. Observations of nearshore crescentic sandbars. Journal of Geophysical Research: Oceans 109, n/a-n/a.
Wang, J.Y.A., Adelson, E.H., 1994. Representing moving images with layers. IEEE Transactions on Image Processing 3, 625-638.
Wright, L.D., Short, A.D., 1984. Morphodynamic variability of surf zones and beaches: A synthesis. Marine Geology 56, 93-118.

5

Final Considerations

5.1 Thesis aim

This thesis is a multi-scale investigation of embayed beach morphology and morphodynamics over spatial scales of metres to kilometres and temporal scales of days to millennia. This chapter summarises the thesis findings that are presented in Chapters 2 to 4, in context with the existing literature, and states how this body of work extends embayed beach research and coastal science. This chapter is structured to answer the research questions and every one of the individual objectives from Chapter 1; the final part of this chapter explores the significance of the research.

The overarching thesis aim is:

Classifying and understanding how headlands influence embayed beach morphology and storm response

The following research questions are answered by a series of objectives, with a summary of how these are met below.

5.2 Research Questions Answered

Research Question 1: Is it possible to describe different types of embayed beaches by their geomorphological setting using morphometrics collected from open-access imagery? YES.

Chapter 2 provides a powerful tool that, using simple embayed beach morphometrics, provides a quantitative classification of embayed beaches according to their degree of embaymentisation, that determines the level of headland control.

Objective 1.1 Develop a simple empirical relationship to classify the degree of embaymentisation (level of influence) from headlands have on embayed beach morphodynamics.

Chapter 2 proposes a simple new quantitative classification of swell-dominated embayed beaches. This classification is based on the degree of embaymentisation, representing the

varying influences of embayment and headland geometry on beach morphodynamics and was developed using extensive analyses of 168 embayed beaches in 6 regions globally (Table 2.1). For each one of those beaches, 7 morphometric parameters were measured using open-access imagery. Chapter 2 proposes a new empirical relationship defined as the "embayment morphometric parameter" (γ_e) that is a function of embayment indentation (a) and embayment area (A_e) (Eq. 2.4; Figure 2.2). Four classes of embayed beach were defined with k-means cluster analysis, ranging from Class 1 (least embayed) to Class 4 (most embayed) (Figure 2.7).

Objective 1.2 Develop a simple classification of embayed beach headland orientations that is universally applicable to embayed beaches.

Embayed beaches have a range of headland orientations (angle) relative to the beach aspect. Chapter 2 presents a classification of embayed beach headland orientations, with 6 headland orientation types (H1 – H6) (Figure 2.5a), ranging from two acutely oriented headlands (H1) to two obtusely oriented headlands (H6) (Figure 2.5b). Chapter 2 shows the results for all 168 beaches in the 6 regions of the world and shows that H6 is the most common orientation (Figure 2.5f). Chapter 2 also demonstrates that the amount of headland shadowing (protection) as a proportion of beach length increases with the embayed beach class defined in Objective 1.1 (Figure 2.5f).

Objective 1.3 Compare these two new classifications with previous classifications, apply them to globally representative regions and at a regional level to explore relationships in embayed beach morphometrics.

The two new classifications (Objective 1.1 and Objective 1.2) represent an improvement on previous classifications that were based on idealistic embayments assuming headlands with the same length, that are symmetrical and perpendicular to the shoreline (Figure 2.8). However, the reality is that embayed beaches have irregular embayment shapes and areas, a range of coastal indentations and headland orientations that are commonly asymmetrical (Figure 2.9). The extensive analysis in Chapter 2 (Objective 1.1) shows that Class 2 embayed beaches and the H6 headland type are the most common because most embayed beaches are either located at the

mouths of river or estuarine systems or are pockets of coastal indentation (Figure 2.5f).

Research Question 2: Does the degree of embaymentisation and headland orientations impact embayed beach storm response and post-storm recovery rate? YES.

Chapter 3 provides a new method that quantifies the impacts of the degree of embaymentisation, headlands and the alongshore gradients on morphodynamics during storm and fair-weather waves.

Objective 2.1 Compare how headlands and degree of embayment influence morphological response to storm conditions.

Chapter 3 presents the morphological responses of 9 beaches from the 4 different classes of embayed beach (C1–C4) and 6 headland types to fair-weather conditions in southeast Australia and compares this with the literature (Figure 3.7; Figure 3.10). The mean storm response in terms of subaerial volume loss to 8 high-energy storms (2015–2019) from 3 main wave directions (E-NE, SE-SSE and S) vary with the degree of beach embayment as defined by the 4 classes in Objective 1.2. The least embayed beaches had the largest subaerial beach volume losses (Class 1; up to -25 m^3/m) and vice versa for the most embayed beaches (Class 4; up to 0.5 m^3/m) (Figure 3.9). A case study surrounding the most erosive storm in this study (June 2016) showed mean volume losses of -73 m^3/m from the subaerial beach. Moreover, storm responses from this study combined with 13 additional beaches from the literature (elsewhere in southeast Australia, UK and Portugal) show that embayed beach storm response is regionally and site-specific, where storm volume loss is the lowest for Class 1 (up to 43 m^3/m) and increased towards the most embayed beaches (Class 4; up to 110 m^3/m) (Figure 3.10; Table 3.3).

Objective 2.2 Determine how the degree of embaymentisation impacts post-storm recovery of the subaerial beach.

Chapter 3 demonstrates that the post storm recovery rate of the subaerial beach is dictated by the degree of embaymentisation. In southeast Australia, the mean subaerial beach recovery rate is 0.2 $m^3/m/day$ for low to moderately embayed beaches (Class 1 to Class 3), and 0.05

$m^3/m/day$ for highly embayed beaches (Class 4) (Figure 3.9). Recovery after the notable June 2016 storm took up to 3 years for the least embayed beaches (Class 1 and Class 2), while the most embayed beaches studied (Class 3) recovered in 6–12 months (no data for this storm for Class 4). Beach aspect relative to modal wave direction and the depth indentation of the embayment were the main factors in recovery rates of embayed beach. Recovery rates after the storms are consistent with the degree embaymentisation (Class) for the beaches across southeast Australia, the UK and Portugal (total n = 22). Storm responses show similar trends, with recovery of 0.22 $m^3/m/day$ for low to moderately embayed beaches (Class 1 to Class 3) and 0.08 $m^3/m/day$ for highly embayed beaches (Class 4) (Figure 3.9; Table 3.3). Chapter 3 proposes the existence of an embaymentisation threshold, where more embayed beaches (Class 4) are slowest to recover and most vulnerable to storm impacts.

Objective 2.3 Assess how headlands impacts alongshore morphodynamics in protected (headland shadowed) and exposed zones of embayed beaches.

Chapter 3 presents a new trigonometry-based approach to define the shadow edge (X_{se}) that represents the alongshore boundary between the exposed and protected (headland shadowed) zones of embayed beaches (Figure 3.2). The X_{se} approach can be applied with minimal effort to any beach combining headland geometry collected from open-access satellite imagery with storm wave direction. This is applied to 8 high-energy storms at 9 embayed beaches in southeast Australia. The X_{se} shifted alongshore based on the 3 main storm wave directions (E-NE, SE-SSE and S). The morphological responses to storms where quantified in both the exposed and protected zones, with mean subaerial beach volume losses 7 times higher (43 m^3/m) in exposed zones compared to the protected zones (-6 m^3/m) (Figure 3.6a). This method provides insight into headland impacted morphodynamics and the presence of multiple beach states that are commonly observed alongshore.

Research Question 3: Can we provide a new approach to quantify sand bar and rip channel responses along embayed beaches to storms from video? YES.

Chapter 4 proposes a new method to quantify sand bar migration and defines sand bar vorticity to show impacts of headlands shadowing on alongshore sand bar morphodynamics.

Objective 3.1 Develop a semi-automated method to measure patterns of sand bar dynamics from video imagery.

Chapter 4 presents a semi-automated pattern recognition methodology to quantify 6 years (2012–2016) of sand bar migration and sand bar vorticity from daily video imagery. This methodology is used to investigate sand bar responses over storm-scales and builds on standard video image techniques that identify nearshore features that are characterised by high pixel intensity of waves breaking over waves (Figure 4.2). The new approach involves modifying previously used methods for measuring rip current flow vorticity, by substituting current velocities with quantified alongshore and cross-shore migration rates (m/day) (Eq. 4.6). Results from 11 high-energy storms (2012–2018) show that sand bar migration increased with storm duration and storm power, while sand bar vorticity diminished under these conditions (Figure 4.4). The two directions of sand bar vorticity represent pixel intensity changes, with counter-clockwise vorticity (Γ_{ccw}) at locations where rip channels were replaced by sand bars, and clockwise (Γ_{cw}) at locations where sand bars were replaced by rip channels. Four key examples of sand bar response patterns to the high-energy storms observed at Bondi Beach include: opened sand bar-rip channel, meandering sand bar/trough, concentric sand bar, and sand bar curvature switching. These patterns and sand bar vorticity provide insights into the transition and rotational components of sand bar morphology on an embayed beach (Figure 4.5).

Objective 3.2 Provide insights into sand bar morphodynamics on an embayed beach with asymmetrical headlands and an alongshore gradient in waves.

Chapter 4 shows that sand bar migration is driven by an alongshore gradient wave energy from

the asymmetrical headland orientations at Bondi Beach (Figure 4.1c; Figure 4.6b–c). Sand bar dynamics are seasonal and most active in Austral Autumn and Winter (Figure 4.7). During fair-weather conditions, mean sand bar migration is ~1 m/day in alongshore and cross-shore directions and vorticity (both directions) is 1.8 $x10^{-2}s^{-1}$. During high-energy storms, the headland-shadowed zone of the beach experienced ~75 % of the migration and vorticity of the exposed zone, which reached maximum migration of 22.3 m/storm and vorticity of 4.1 $x10^{-2}s^{-1}$ (Figure 4.6b–f; Table 4.2; Table 4.3). Chapter 4 shows a general migration trend showed that when sand bars migrated towards the exposed headland, they tended to also move offshore with typical wave direction, and when migrating towards the protected headland, they typically move onshore against typical wave direction (Figure 4.6d).

5.3 Significance and contribution to coastal science

This thesis is a multi-scale approach that analyses a large number of embayed beaches, including a global assessment across 6 embayed regions that feature heavily in the literature (n = 168; Chapters 2–4) that is combined with more detailed site-specific studies also presented in the same chapters. The chapters link through common themes, highlighting the geological impact and headland controls on embayed beach morphodynamics (Loureiro et al., 2012; Castelle and Coco, 2013; Daly et al., 2014; George et al., 2015) and are applied across multiple spatial-temporal scales, from millennial (Chapter 3) to seasonal-yearly (Chapter 3–4); and spatial that encompass embayment morphology (Chapter 2) to beach morphology (Chapter 2–3) and sand bar morphology (Chapter 4) (Figure 5.1). Chapter 2 presents a classification framework of embayed beaches globally. Chapter 3 shows how beach scales morphology and storm and fair-weather responses vary based on these geometries and the degree of embaymentisation. Finally, Chapter 4 addresses headlands shadowed and alongshore sand bar morphodynamics and modifies traditional flow mechanics equations to define and quantify sand bar vorticity.

Many studies on embayed beaches before this thesis were based on individual beach sites or a low number of local or regional areas (e.g., southeast Australia, southwest United Kingdom, southeast Brazil, northwest New Zealand; Table 2.1), and therefore could not account for all the

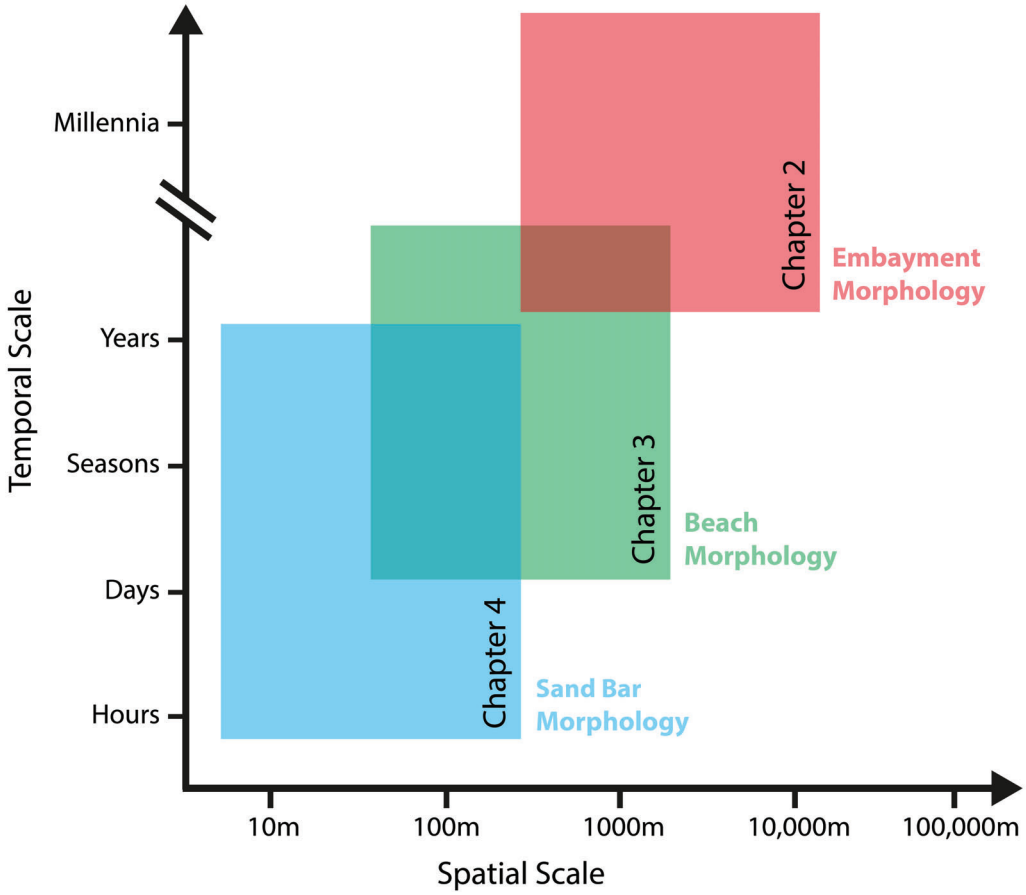

Figure 5.1: The spatial and temporal scales for each research chapter (Chapter 2–4), showing the main themes and overlaps. Figure is based on the idea of the coastal evolution model from Cowell and Thom (1997).

inherent geological variability that can be considered in a global study. Chapter 2 demonstrates that a comprehensive assessment or classification of embayed beaches must consider the diversity in embayment and headland geometries. For instance, previous studies (Scott et al., 2011; Bryan et al., 2013) have shown that adjacent beaches could respond in different ways due to differing wave exposures; this thesis assesses these differences through quantifying the wave shadowing effect of the headlands and the degree of embaymentisation in Chapters 2 to 4. This thesis shows how classifying embayed beaches on a global scale has become feasible with the advent of technical developments such as open-access imagery (e.g., Google Earth), remote sensing video cameras and RTK–GNSS surveying. These have allowed for more in situ measurements and more beaches in remote corners of the world to be studied with minimal effort.

The embayed beach classification (γ_e) presented in Chapter 2 and published in Marine Geology (Fellowes et al., 2019), categorises all embayed beaches into 4 classes (Class 1-Class 4) based on the degree of embayment from an empirical ratio of embayment area (A_e) and coastal indentation (a). The γ_e classification allows for inclusion to a range of embayment shapes and areas, and headland orientations and geometries found globally. The classification builds on works on the static beach and embayment planform and headland refraction of Hsu and Evans (1989) that characterised embayment boundaries and headland–beach responses as well as the embayed beach; and builds on the nearshore circulation model (δ') of Short and Masselink (1999) proposed the circulation of idealistic embayments that assumed headlands were perpendicular to the shoreline and were the same length offshore. However, McCarroll et al. (2016) showed that headland asymmetry could control alongshore morphodynamics. These works prompted the ideas of categorising atypically headland orientation types (H1–H6) in Chapter 2 and the X_{se} in Chapter 3. The presented e classification (Class 1–Class 4) in Chapter 2 and X_{se} in Chapter 3 are centred around principals of using open-access data for universal application to any embayed beach globally and better determines the embayment impacts.

This thesis used a combination of current and state-of-the-art methodologies and developed three simple tools to determine headland and embayment impacts and the degree of embaymentisation across multiple scales. New methods in Chapters 2 to 4 focus on the geological processes that commonly span different spatial-temporal scales, and this led to a comprehensive study of embayed beaches through:

- A new classification (Class 1-Class 4) that builds on previous works with a global morphometric assessment and categorisation of headland orientations types (H1–H6) (Chapter 2; Figure 2.5; Figure 2.7).
- A new trigonometry-based approach to define the headland shadow edge (X_{se}) that quantifies alongshore morphodynamics and highlights headland shadow processes (Chapter 3; Figure 3.2; Figure 3.6a).

- A new video image technique to quantify daily sand bar migration that builds on established camera image methods and defines sand bar vorticity and shifts in sand bar morphology on storms-scales (Chapter 4; Figure 4.5a–d; Figure 4.6b–c, e).

These tools are simple approaches that require limited data, are highly repeatable and show how the thesis' approach is at the forefront of embayed beach research, including for example, the use of open-access imagery in Chapter 2 and 3, global wave model data in Chapter 2, RTK–GNSS surveys in Chapter 3 and video camera imagery in Chapter 4. This is evident at Bondi beach (Australia; Figure 4.1c), which is included across Chapters 2 to 4. Bondi beach is a Class 2 beach, which is the most common class (representing 43 % of embayed beaches globally; Table 2.2). This beach was subjected to the shadow edge (X_{se}) analysis with alongshore storm response and recovery rates quantified and characterised to 8 high-energy storms (Chapter 3); and was the location of the video camera that captured 6 years (2012–2018) of daily images to quantify sand bar morphological changes (Chapter 4). Understanding multi-scale processes on embayed beaches is fundamental in any comprehensive beach study (Figure 5.1). Findings from this thesis (Chapter 2–4) provide greater understanding and give insight into embayed beach dynamics on a global scale.

5.4 Future Directions

This thesis answers a number of fundamental research questions about embayed beaches, however, as it is always the case with research, it has also triggered other questions that remain unanswered and should be the subject of further investigation. The following unanswered questions are an example of future directions of research that will be crucial for completing the understanding of the morphodynamics of embayed beaches.

5.4.1. *How does the tidal ranges impact alongshore gradients in subaerial volume losses and recovery rates on embayed beaches to high-energy storms?* This question could use the new classification (Chapter 2) and the X_{se} method (Chapter 3) to show if the interaction of different tidal range (micro vs. macro) with long duration storms or storm-clusters influences the erosion

risk to beaches. For example, the June 2016 storm case study (Chapter 3) occurred at the same time as a superelevated water level and caused a mean subaerial volume (76 m^3/m) three times the average of other storms (Figure 3.7). Furthermore, this may present reasons for the higher erosion in Cornwall, UK than southeast Australia between comparable Class 4 beaches that have total embayment control (Chapter 3; Figure 3.9; Figure 3.10). This question is important as tidal conditions vary globally, and a comprehensive understanding of tides and storm impact to embayed beaches is important to coastal science.

5.4.2. *How does sand bar vorticity control shifts in morphodynamic beach state, storm erosion?* This question could provide a way of determining shifts between beach states that do not follow the previous morphodynamic frameworks. Sand bar vorticity may present a mode of beach recovery when sand bar morphology transitions (down-state) after storms (Chapter 4). This question could also be a way of quantifying the self-organisation of sand bars and suggest why embayed beaches do not typically reset (or become alongshore uniform) after high-energy storms. Furthermore, this question could also be useful for open (non-embayed) beaches. In addition, better understanding of changes in sand bar morphology and vorticity is paramount for the safety of beach goes, coastal management and vulnerability assessments.

5.4.3. *How does sediment grain size and mixing affect the morphodynamics of embayed beaches?* This thesis focuses on embayed beaches that are purely sand, but embayed beaches can also exist of other sediments such as gravel, boulders, and mixed sediments. It would be interesting to see if the methods and approaches in this thesis (Chapter 2–4) could be applicable to embayed beaches with other types of sediment. This could be integrated into the morphometric assessment of beaches by looking at other embayed regions (Chapter 2) by providing regional understanding in locations that may be inaccessible. This would ultimately be important for understanding non-linear embayed beach morphodynamics on a global scale.

5.5 References

Bryan, K.R., Foster, R., MacDonald, I., 2013. Beach Rotation at Two Adjacent Headland-Enclosed Beaches. Journal of Coastal Research, 2095-2100.

Castelle, B., Coco, G., 2013. Surf zone flushing on embayed beaches. Geophysical Research Letters 40, 2206-2210.

Cowell, P.J., Thom, B.G., 1997. Morphodynamics of coastal evolution, in: Carter, R.W.G., Woodroffe, C.D. (Eds.), Coastal Evolution: Late Quaternary Shoreline Morphodynamics. Cambridge University Press, United Kingdom and New York, pp. 33-86.

Daly, C.J., Bryan, K.R., Winter, C., 2014. Wave energy distribution and morphological development in and around the shadow zone of an embayed beach. Coastal Engineering 93, 40-54.

Fellowes, T.E., Vila-Concejo, A., Gallop, S.L., 2019. Morphometric classification of swell-dominated embayed beaches. Marine Geology 411, 78-87.

George, D.A., Largier, J.L., Storlazzi, C.D., Barnard, P.L., 2015. Classification of rocky headlands in California with relevance to littoral cell boundary delineation. Marine Geology 369, 137-152.

Hsu, J., Evans, C., 1989. Parabolic Bay Shapes and Applications. Proceedings of the Institution of Civil Engineers 87, 557-570.

Loureiro, C., Ferreira, Ó., Cooper, J.A.G., 2012. Geologically constrained morphological variability and boundary effects on embayed beaches. Marine Geology 329–331, 1-15.

McCarroll, R.J., Brander, R.W., Turner, I.L., Van Leeuwen, B., 2016. Shoreface storm morphodynamics and mega-rip evolution at an embayed beach: Bondi Beach, NSW, Australia. Continental Shelf Research 116, 74-88.

Scott, T., Masselink, G., Russell, P., 2011. Morphodynamic characteristics and classification of beaches in England and Wales. Marine Geology 286, 1-20.

Short, A.D., Masselink, G., 1999. Embayed and structurally controlled embayed beaches, Handbook of beach and shoreface morphodynamics. Wiley, Chichester, pp. 230-250.

6

Supplementary Information

6.1 Supplementary Chapter 2

Datasets related to Chapter 2 can be found at http://dx.doi.org/10.17632/c5bxpgbdr2.1, an open-source online data repository hosted at Mendeley Data (Fellowes et al., 2018).

6.2 Supplementary Chapter 3

6.2.1 Supplementary Tables

Table S1: Storm statistics for Chapter 3 defined as events with H_s > 3 m.

Start Date	**End Date**	**Duration (hrs)**	**Mean H_s (m)**	**Mean H_{max} (m)**	**Max H_{max} (m)**	**Mean T_z (s)**	**Mean T_p (s)**	**Mean W_{dir} (deg)**
2015/12/12	2015/12/12	7	3.22	5.64	6.52	8.19	10.85	173.00
2015/12/27	2015/12/27	6	3.12	5.25	6.04	6.58	8.85	182.71
2016/01/04	2016/01/08	85	3.28	5.76	8.00	6.88	9.86	143.87
2016/01/14	2016/01/15	21	3.58	6.35	7.77	7.01	9.89	180.05
2016/02/04	2016/02/05	30	3.47	6.12	8.16	6.67	9.33	173.97
2016/02/17	2016/02/18	28	3.26	5.67	7.38	9.52	14.43	161.90
2016/03/19	2016/03/21	41	3.71	6.42	8.64	8.75	13.08	172.65
2016/03/31	2016/03/31	10	3.42	5.75	6.62	8.30	10.81	166.27
2016/04/23	2016/04/23	13	3.40	5.64	6.26	6.69	9.54	172.75
2016/05/25	2016/05/25	6	3.17	5.03	5.31	10.04	13.31	152.00
2016/05/28	2016/05/28	6	3.15	5.17	6.16	8.95	12.49	173.50
2016/06/04	2016/06/07	75	4.24	7.18	12.01	9.10	13.98	118.67
2016/06/25	2016/06/25	9	3.08	5.23	5.43	7.81	11.24	171.00
2016/07/07	2016/07/08	47	3.54	5.94	7.20	7.56	10.98	160.25
2016/07/29	2016/07/29	12	3.24	5.14	6.81	10.10	13.71	171.91
2016/08/02	2016/08/05	57	3.60	6.18	10.40	7.11	10.07	161.65
2016/09/23	2016/09/23	12	3.10	5.07	5.52	6.84	9.42	188.80
2016/10/13	2016/10/13	13	3.59	6.28	7.59	7.84	10.49	181.07
2016/10/22	2016/10/25	66	3.66	6.26	8.01	8.66	12.27	165.66

2016/11/14	2016/11/15	11	3.46	6.35	8.34	7.41	10.63	179.75
2016/11/24	2016/11/24	10	3.30	5.78	7.58	7.92	10.56	175.55
2016/12/09	2016/12/10	11	3.21	5.68	7.83	8.72	12.01	173.89
2017/01/21	2017/01/21	6	3.66	6.31	7.11	7.59	10.03	178.71
2017/02/14	2017/02/14	8	3.24	5.88	6.62	7.64	10.46	168.33
2017/03/04	2017/03/11	168	3.47	6.08	8.61	7.44	11.18	146.20
2017/03/17	2017/03/19	45	3.45	6.20	8.07	6.76	9.22	151.95
2017/03/30	2017/03/31	14	3.56	6.32	7.57	6.66	10.32	177.33
2017/04/11	2017/04/12	26	4.07	7.12	9.53	8.07	11.95	177.96
2017/04/27	2017/04/28	20	3.61	6.50	8.05	7.53	11.24	173.64
2017/05/08	2017/05/09	17	3.20	5.32	6.63	8.25	12.70	174.88
2017/05/16	2017/05/16	7	3.06	5.34	5.58	7.21	9.59	176.00
2017/05/31	2017/06/01	30	3.19	5.59	6.26	6.53	8.79	182.86
2017/06/07	2017/06/07	14	3.62	6.29	8.18	6.92	9.65	184.00
2017/06/30	2017/07/01	16	3.21	5.46	6.66	7.70	11.89	165.69
2017/07/20	2017/07/23	72	3.29	5.66	6.41	8.53	11.76	167.25
2017/08/01	2017/08/02	22	3.31	5.80	6.74	7.86	10.39	161.93
2017/08/19	2017/08/20	38	4.27	7.35	10.08	8.42	12.30	166.28
2017/08/24	2017/08/25	11	3.14	5.26	5.99	6.81	9.27	181.50
2017/08/28	2017/09/01	100	4.16	7.08	10.39	8.00	10.97	170.76
2017/09/09	2017/09/10	27	3.61	6.23	7.59	9.25	13.52	160.25
2017/10/07	2017/10/07	13	3.08	5.38	5.91	7.08	10.47	184.50
2017/10/31	2017/11/02	39	3.91	6.72	8.44	8.96	12.00	169.70
2017/11/07	2017/11/07	9	3.47	6.06	7.58	7.89	11.18	161.78
2017/12/04	2017/12/06	46	3.22	5.79	7.10	7.26	10.85	166.88
2018/01/14	2018/01/17	82	3.71	6.55	9.62	7.26	10.65	173.74
2018/01/31	2018/02/01	32	3.50	6.16	7.43	7.25	10.39	174.00
2018/02/20	2018/02/20	10	3.29	6.14	7.29	6.66	8.47	167.33
2018/02/25	2018/02/26	18	3.28	5.65	6.39	6.60	8.83	145.78

2018/03/20	2018/03/23	54	3.48	6.15	8.21	6.98	9.74	140.76
2018/05/12	2018/05/14	55	3.52	6.04	6.80	7.11	10.67	172.43
2018/05/31	2018/06/03	69	4.18	7.20	9.98	7.58	11.52	171.02
2018/06/18	2018/06/20	48	3.81	6.74	9.22	7.30	10.73	174.73
2018/07/09	2018/07/10	30	3.84	6.67	8.65	9.16	12.85	163.84
2018/07/14	2018/07/14	20	3.79	6.65	7.69	8.89	11.12	169.43
2018/08/19	2018/08/20	26	3.53	6.08	8.66	8.00	11.81	173.04
2018/08/27	2018/08/27	11	3.65	6.47	7.50	7.17	9.39	180.92
2018/08/29	2018/08/30	23	3.95	6.72	9.51	9.58	13.77	160.63
2018/10/05	2018/10/07	67	3.23	5.60	6.75	6.60	8.76	157.46
2018/10/10	2018/10/10	6	3.16	5.93	6.81	6.77	9.21	164.14
2018/10/15	2018/10/16	7	3.01	5.93	6.59	7.20	10.55	88.00
2018/11/28	2018/11/30	37	3.48	6.15	9.25	6.73	9.05	161.41
2019/02/23	2019/02/25	31	3.17	5.53	6.96	7.17	9.89	158.88
2019/03/07	2019/03/07	9	3.38	5.80	7.41	7.66	10.75	170.50
2019/05/06	2019/05/07	35	3.18	5.52	7.06	8.44	10.92	162.09
2019/05/11	2019/05/11	6	3.19	5.72	6.53	7.59	12.82	177.67
2019/05/31	2019/06/02	32	3.83	6.60	8.49	8.39	12.23	173.13
2019/06/04	2019/06/07	70	4.01	7.09	12.54	7.81	11.15	162.39

6.2.2 Supplementary Figures

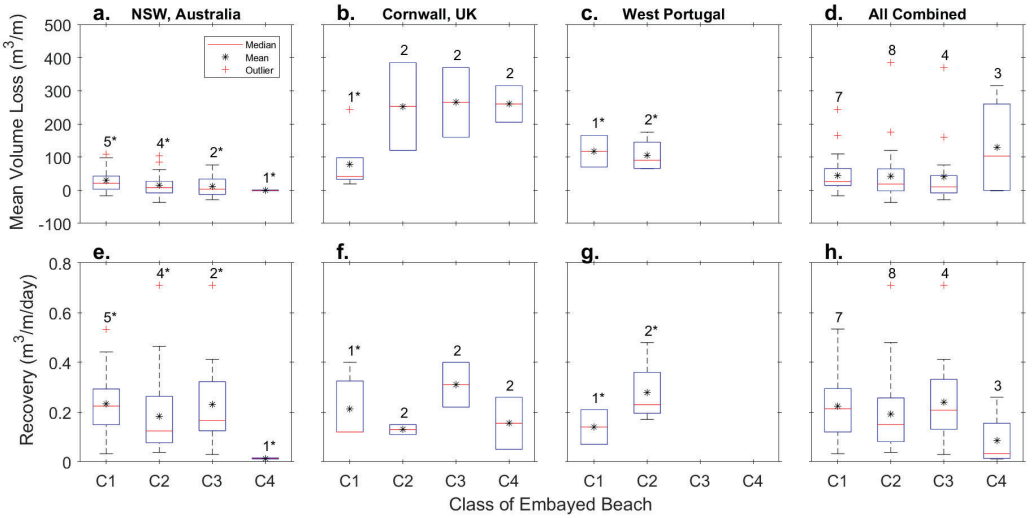

Figure S1: Beach mean volume loss by class (top) and recovery rate by class (bottom) with number of beaches stated above and '*' denoting multiple storms included in calculations. Data is combined from this study and multiple sources listed in Table 3. (a and e) NSW, Australia (this study plus 3, n = 12), (b and f) Cornwall, UK (n = 8), (c and g) Central Portugal (n = 3), and all regions combined (n = 22).

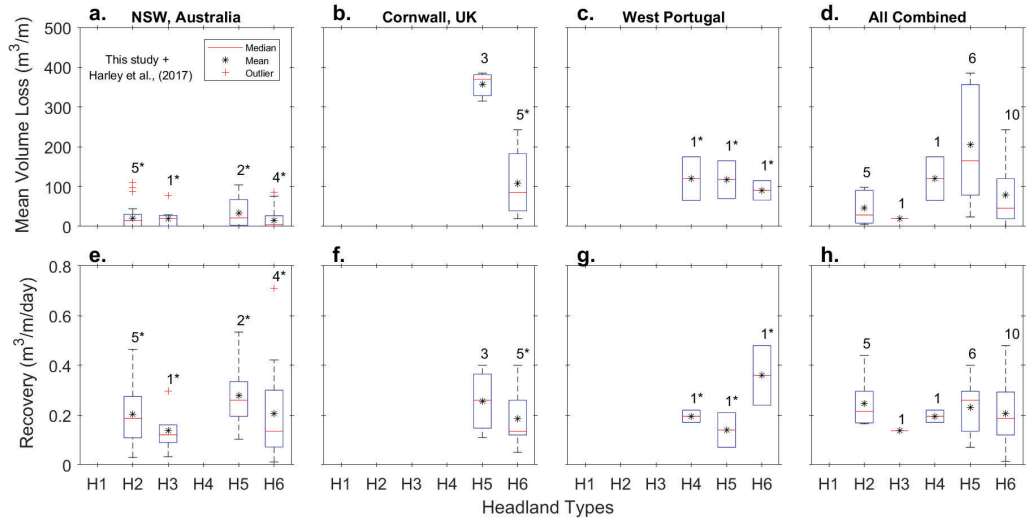

Figure S2: Beach mean volume loss by headland type (top) and recovery rate by headland type (bottom) with number of beaches stated above and '*' denoting multiple storms included in calculations. Data is combined from this study and multiple sources listed in Table 3. (a and e) NSW, Australia (this study plus 3, n = 12), (b and f) Cornwall, UK (n = 8), (c and g) Central Portugal (n = 3), and all regions combined (n = 22).

6.3 Supplementary Chapter 4

6.3.1 Supplementary Tables

Table S2: Sand bar morphodynamics from the high-energy storms with descriptions of sand bar migration M and rates, and vorticity Γ in counter-clockwise Γ_{ccw} and clockwise Γ_{cw} directions measured in beach length X_d from north with storm clusters labelled (SC1/SC2). Typical patterns detected including Opened sand bar/rip channel (OSB), Sand bar curvature switching (SCS), Concentric sand bar (CSB) and meandering sand bar/tough (MSB) with locations in beach length X_d from north.

	Sand bar Migration, M	**Sand bar Vorticity, Γ**
S1	Pre-storm, TBR in southern and meandering troughs in the northern zone. Post-storm there is a divergence point (X_d = 500 m) with northern zone bars change orientation (north 45°), infilled trough and TBR oriented southerly 45° (X_d = 100, 250, 450 m) and southern zone bars RBB and oriented north 45° (X_d = 550, 725, 800 m).	Weak Γ_{ccw} and Γ_{cw}, especially in the northern zone. Southern zone has a large complex concentric rip that has Γ_{ccw} on the leading edges of new sand bars (X_d = 450, 550, 700 m). Γ_{cw} is evident in the deeper zones where rip channels form and where they open seaward (X_d = 100, 275, 475, 550, 750 m).
S2	Pre-storm, northern zone was LTT and the southern zone was TBR. Post-storm the northern zone was LBT and the southern was BBB. There was general offshore migration and shoreline infilling (X_d = 350–500 m), a trough in the central beach (X_d = 150–350, 450–800 m) that reorganised rips, rip deepening in the south and south headland rip development (X_d = 675 m).	Mild vorticity overall, Γ_{ccw} was focused on the edges of sand bars and rips in the southern zone (X_d = 150–250, 400–600, 675, 825 m) and Γ_{cw} was in locations where deepening of channels in the at newly formed rips (X_d = 150, 500, 725 m) and in points offshore where deepening occurred from possible erosion (X_d = 225, 550 m).
S3	Start of cluster. Pre-storm northern LTT and southern zone RBT/LBT. Post-storm TBR in northern (X_d = 175 m) and southern zone seaward extension, RBB spiral concentric bars (X_d = 275–450 m) and meandering TBR (X_d = 575, 700 m).	Vorticity high overall and shows complex patterns. The strongest Γ_{ccw} edges of new and prograding bars (X_d = 75, 150–250, 350–400, 500–600, 650, 725 m). the strong Γ_{cw} processes where along the troughs (X_d = 50–200, 550, >650 m) and widening rip channels (X_d = 150, 300–500, 550, 650, 700 m).

S4	End of cluster. Pre-storm based off previous storm with LTT/TBR in northern and in southern RBB (X_d = 275–425 m) and TBR (X_d = 575, 700, 850 m). Post-storm northern is same, southern zone more RBB with lateral extension of spiral concentric bars (X_d = 275–600 m) and same TBR at south (X_d = 700, 850 m).	Vorticity is high and concentrated in southern zone. The Γ_{ccw} is on leading edges and locations of offshore sand bar progradation (X_d = 50, 200–300, 350–800 m) and along infilled nearshore tough (X_d = 200–300, 450–625 m). The Γ_{cw} is focused in the deepening areas of the spiral concentric bars (X_d = 300–600 m) and in the new trough (X_d = 500–750 m).
S5	Start of cluster. Pre-storm northern LTT/TBR and southern TBR. Post-storm northern zone rip infill and a trough form (X_d = 100–300 m), outer bar moves landward 50 m. The southern zone gets a tough (X_d = 300–800 m) replacing TBR morphology and building off this with RBB channels and curvature switching (convex to concave orientation) of meandering bars (X_d = 450, 550–650 m) and the headland rip opened (X_d = 850 m).	Vorticity was mild overall with pockets of Γ_{cw} on opening rip channel heads in both zones (X_d = 100–200, 350, 400–450, 700 m) and at new rip channel locations (X_d = 400–450 m), at new alongshore troughs (X_d = 300–600, 650–850 m) and where the outer sand bar eroded (X_d = 700 m). The Γ_{ccw} is at the locations where the pre-storm rip channels infilled (X_d = 125, 225, 350, 400–500, 650 m).
S6	Mid-cluster. Pre-storm northern zone LTT and southern RBB. Post-storm is RBB extended seaward in southern zone, deep troughs formed alongshore (X_d = 200–650 m), a triple connected channel complex of meandering rhythmic bars (X_d = 250–500 m) and oblique channels became transverse to shoreline (X_d = 400, 650 m) and headland rip opened (X_d = 850 m).	The Γ_{ccw} was focused on edges prograding offshore (X_d = 225, 350–500, 550, 675 m) and on trough near the shoreline (X_d = 450–650 m). The Γ_{cw} was focused on the channels between sand bars (X_d = 275–450, 575–675, >775 m). Strong Γ_{ccw} was focused on the edges of a new transverse sand bar alongshore 675 m and at a newly opened rip head with meandering sand bar extension (X_d = 225 m).
S7	End of cluster. Pre-storm, RBB in southern and LTT in northern zone. Post-storm is LBT with a large open offshore trough formed along north-central beach (X_d = 200–550 m), a disconnected triangle bar (X_d = 550 m), a large rip channel in the south oriented south 45° (X_d = 650 m) and headland rip opened (X_d = 850 m).	Overall, the Γ was messy with stronger Γ_{cw} focused on the boundaries of the newly formed troughs in the central-north beach (X_d = 200–600 m) and in the rips in the southern zone (X_d = 550, 600, 750, 825 m). The strong Γ_{ccw} was focused on the leading edges of forming and prograding bars (X_d = 50–150, 400–500, 700 m).

S8	Pre-storm LTT in northern and RBB in southern zone. Post-storm bars reset and surf zone 75 m narrower (X_d = >350 m). Northern zone has infilled the alongshore trough (X_d = 50–400 m), replaced with meandering RBB (X_d = 200–300 m) and southern zone has new TBB new locations (X_d = 375, 425, 525, 625, 750 m).	Strong Γ_{ccw} along new outer sand bar (X_d = >350 m). Northern and southern zones, there are Γ_{cw} processes (X_d = 100, 300, 400, 550 650, 800 m) at that intersect the Γ_{ccw} bar at post-storm rip channels locations (X_d = 375, 425, 525, 625, 750 m) and nearshore toughs (X_d = 100–400 m).
S9	Pre-storm LLT in northern and RBB/LBT and northern zone was protected. Post-storm northern is RBB with oblique north 45° rips (X_d = 75, 225, 450 m), southern zone LBT with 100 m wide trough (X_d = >550 m) with rhythmic outer bar with corresponding beach lobes/cusps and open headland rip (X_d = 850 m).	Mild vorticity with both Γ_{cw} and Γ_{ccw}. Northern zone has stronger Γ_{ccw} along newly formed bars (X_d = 100, 200,350–400 m). The Γ_{cw} is at locations of new rip channels (X_d = 75, 225, 450 m). Southern zone has Γ_{ccw} along offshore bar and shoreline lobes (X_d = >600 m) and Γ_{cw} on boundaries and centre of the wide channel (X_d = >600 m).
S10	Pre-storm northern zone LTT, southern TBB with rips oblique north 45° (X_d = 175, 250 m). Post-storm bars reset, seaward extension, infilling shoreline (X_d = 200–700 m), a new trough (X_d = 225–800 m) and meandering TBB/RBB bars (X_d = 300–400, 500–600, 700, 800 m) and wider LTT in the northern zone (X_d = <250 m).	Vorticity was strong in this event. The Γ_{ccw} processes were at leading edges of forming meandering sand bars (X_d = 475, 575, 750 m). The Γ_{cw} processes were typically at the location of a developed and deep alongshore trough (X_d = 50–650) and at the widening and deepening of transverse rip channels (X_d = 50, 400, 525, 650, 750–825 m).
S11	Pre-storm northern LTT/TBR with trough (X_d<400 m), southern zone has meandering RBB (X_d = 350, 500 m) and TBB (X_d = 700 m). Post-storm, alongshore bar migration (X_d = 300–600 m), offshore sand bar forms (X_d = 150–400 m), extension of RBB in southern zone with double oblique south 45° sand bars (X_d = 400–600 m). Headland channel opened (X_d = 850 m).	Strong Γ_{ccw} at new outer bar adjacent to strong Γ_{cw} alongshore trough (X_d = 200–400 m). In southern zone, strong Γ_{ccw} at points of sand bar progradation at centre beach (X_d = 500 m) and strong Γ_{cw} at locations where trough or rip channels form (X_d = 475–650 m) and where channels are shallow (X_d = 750 m).

Table S3: Typical patterns of sand bar response, n observations and locations in beach length (X_d) from north (m) identified from the high-energy storms (S1–S11)

		Location, X_d (m) from north			
Storm	**n**	**Opened sand bar / rip channel**	**Meandering sand bar / trough**	**Concentric sand bar**	**Sand bar curvature switching**
S1	7	100, 250, 700, 850	-	100, 250, 500–600	-
S2	4	700, 850	450–700	700	-
S3	5	350	0–200	300–500	575, 700
S4	3	100	300–500	250–600	-
S5	4	650, 850	350–650	-	650
S6	7	250, 500, 650	50–150, 225–550	250–500	700
S7	4	250, 675, 850	100–500	-	-
S8	4	200, 375	100–300, 300–850	-	-
S9	6	250, 375, 850	600–850	-	250, 400–500
S10	6	250, 650, 750	300–500, 800	450–550	-
S11	7	850	150–400, 400–800, 600–800	500, 600–750	650–700

6.3.2 Supplementary Figures

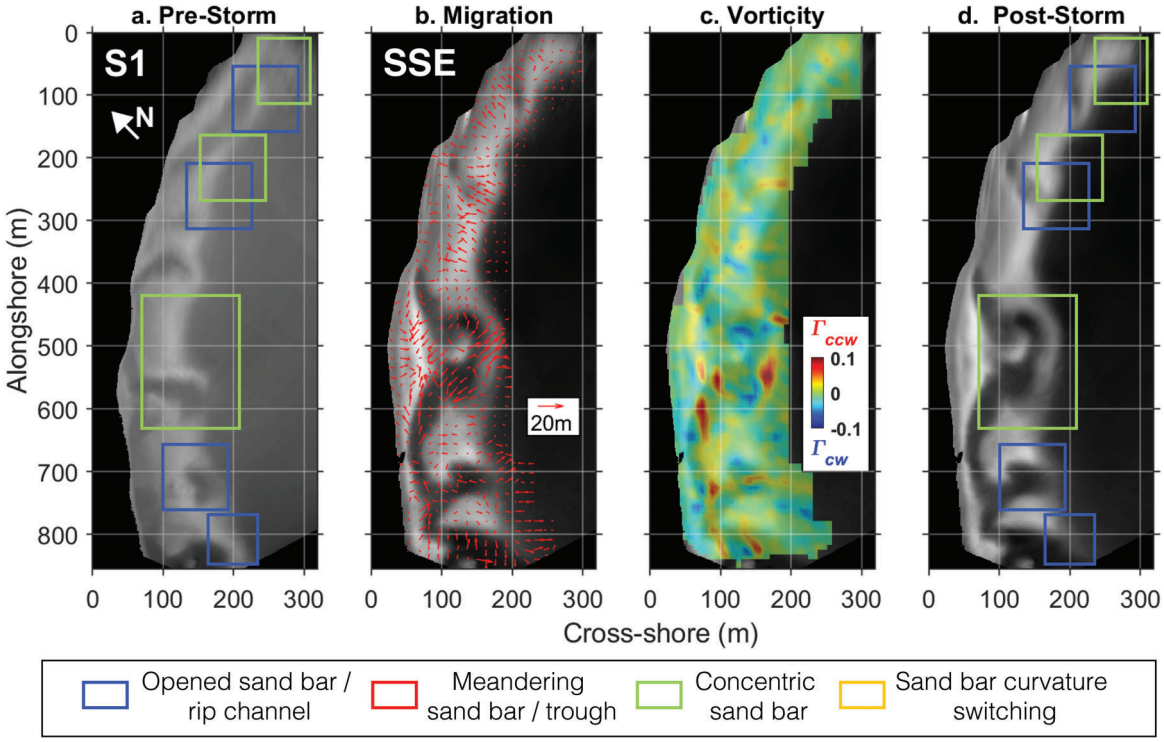

Figure S3: Sand bar migration and vorticity from June 2012 storm (S1) at Bondi Beach. The 4 key example sand bar response pattern are labelled.

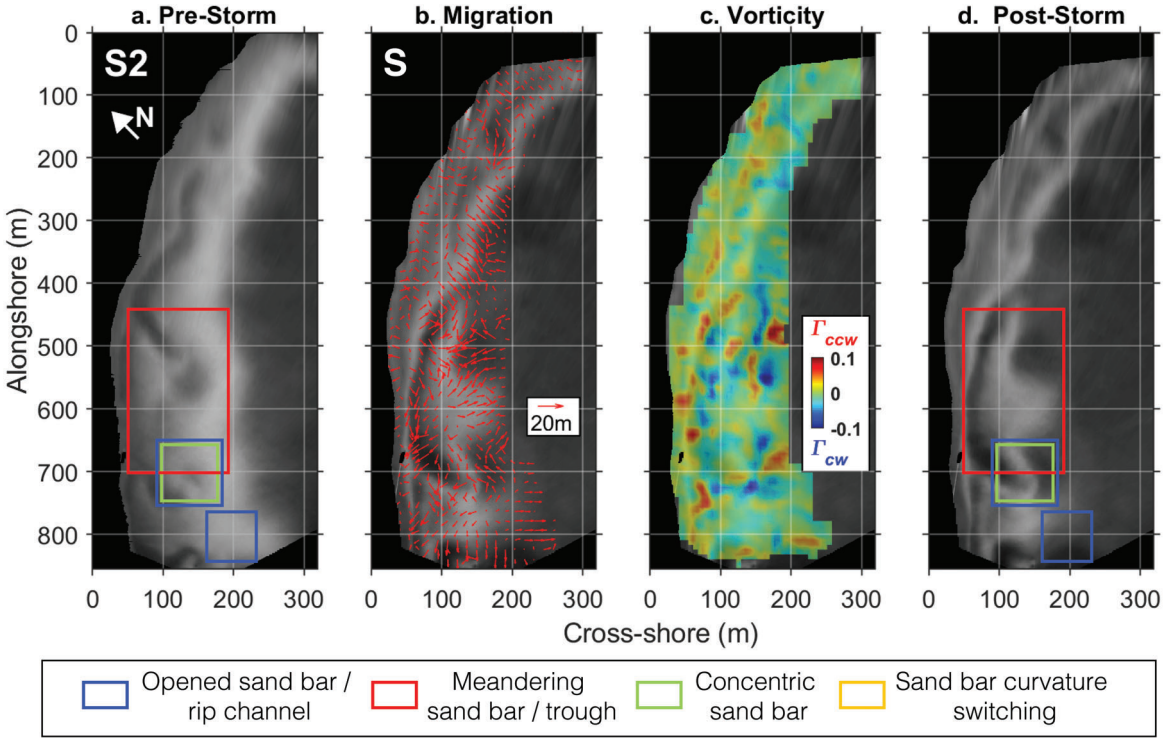

Figure S4: Sand bar migration and vorticity from July 2012 storm (S2) at Bondi Beach. The 4 key example sand bar response pattern are labelled.

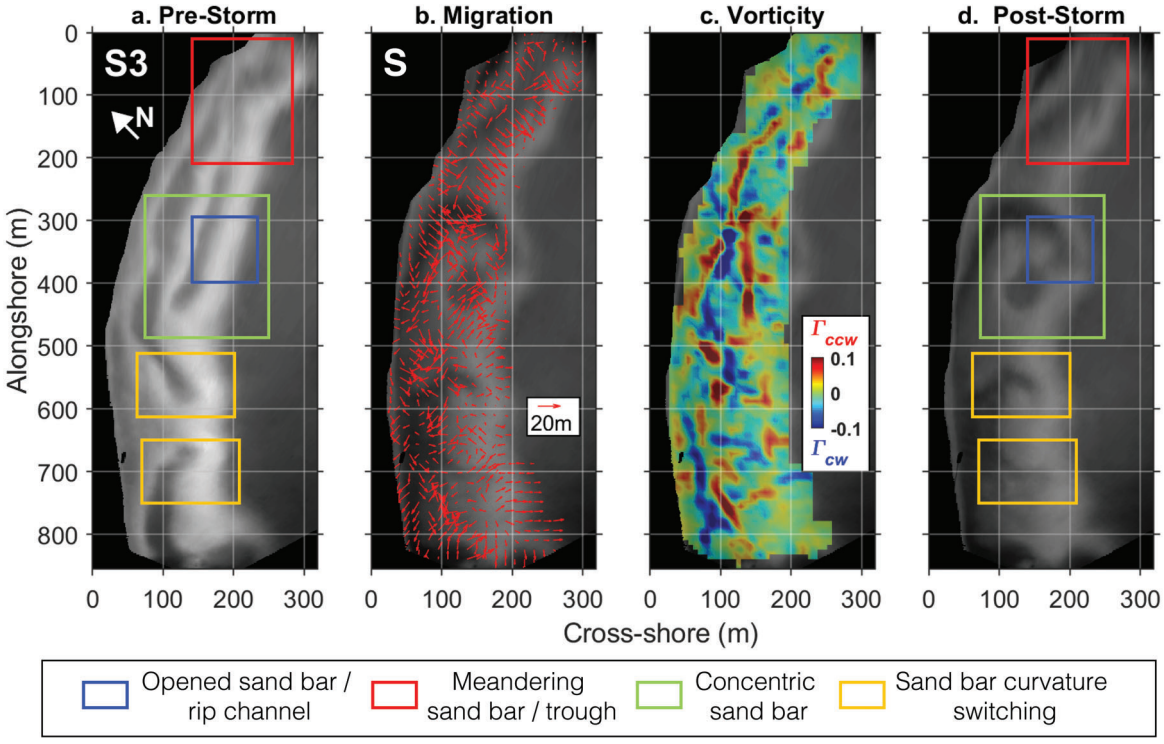

Figure S5: Sand bar migration and vorticity from June 2013 storm (S3) at Bondi Beach. The 4 key example sand bar response pattern are labelled.

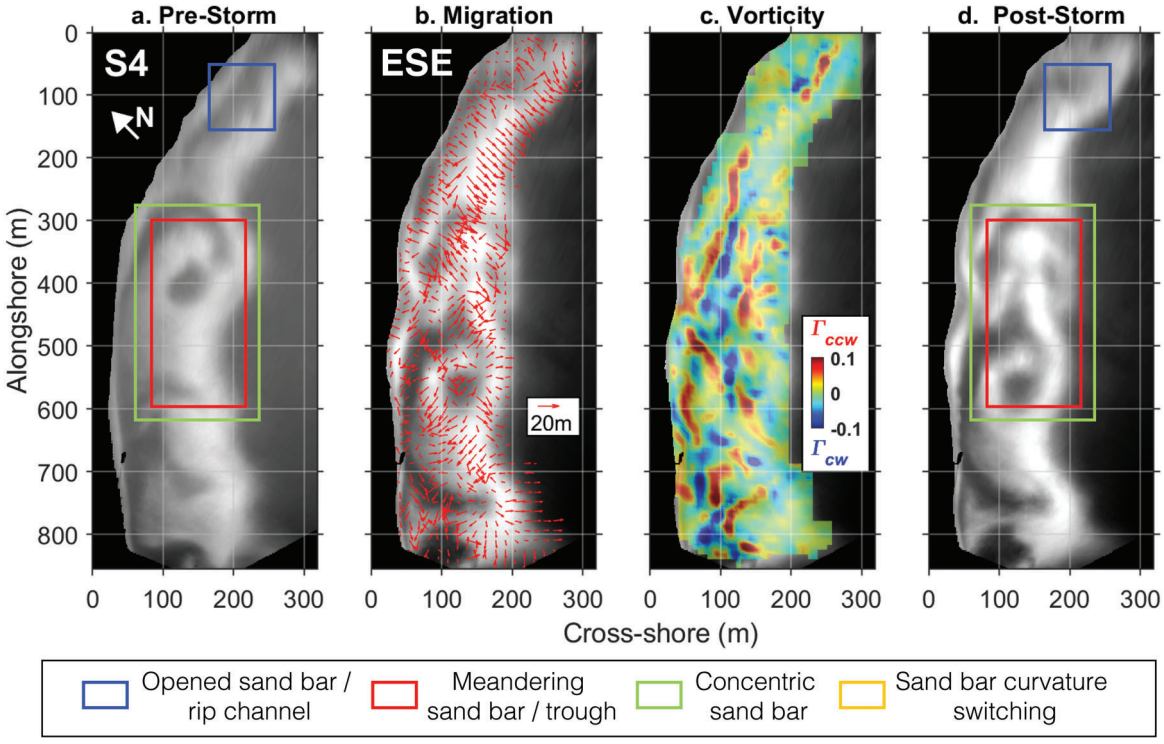

Figure S6: Sand bar migration and vorticity from June 2013 storm (S4) at Bondi Beach. The 4 key example sand bar response pattern are labelled.

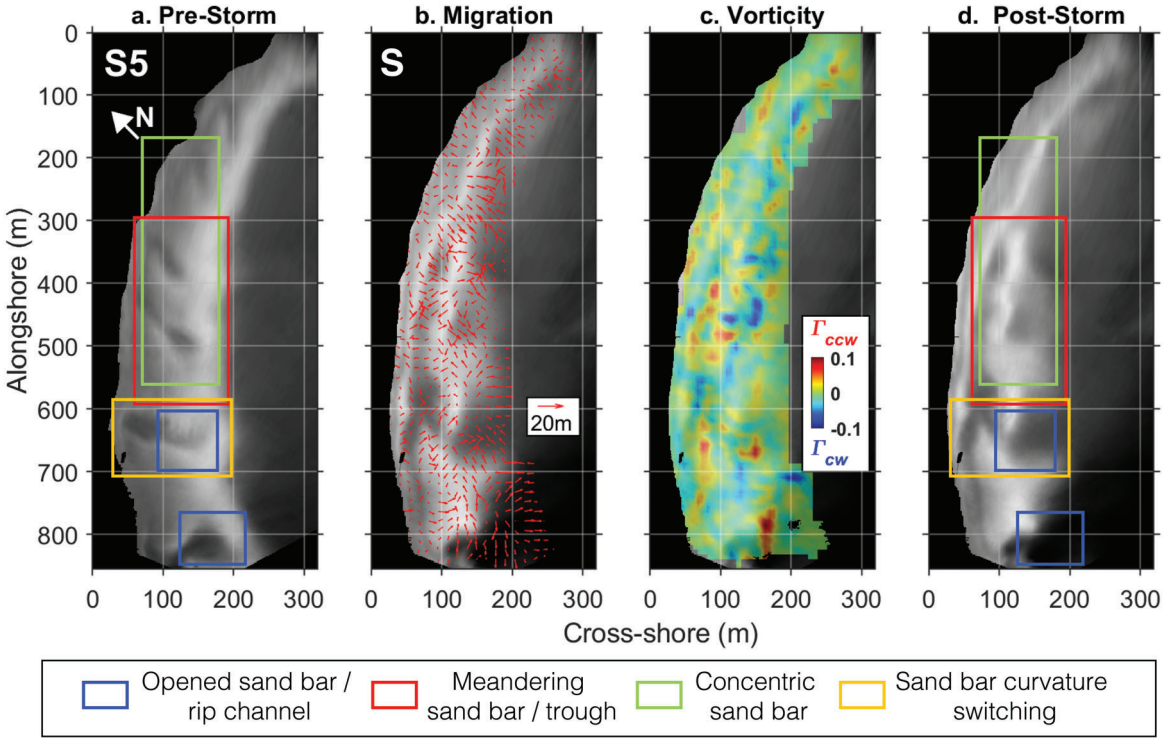

Figure S7: Sand bar migration and vorticity from July 2014 storm (S5) at Bondi Beach. The 4 key example sand bar response pattern are labelled.

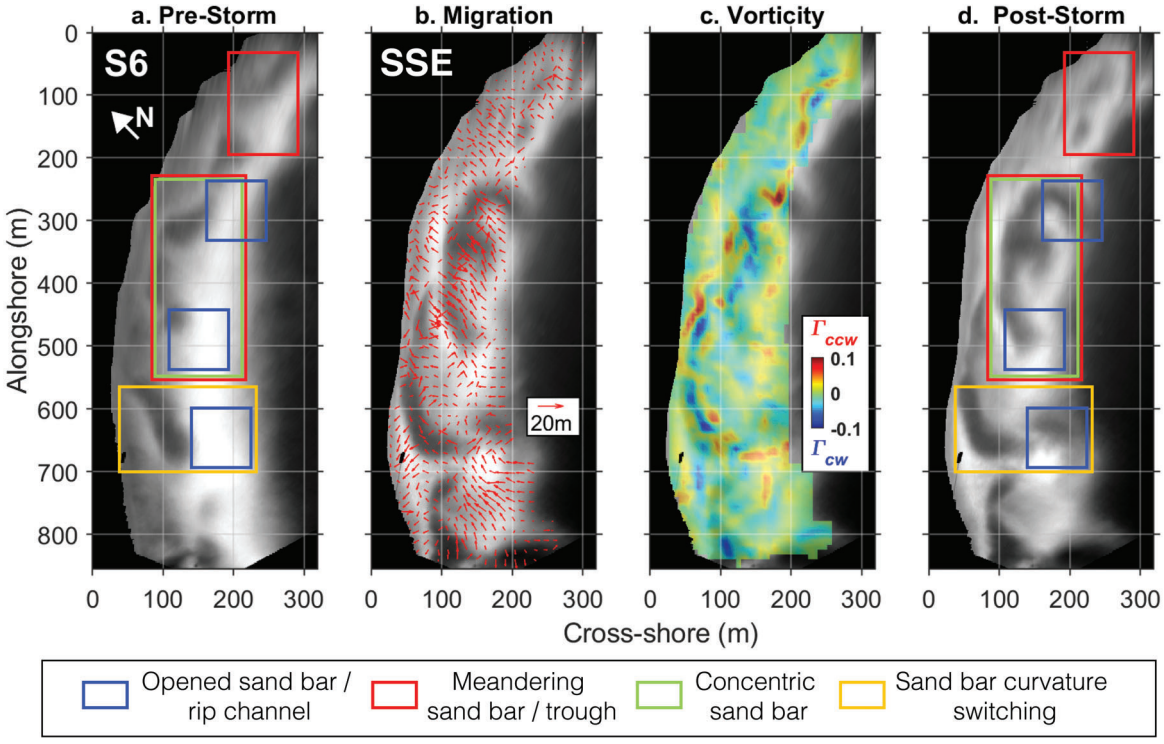

Figure S8: Sand bar migration and vorticity from August 2014 storm (S6) at Bondi Beach. The 4 key example sand bar response pattern are labelled.

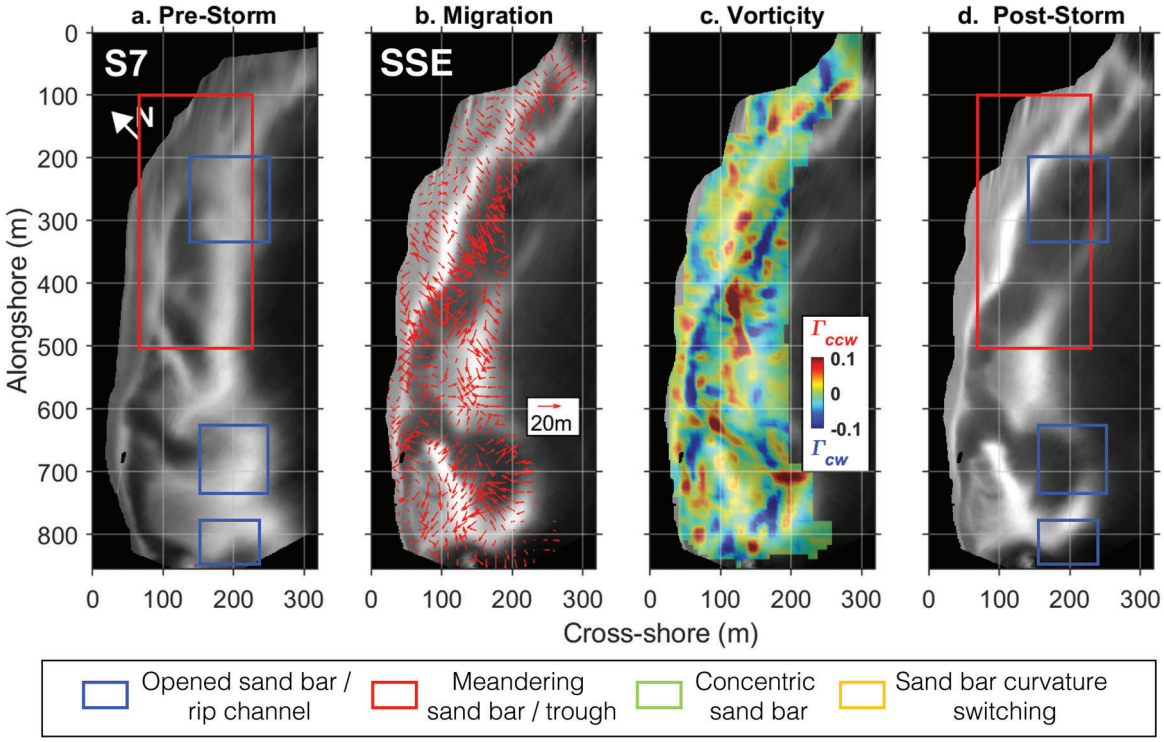

Figure S9: Sand bar migration and vorticity from September 2014 storm (S7) at Bondi Beach. The 4 key example sand bar response pattern are labelled.

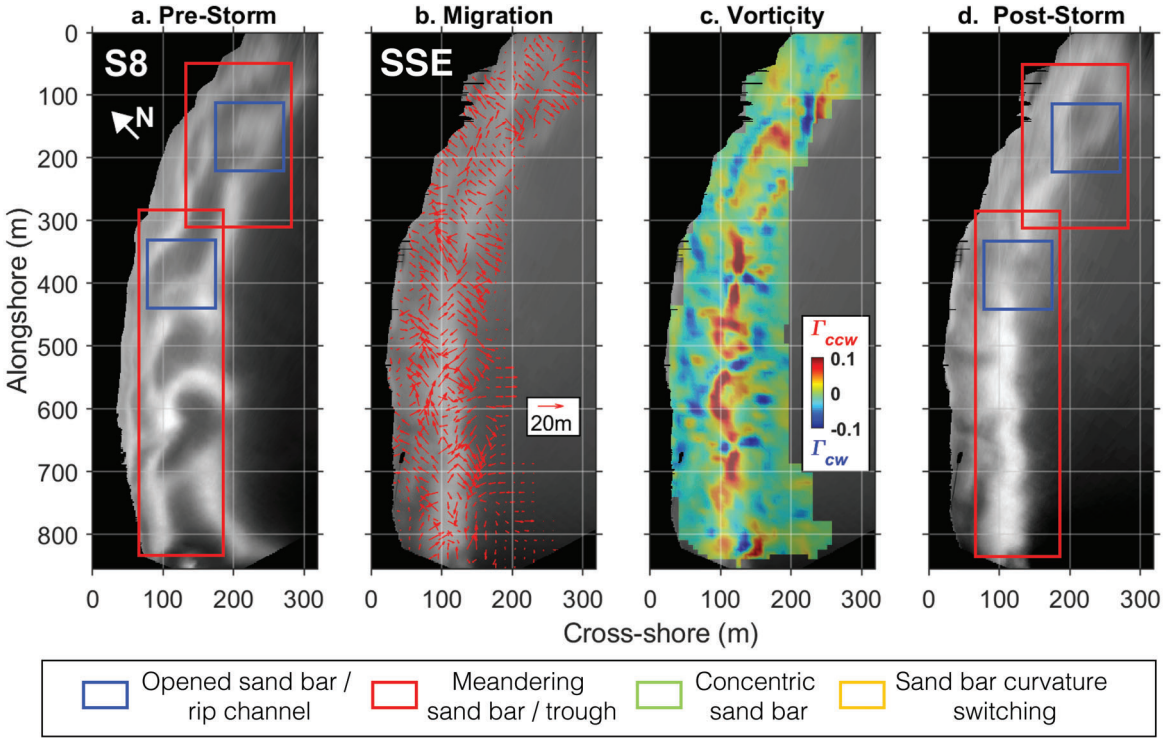

Figure S10: Sand bar migration and vorticity from April 2015 storm (S8) at Bondi Beach. The 4 key example sand bar response pattern are labelled.

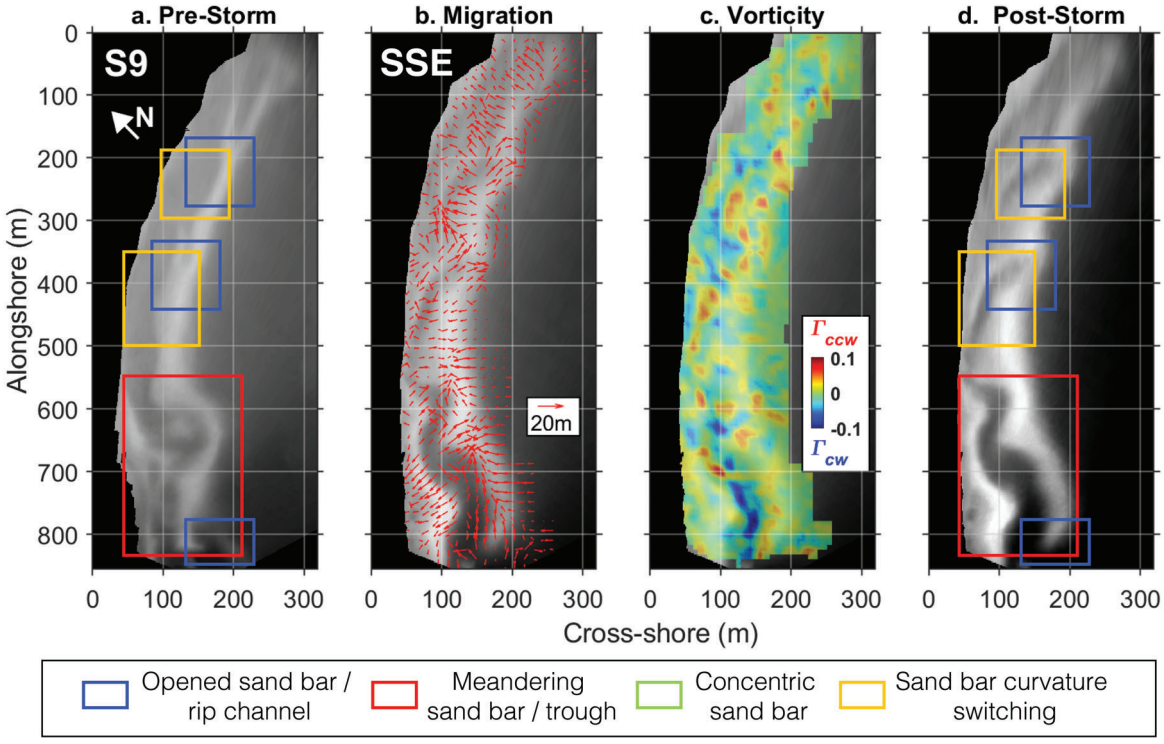

Figure S11: Sand bar migration and vorticity from June 2016 storm (S9) at Bondi Beach. The 4 key example sand bar response pattern are labelled.

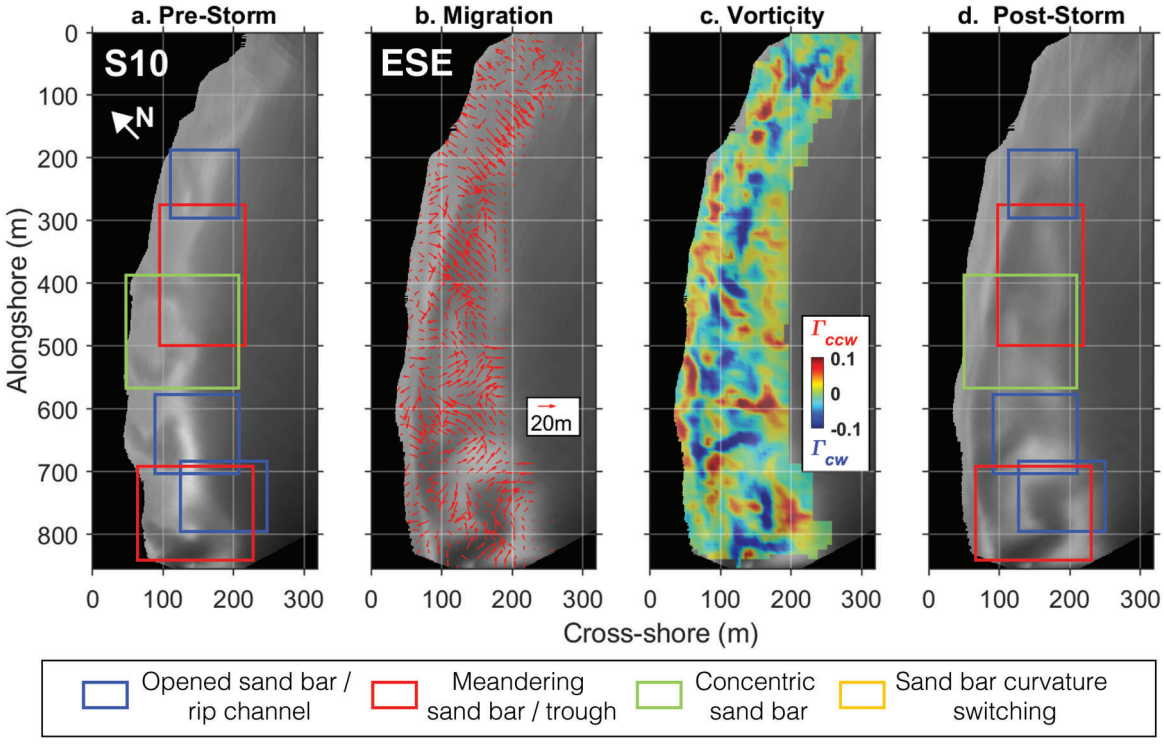

Figure S12: Sand bar migration and vorticity from March 2017 storm (S10) at Bondi Beach. The 4 key example sand bar response pattern are labelled.

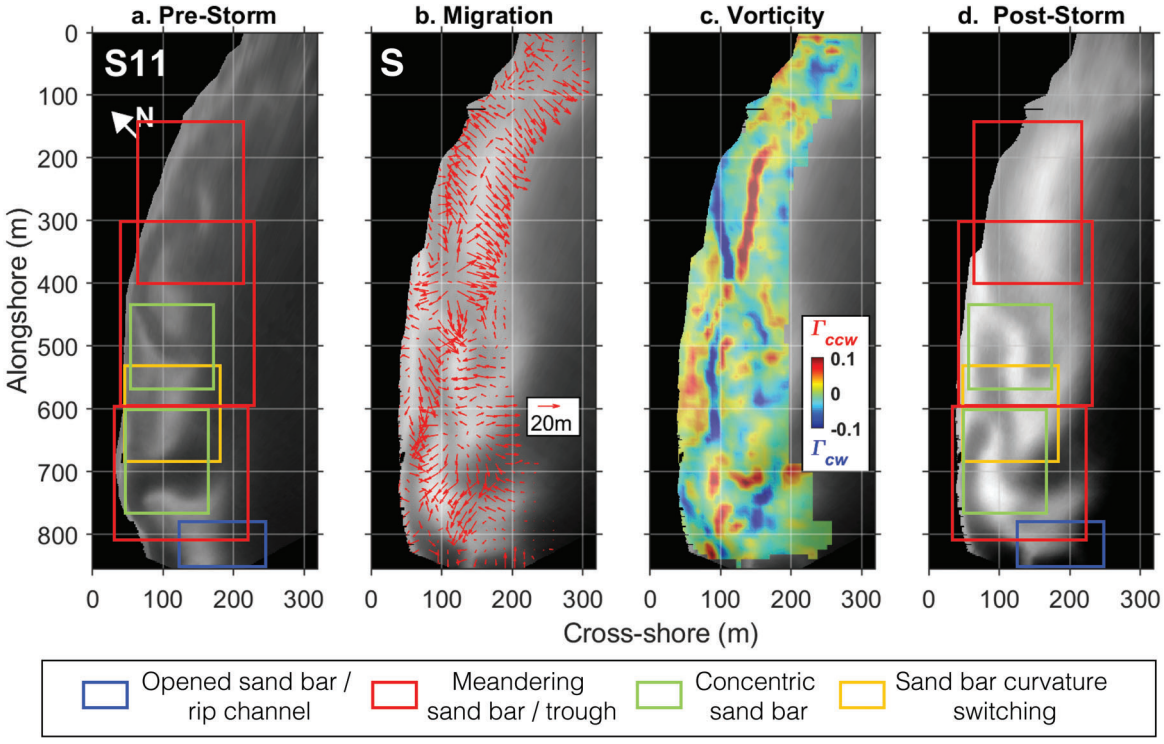

Figure S13: Sand bar migration and vorticity from May 2018 storm (S11) at Bondi Beach. The 4 key example sand bar response pattern are labelled.